

Oxygen-tension and the VHL-Hif1 α pathway determine onset of neuronal polarization and cerebellar germinal zone exit

Jan A. Kullmann,^{1,4,7} Niraj Trivedi,^{1,7} Danielle Howell,^{1,7} Christophe Laumonnerie,^{1,7} Vien Nguyen,² Shalini S. Banerjee,¹ Daniel R. Stabley,¹ Abbas Shirinifard,¹ David H. Rowitch,^{2,3} and David J. Solecki^{1,8*}

¹Department of Developmental Neurobiology, St. Jude Children's Research Hospital, Memphis, TN 38105, USA

²Department of Pediatrics and Eli and Edythe Broad Institute for Stem Cell Research and Regeneration Medicine Biomedical Sciences Graduate Program, University of California, San Francisco, San Francisco, CA 94143, USA.

³Department of Pediatrics, University of Cambridge and Wellcome Trust–MRC Stem Cell Institute, Hills Road, Cambridge CB2 0AN, UK.

⁴Molecular Neurobiology Group, Institute of Physiological Chemistry, Philipps University of Marburg, 35032 Marburg, Germany

⁷These authors contributed equally.

⁸Lead contact

*Correspondence: david.solecki@stjude.org

SUMMARY (140 words)

Postnatal brain circuit assembly is driven by temporally regulated intrinsic and cell-extrinsic cues that organize neurogenesis, migration, and axo-dendritic specification in post-mitotic neurons. While cell polarity is an intrinsic organizer of morphogenetic events, environmental cues in the germinal zone (GZ) instructing neuron polarization and their coupling during postnatal development are unclear. We report that oxygen tension, which rises at birth, and the von Hippel–Lindau (VHL)–hypoxia-inducible factor 1 α (Hif1 α) pathway, regulate polarization and maturation of post-mitotic cerebellar granule neurons (CGNs). At early postnatal stages with low GZ vascularization, Hif1 α restrains CGN-progenitor cell-cycle exit. Unexpectedly, cell-intrinsic VHL-Hif1 α pathway activation also delays the timing of CGN differentiation, germinal zone exit, and migration initiation through transcriptional repression of the partitioning-defective (Pard) complex. As vascularization proceeds, these inhibitory mechanisms become downregulated, implicating increasing oxygen tension as critical switch for neuronal polarization and cerebellar GZ exit.

INTRODUCTION

Lamination of the mammalian brain depends on the ability of neurons to exit the cell cycle, undergo directed cell migration, and coalesce into the neuronal layers that are the fundamental building blocks of neuronal circuitry (Ayala et al., 2007; Cooper, 2013; Hatten, 2002). A number of human pediatric neurologic disorders and brain cancers involve dysregulation of neuronal motility or the timing of progenitor germinal zone (GZ) exit, ultimately resulting in abnormal neuronal circuit formation (Hatten and Roussel, 2011; Metin et al., 2008). During brain morphogenesis, cell polarity signaling molecules are required to establish regional asymmetry, axon-dendrite specification (Barnes and Polleux, 2009; Lewis et al., 2013), neurogenesis (Falk et al., 2017; Taverna et al., 2014), radial migration or migration initiation (Cooper, 2013; Singh and Solecki, 2015), and cellular recognition via adhesion (Rasin et al., 2007; Solecki, 2012). However, the coordination of the precise polarity pathways involved in development and CNS disease is poorly understood.

The cerebellum is a suitable system with which to investigate this issue. Recent studies by our laboratory in the mouse cerebellar granule neuron (CGN) model system have shown that the regulatory events that shape polarity development extend beyond conventional signaling events (e.g., canonical polarity protein phosphorylation (McCaffrey and Macara, 2009; Namba et al., 2015)). Our findings suggest a model in which parallel transcriptional (e.g., Zeb1 (Singh et al., 2016)) and ubiquitination (e.g., Siah2 (Famulski et al., 2010)) pathways act in a switch-like manner to orchestrate polarity initiation during the earliest stages of

neuronal differentiation by controlling the onset of expression of the partitioning-defective (Pard)-complex gene or protein (Laumonnerie and Solecki, 2018). Despite advances in our knowledge of how differentiation is intrinsically controlled by gene expression programs (Kohwi and Doe, 2013; Syed et al., 2017) and how polarity is linked to differentiation status (Singh and Solecki, 2015; Uzquiano et al., 2018), key challenges remain to our understanding of how polarity signaling cascades are regulated during neuronal differentiation, how they are affected by cell-extrinsic conditions that accompany development, and how changes in polarity signaling affect the interactions of progenitors or newborn neurons with GZ niches.

In this study, we investigated the general role of oxygen homeostasis in CGN development and specific connections to polarity regulators that control their polarization due to inferred connections to oxygen levels (Bui et al., 2009; Krishnamachary et al., 2006; Nakayama et al., 2004; Nakayama and Ronai, 2004). In a variety of brain regions, oxygen levels affect neural stem cells (Lange et al., 2016; Mazumdar et al., 2010; Morrison et al., 2000; Studer et al., 2000) (reviewed by (Mohyeldin et al., 2010; Panchision, 2009; Simon and Keith, 2008)), and specific vascular relations with germinal niches *in vivo* have been described for some lineages (Javaherian and Kriegstein, 2009; Lange et al., 2016; Palmer et al., 2000; Shen et al., 2004; Shen et al., 2008; Tavazoie et al., 2008). Also, brain-tissue oxygen tension is critical to healthy brain development; both elevated and reduced oxygen have been linked to altered neurodevelopment and cognitive impairment (Salmaso et al., 2014). The hypoxia-inducible factor 1 α (Hif1 α) pathway is the primary adaptive mechanism used by cells to respond to alterations in oxygen

levels (Kaelin, 2008; Kaelin and Ratcliffe, 2008). In normoxia, the prolyl hydroxylase (PHD) enzymes Egl nine homologs 1–3 (Ivan and Kaelin, 2017) (EGLN1–3) negatively regulate the Hif1 α hypoxia-response transcription factor by creating a proline-based binding site on Hif1 α for the von Hippel–Lindau (VHL) E3 ubiquitin ligase (Gossage et al., 2015), thus targeting Hif1 α for degradation. In hypoxia, this repression is relieved and Hif1 α is free to activate target-gene expression (Semenza et al., 2006). Although the Hif1 α pathway is well characterized molecularly, a key challenge in basic neuroscience is to identify the molecules and genetic pathways that are affected by oxygen homeostasis during brain maturation, particularly those that restrain the onset of neuronal differentiation and neuronal morphogenesis.

We hypothesized that oxygen tension controlled the onset of CGN differentiation and GZ exit in a manner involving the regulation of cell polarity. We found that the early postnatal mouse cerebellum is poorly vascularized and hypoxic and that granular neuron precursors (GNPs) in the external germinal layer (EGL) express Hif1 α at high levels until the period of CGN differentiation commences. *In vivo*, inhibition of the Hif1 α pathway diminishes GNP proliferation, whereas activation enhances it. We investigated whether oxygen tension and the Hif1 α pathway also regulated events that occur concomitantly with neuronal differentiation, and we discovered that manipulation of oxygen homeostasis controls the timing of CGN GZ exit and migration initiation: both hypoxia and Hif1 α promote germinal niche occupancy and restrain GZ exit. By systematic epistasis analysis, we revealed that the Hif1 α pathway controls the onset of neuronal

polarization by activating the expression of Zeb1, a transcriptional repressor that suppresses the expression of the polarity genes *Pard3* and *Pard6a* (Singh et al., 2016), thereby providing a direct link between oxygen tension and the regulation of neuronal cell polarity, differentiation and migration initiation. Finally, we explored how the Hif1 α /Zeb1 axis promotes GZ occupancy. Immature CGNs express high levels of integrin β -1 (Itg β 1) receptor (Blaess et al., 2004). We found that *Itg β 1* is transcriptionally activated by Zeb1 and that hypoxia stimulates the binding of GNPs to Itg β 1 receptor substrates. Itg β 1 receptor gain of function is sufficient to promote GNP GZ occupancy, whereas the corresponding loss of function rescues GZ exit in the presence of hypoxia. Surprisingly, the restoration of *Pard6a* expression in the context of Zeb1 or Hif1 α gain of function diminishes Itg β 1 receptor focal adhesions, linking cell polarity molecules with a mechanism that relieves GZ occupancy for differentiating progenitor cells. Thus, we provide an integrated model of how oxygen tension controls polarity-dependent cell interactions with niche substrates and their impact on the earliest stages of neuronal circuit formation. This model enhances our understanding of both normal brain development and the cell biological mechanisms that go awry when oxygen homeostasis is perturbed.

RESULTS

Oxygen Tension and Hif1 α Pathway Activation Change Dynamically in the GZ Niche of the Early Postnatal Cerebellum

To test the role of oxygen homeostasis in GNP and CGN development, we examined key features of the niche in which these cells develop, such as the relative oxygen levels, the time course of vascularization and Hif1 α expression. Organs and cells low in oxygen can be identified by using intraperitoneal injections of pimonidazole (HypoxyprobeTM), which binds to tissues when the oxygen concentration is 2% or lower. Although pimonidazole adducts were detectable in the cerebellar cortex at P5 and P9, pimonidazole binding was greatly reduced at P15 *in vivo* (Figure 1A), suggesting that hypoxia is relieved in later cerebellar development. Consistent with these results, vascularization is sparse at P5 and P9 and there is a marked increase in the vasculature in all cerebellar layers at P15 as demonstrated by immunohistochemical staining of the endothelial glucose transporter 1 (GluT1) in CLARITY–passive-cleared cerebellar slices (Figure 1B, GluT1 levels doubled in all regions when comparing P5 GluT1 levels to P15 levels in the respective regions). We were also curious as to whether the relative vascular disparity in the EGL and molecular layer (ML) of the cerebellum was indicative of a local difference from the internal granule layer (IGL) or a broad difference across brain regions. Therefore, we applied iDisco tissue-clearing methods to GluT1 staining of the hindbrain, midbrain, and cerebellum of P7 animals. We computationally analyzed the whole 3D volume of these brain tissues and used the 100- μ m region in the vicinity of an *Atoh1*^{EGFP/EGFP} in frame fusion marker (Rose et al., 2009) to highlight the relative location of immature GNPs in the EGL. The

3D vascular volumes measured via Ilastik-mediated machine learning (Kreshuk et al., 2011) showed that the EGL and ML have roughly half the vascular volume of not only the IGL, as predicted by our conventional histology analysis, but also the P7 hindbrain and midbrain (Figure 1C, Supplemental Movie 1, [T-test vascular volume fraction EGL+ML vs. IGL $P=0.0004$, vs. Hindbrain= 0.00004 , vs. Midbrain= 0.019]). This indicates that brain regions in the vicinity of the cerebellum that contain mature neurons have higher vascular density relative to the EGL and ML. Finally, we surveyed the expression of Hif1 α in the cerebellum. At postnatal day 7 (P7), Hif1 α expression coincides with that of the proliferation marker Ki67 in the external granular layer (EGL) but is greatly reduced in p27^{Kip1}-positive postmitotic CGNs (Figure 1D). At P15, Hif1 α is greatly diminished in the cerebellar cortex. The high levels of Hif1 α expression during the peak of GNP neurogenesis prompted us to examine whether this period correlated to a hypoxic environment in the early postnatal cerebellum. Western blots of cerebellar lysates from different developmental time-points with antibodies against Hif1 α and pimonidazole. Both of these hypoxia markers were abundant between P2 and P9 but abated after P9 (see Figure 1E for quantitation, $60 \pm 6.8\%$ [$\bar{x} \pm \text{sem}$] reduction in Hif1 α expression compared to P7 levels, [T-test, $P<0.0001$], $59.7 \pm 12.5\%$ reduction in pimonidazole values normalized to actin levels when compared to P7 values T-Test, $P<0.05$]), confirming not only that the oxygen environment undergoes changes during cerebellar development but also that there are cellular responses to these changes, at least at the level of Hif1 α expression. Taken together, these results show that the oxygen status of the developing cerebellum varies considerably

during the peak stages of neurogenesis and CGN maturation: proliferating GNPs reside in hypoxic regions and express Hif1 α , whereas differentiating CGNs reside in vascularized layers of the cerebellum. Moreover, after a burst of vascularization at P9 that also coincides with neuronal differentiation in the CGN lineage, neither hypoxia nor Hif1 α expression is detectable in the developing cerebellum.

The Hif1 α Pathway Modulates GNP Neurogenesis *in Vivo*

Because Hif1 α is expressed in Ki67-positive GNPs (Figure 1), we wished to determine whether altering Hif1 α pathway activity influenced their proliferation. To this end, we generated *Atoh1-Cre:Hif1 $\alpha^{flx/flx}$* and *Atoh1-Cre:VHL^{flx/flx}* mice that lacked Hif1 α or VHL, respectively, specifically in the CGN lineage. To test for the successful deletion of *Hif1 α* , we purified CGNs from P7 mice and incubated them for 24 h in 20% or 2% O₂. Although purified CGNs of *Hif1 $\alpha^{flx/flx}$* mice maintained in 2% O₂ expressed Hif1 α , we detected a 75.6 \pm 5.8% reduction in levels of Hif1 α in CGNs of *Atoh1-Cre:Hif1 $\alpha^{flx/flx}$* mice by Western blot analysis (Figure 2A). Having shown that *Hif1 α* had been successfully removed from the CGNs of *Atoh1-Cre:Hif1 $\alpha^{flx/flx}$* mice, we found a small but consistent decrease in their cerebellar size at P7, P10, and P15 when compared to control cerebella (Figure 2B, 15%, 11% and 9% volume change respectively for each timepoint; T-test P<0.01, 0.02 and 0.07 respectively). Next, we wished to know whether the reduced cerebellar size was due to diminished proliferation of GNPs in the *Atoh1-Cre:Hif1 $\alpha^{flx/flx}$* mice. Accordingly, we injected EdU into P7 mice, euthanized them 1 h later, and analyzed the extent of GNP EdU incorporation and the abundance of mitotic cells, as detected with antibodies against phospho-histone H3 (pH3). Although the

number of EdU⁺ GNPs was only slightly lower in Hif1 α -deficient CGNs (*Hif1 α ^{flx/flx}*: 268 \pm 17 cells/mm; *Atoh1-Cre:Hif1 α ^{flx/flx}* 246 \pm 11 cells/mm; $P > 0.05$), the number of pH3⁺ cells was reduced by 23 \pm 6% (Figure 2C), suggesting that GNP proliferation was impacted. To assess actively cycling, proliferating GNPs, we calculated the ratio of cells that had been recently born but still capable for further proliferation (EdU⁺ /Ki67⁺ cells) and those that had already exited the cell cycle (EdU⁺/Ki67⁻ cells). In *Atoh1-Cre:Hif1 α ^{flx/flx}* mice, we found a 53 \pm 15% increase in EdU⁺/Ki67⁻ cells, indicating a larger fraction of *Hif1 α* -deleted GNPs had exited cell-cycle and begun differentiation (T-test, $P < 0.05$; Figure 2D,E). In contrast, Hif1 α pathway activation in *Atoh1-Cre:VHL^{flx/flx}* mice led to increased EdU incorporation into GNPs (*VHL^{flx/flx}*: 218 \pm 1 cells/ μ m; *Atoh1-Cre:VHL^{flx/flx}*: 274 \pm 3 cells/ μ m; $P < 0.01$) and in the number of pH3⁺ cells in the EGL (39 \pm 5% increase), as compared to that of *VHL^{flx/flx}* mice (T-test, $P < 0.02$; Figure 2C and 2D). Consistent with these results, there were fewer cell-cycle exit events in the EGL of *Atoh1-Cre:VHL^{flx/flx}* mice because the percentage of EdU⁺/Ki67⁻ cells was reduced by 30 \pm 5%, as compared to that in the control cerebella (T-test, $p < 0.02$; Figure 2E). It is notable the increase in Hif1 α -pathway activity in *Atoh1-Cre:VHL^{flx/flx}* mice is accompanied by only a slight alteration in apoptosis in the P7 cerebellum, mainly localized to the IGL (Supplemental Figure1) These results suggest that not only does the cerebellum have a rapidly changing oxygen environment during development but the Hif1 α pathway functions to adjust the levels of actively cycling transiently amplifying progenitor-cells within the EGL GZ niche.

The Hif1 α Pathway and Hypoxia Regulate the Timing of Postmitotic CGN GZ Exit and Migration

Having demonstrated that the Hif1 α pathway influences the proportions of proliferating GNPs and differentiating CGNs, we next sought to investigate whether hypoxia or alterations in oxygen homeostasis via the Hif1 α pathway also regulated events that occur after differentiating CGNs become postmitotic, such as GZ exit or the initiation of radial migration. For these experiments, where migration is also a surrogate linked with CGN maturation, we used *ex vivo* organotypic cerebellar slices that were electroporated with an H2B-mCherry–labeled expression construct and maintained in culture under a range of O₂ levels including: standard culture condition of 20% O₂, hypoxia (2%, 5%, 10% or 15% O₂), or hyperoxia (40% O₂). Previous work had established that GNPs in *ex vivo* cerebellar slices incubated in 20% O₂ exhibit differentiation and migration kinetics indistinguishable to those seen *in vivo* (Famulski et al., 2010; Ruiz de Almodovar et al., 2010). After incubating cerebellar slices *ex vivo* for 24 or 48 h, we analyzed the distribution of CGNs through the GZ and layers occupied by maturing neurons via migration by measuring the distance of H2B-mCherry–positive CGNs from the pial surface of the cerebellar slices (Figure 3A). Overall, hypoxic conditions increased the numbers of cells that remained near their GZ [depending on the relative level of hypoxia \(see 2-40% gradient\), while higher oxygen concentrations supported maximal inwards displacement toward the IGL](#). At 24 h, cells in slices incubated at 20% O₂ demonstrated an average distance from the pial surface of $61.5 \pm 2.1 \mu\text{m}$ (\bar{x} distance \pm sem), whereas cells in slices incubated at 2% O₂ displayed an \bar{x}

distance of $39.6 \pm 4.1 \mu\text{m}$ (T-test, $P < 0.002$; Figure 3A, [See Supplemental Figure 2 for data on intermediate oxygen concentration displayed in summary box plot and legend for detailed statistical analysis](#)). At 48 h there was still a significant difference between average distances of cells in slices incubated at 2% O_2 ($66.1 \pm 7.0 \mu\text{m}$) and 20% O_2 ($93.0 \pm 5.3 \mu\text{m}$, T-test, $P < 0.01$). Slices incubated in 40% O_2 showed a trend for more migration towards the IGL ($100.7 \pm .4 \mu\text{m}$), although replicate variability diminished statistical significance (T-test, $P < 0.15$, compared to 20% 48 h data). To examine directly CGN migration kinetics in response to hypoxia, we used long-term time-lapse microscopy to longitudinally image CGN motility in *ex vivo* slices under conditions of 2% or 20% O_2 , starting approximately 18 h after the slices were placed in culture (Figure 3B). Consistent with the results of studies on fixed slices, time-lapse imaging revealed that higher amounts of GZ resident cells in slices maintained in 2% O_2 than in the GZ niche of slices maintained in 20% O_2 (see Supplemental Movies 2 & 3). Interestingly, dynamic layer-occupancy calculations showed that whereas the population of cells in the outer EGL (oEGL) of slices maintained in 20% O_2 decreased rapidly over the observation period, the rate of oEGL exit was diminished in 2% O_2 . Similarly, the increases in layer occupancy in the ML and IGL were diminished in 2% O_2 , and the efficiency of motility (measured in terms of how many neurons persisted along the migration directions) was most potently disrupted in these layers (Figure 3B).

Hypoxic insults greatly reduce the ability of cells to produce energy equivalents through oxidative phosphorylation and, therefore, they increase the abundance of glycolytic enzymes (Knobloch and Jessberger, 2017). Because

energy production solely through glycolysis predominates in hypoxia and is less efficient than other means of energy production, we wondered whether reduced energy production was limiting GZ exit and migration in hypoxic conditions. Accordingly, we incubated cerebellar slices in medium supplemented with glucose (\bar{x} distance = $64.7 \pm 1.7 \mu\text{m}$), as the control condition; in medium supplemented with galactose instead of glucose to prevent energy production through glycolysis (\bar{x} distance = $60.5 \pm 2.4 \mu\text{m}$); and in the presence of 1 mM malonate, a specific inhibitor of succinate dehydrogenase, a component of the TCA cycle and the electron transport chain. Inhibiting energy production through glycolysis or oxidative phosphorylation alone had no significant influence on neuronal migration (\bar{x} distance = $61.6 \pm 4.0 \mu\text{m}$; Figure 3C), demonstrating that limiting energy production does not impede the transition to the IGL.

Given that hypoxia regulated either the timing or kinetics of GZ exit and subsequent migration to the IGL, we next assessed the effect of Hif1 α pathway function on that process. We performed Hif1 α gain-of-function studies by ectopically expressing a hydroxylation-deficient, and thereby stabilized, form of Hif1 α (Hif1 α HD) (Kaelin, 2008; Kaelin and Ratcliffe, 2008) in GNPs in *ex vivo* cerebellar slices for 48 h. Expression of Hif1 α HD in GNPs led to a dose-dependent increase in GZ occupancy at 48 h (Figure 4A upper-left panels, LacZ: \bar{x} distance = $57.8 \pm 3.9 \mu\text{m}$; 1 $\mu\text{g}/\mu\text{L}$ Hif1 α HD OE: \bar{x} distance = $46.5 \pm 1.9 \mu\text{m}$, $P < 0.05$; 4 $\mu\text{g}/\mu\text{L}$ Hif1 α HD OE: \bar{x} distance = $41.7 \pm 3.6 \mu\text{m}$, $P < 0.001$ X^2 test and $P, 0.02$ T-test). To further characterize Hif1 function we introduced inactive (control) or active Cre recombinase into the *Hif1 α ^{flx/flx}* GNPs. Not only did electroporation of Cre

recombinase into *ex vivo* slices from *Hif1 α ^{flx/flx}* mice lead to enhanced displacement to the IGL of CGNs in slices maintained under standard oxygen conditions (Figure 4A, lower-left panels), *Hif1 α* deletion also reversed enhanced GZ occupancy seen in the hypoxia (Figure 4A, lower-right panels, at 2% O₂ Cre^{inactive}: \bar{x} distance = 25.3 ± 1.3 μ m, Cre^{active}: \bar{x} distance = 43.5 ± 3.7 μ m, X² and T-test analysis both $P < 0.0002$). Finally, we were curious as to whether the enhanced displacement to the IGL of *Hif1 α* -deficient CGNs represented an alteration in the timing of CGN migration or simply reflected enhanced general motility. Interestingly, longitudinal time-lapse imaging starting approximately 18 h after the slices were placed in *ex vivo* culture revealed that most *Hif1 α* -deficient CGNs had already undergone GZ exit by the start of imaging (Figure 4B, dynamic layer-occupancy graph in left panel, see Supplemental Movies 4 & 5) and that these cells exhibited no changes in their average speed of motility, as compared to that of controls (Figure 4B, migration speeds in right panel). Thus, *Hif1 α* deletion not only reduced the proportion of GNPs in the EGL *in vivo* but also accelerated the onset of GZ exit and migration initiation in post-mitotic CGNs.

Under normoxic conditions, *Hif1 α* is degraded through the action of the VHL ubiquitin ligase and PHD enzymes, which are critical mediators of the oxygen homeostasis machinery (Kaelin, 2008; Kaelin and Ratcliffe, 2008). Hence, we examined whether deleting VHL or PHDs would regulate GZ exit or migration initiation in a manner similar to that observed when we manipulated *Hif1 α* itself. We electroporated P7 EGLs of cerebella harvested from *VHL^{flx/flx}*, *EGLN1^{flx/flx}* or *EGLN3^{flx/flx}* mice to introduce inactive (control) or active Cre recombinase into the

GNPs and examined the distribution of labeled CGNs. As with the ectopic expression of Hif1 α in cerebellar slices or maintaining slice in culture at 2% O₂, GZ occupancy was significantly increased when we deleted VHL or EGLN1 (VHL Cre^{inactive}: \bar{x} distance = 117.6 \pm 0.4 μ m; VHL Cre^{active}: \bar{x} distance = 80.5 \pm 3.8 μ m; $P < 0.001$ [χ^2 test] or $P < 0.001$ [t -test]) (Figure 4C and Supplemental Figure 3 for EGLN1 and 3 deletion and legend for detailed statistical analysis). In these cases, GZ exit and subsequent CGN displacement towards the IGL was restored by introducing VHL, EGLN1 or EGLN3 cDNA, respectively (Cre^{active} + VHL: \bar{x} distance = 105.7 \pm 4.7 μ m; $P < 0.001$ [χ^2 test] and $P < 0.004$ [t -test] vs Cre^{active} [Figure 4C]). Importantly, deletion of *Hif1 α* in VHL-deficient CGNs restored displacement to the IGL to control levels, confirming the Hif1 α dependence of the VHL phenotype (Supplemental Figure 4A and see legend for detailed statistical analysis). As with *Hif1 α* deletion, we were curious as to whether the phenotype that resulted from the deletion of upstream oxygen-homeostasis components was due to an alteration in the timing of CGN migration or to decreased general motility. Longitudinal time-lapse imaging of VHL-deficient cells, starting approximately 18 h after they were placed in *ex vivo* culture, revealed persistent GZ occupancy and delayed transition to the ML and IGL (Figure 4D; see dynamic layer-occupancy graph in left panel, see Supplemental Movies 6 & 7) in the absence of changes in the overall cell motility, showing that VHL loss of function delays the onset of GZ exit and the initiation of radial migration. Taken together, these results show that the low oxygen levels in the early postnatal cerebellar environment and, more specifically, the Hif1 α pathway modulate progenitor-cell neurogenesis *in vivo* but also control

the timing of the exit of neuronal progenitors from the germinal niche to initiate radial migration to a final laminar position.

Given the apparent dual role of the Hif1 α pathway in modulating GNP neurogenesis, the ensuing timing of GZ exit and migration initiation to the IGL, we also investigated crosstalk with the Sonic hedgehog (Shh) mitogen signaling cascade, the major reported regulator of GNP neurogenesis and GZ exit by deleting *VHL* alone or in combination with the *Patched* (*Ptch*) Shh receptor. We electroporated P7 EGLs of cerebella harvested from *VHL*^{flx/flx} or *VHL*^{flx/flx};*Ptch*^{flx/flx} mice to introduce inactive (control) or active Cre recombinase into the GNPs and examined the distribution of labeled CGNs to assess displacement to the IGL as a surrogate for the timing of migration. Analysis of CGN distribution in *ex vivo* slices harboring the appropriate combinations of *VHL*^{flx/flx} and *Ptch*^{flx/flx} alleles revealed that *Ptch* deletion does not further enhance *VHL* loss of function phenotypes (Supplemental Figure 4B and see legend for detailed statistical analysis). *VHL* and *Ptch* deletion activates the Hif1 α or Shh signaling respectively as both are negative regulators of their respective pathways, therefore no additional or synergistic effects in this epistasis experiment place Hif1 α - and Shh-signaling in a common pathway modulating GNP neurogenesis. To further address the Shh-Hif1 α relationship in the context of hypoxia, we performed an additional pharmacological epistasis experiment using a small molecule inhibitor of GLI1 and GLI2 transcription factors (e.g. GANT68) that are the transcriptional effectors of the canonical, transcriptional arm of the Shh signaling cascade. Inhibition of GLI transcription factors does not rescue the 2% O₂ GZ occupancy phenotype (Supplemental Figure 4C and see legend for detailed statistical analysis), showing that while Shh and Hif1 α are part of a similar genetic

pathway controlling GNP proliferation, hypoxia can regulate the timing of CGN migration independently of Shh signaling.

The Hif α Pathway Controls CGN Differentiation, Migration timing, and Polarity via Zeb1

Having learned that the Hif1 α pathway supports GNP proliferation while negatively influencing GZ exit and CGN migration initiation, we next sought to identify potential targets in order to determine how hypoxia or the Hif1 α pathway mechanistically controls this balance. Our first clue regarding the mechanism came from comparing the transcriptomes of freshly purified CGNs from P0 and P15 to CGNs maintained in culture under hypoxic conditions (Supplemental Figure 5). These analyses showed that P0 CGNs and purified CGNs maintained in hypoxic culture exhibited similar degrees of immature gene expression, as compared to mature CGNs purified at P15, suggesting that low oxygen levels maintained CGNs in an immature, undifferentiated state. We gained further insight into how oxygen levels and the Hif1 α pathway control CGN differentiation by examining their relation to the Zeb1 transcription factor, an inhibitor of CGN differentiation (Singh et al., 2016). Interestingly, Zeb1 expression is not only activated by ischemic insults in the adult mouse brain (Bui et al., 2009) but is also positively regulated by Hif1 α in renal carcinoma (Krishnamachary et al., 2006). We reasoned that Zeb1 might be involved in the oxygen-homeostasis regulation of GNP differentiation or GZ exit. Accordingly, we first examined Zeb1 expression via immunostaining in *ex vivo* cerebellar slices in which the oxygen levels were manipulated. Slices incubated in 2% O₂ for 48 h showed an abundance of Zeb1-positive cells,

specifically in the EGL GZ niche, when compared to slices incubated in 20% O₂ (Figure 5A). Next, we prepared RNA from P7 GNPs nucleofected with LacZ (control), Hif1 α , or Zeb1 expression vectors and qRT-PCR analysis of CGNs overexpressing Hif1 α not only confirmed the expected increase in known Hif1 α targets such as *Bnip3*, *Hk2*, *VEGFa*, *PHD2*, and *PHD3*, but also showed a marked increase in *Zeb1* transcript expression, implicating Zeb1 as a mediator of Hif1 α regulation of GNP maturation (Figure 5B). Consistent with this model, we observed reduced NeuN expression and enhanced Zeb1 expression in CGNs from P7 *Atoh1-Cre:VHL^{flx/flx}* mice, in which the Hif1 α pathway is activated by the loss of VHL (Supplemental Figure 6). Indeed, Zeb1 expression continues in the IGL of VHL-deficient CGNs at P15, a developmental time-point at which its expression is extinguished in control animals (Supplemental Figure 6).

We assessed whether Hif1 α regulation of Zeb1 was direct by determining if Hif1 α binds the Zeb1 locus. Hif1 α CHiP-seq performed using chromatin harvested from highly pure, FACS isolated *Atoh1*-EGFP positive GNPs revealed four peaks of Hif1 α enriched reads denoting direct binding to a ~2.0 kb region surrounding the transcriptional start site of the Zeb1 gene (Figure 5C). Two of these peaks harbor evolutionarily conserved Hif1 α response elements (e.g., mouse vs. human) and were subjected to Hif1 α CHiP-PCR validation. Importantly, the peaks centered at -212 and +847 had equal or better binding than known/validated Hif1 α binding site in genes like *Vegf*, *Ldha* and *Pgk1* that also harbored peaks in the Hif1 α CHiP-Seq dataset (Figure 5D, control genomic region vs. -212 and +847 TTest P value < 0.01). Taken together

these results suggest that hypoxia regulates Zeb1 expression by direct binding of the Hif1 α to the Zeb1 promoter.

To further examine how the Hif1 α pathway controlled CGN differentiation, we performed a comparative analysis of the transcriptomes of cells overexpressing Hif1 α or Zeb1 via Affymetrix DNA arrays to gain insight into common mechanisms of GNP differentiation regulation. Our global analysis of transcripts revealed distinct patterns of gene expression, as would be expected for cells overexpressing the transcriptional repressor Zeb1 or the transcriptional activator Hif1 α . For example, the expression of a large group of genes that are activated by Hif1 α was unchanged in both the LacZ-expressing control and Zeb1-overexpressing cells (Figure 5E, left panel). Nevertheless, a group of transcripts were repressed by both Zeb1- and Hif1 α -expressing CGNs. Interestingly, two of the top 5 hits included two previously characterized Zeb1 targets, *Chl1* and *Lin7a*, that were recently shown by our laboratory to promote CGN differentiation [Figure 5E]. By clustering a large group of transcripts that are downregulated by both Zeb1 and Hif1 α to biological processes, using gene ontology terms, we discovered that many of the genes repressed in both sets of transcriptomes were related to classical hallmarks of early neuronal differentiation, such as neurogenesis, neuronal projection, and synaptic maturation, with the highest fold enrichment occurring for genes already known to be necessary and sufficient for neuronal migration (*DCC*, *CTTNBP2*, *NDE1*, *ATOH1*, *NAV1*, *NEUROD4*, *SYNE1*, *NEUROG2*, and *CHL1* [Figure 5F]). Consistent with this observation, qRT-PCR validation also showed that Zeb1 target genes such as *Chl1*, *Pard3*, and *Pard6a* were downregulated in the Hif1 α gain-of-function study (Figure 5B). Indeed, reduced *Chl1*, *Pard3*, and *Pard6a* expression

was also observed in CGNs from P7 *Atoh1-Cre:VHL^{flx/flx}* mice (Supplemental Figure 6). We have recently shown these genes to be the most critical Zeb1-repressed targets that control GNP polarization, differentiation, and GZ exit. Taken together, these results show that Hif1 α negatively regulates a group of genes implicated in neuronal maturation, and they suggest a working model that Hif1 α mechanistically mediates the timing of GZ exit via Zeb1 inhibition of polarity or migration genes (Figure 5G).

We recently showed that Zeb1 is necessary and sufficient to maintain the GNP state and GZ occupancy in a manner requiring Pard-complex transcriptional repression (Singh et al., 2016). We next sought to functionally assess whether Hif1 α controlled CGN migration initiation through Zeb1 or its target genes. To do this, we first tested whether Zeb1 loss of function could rescue the observed hypoxia-induced GZ exit delay. Electroporation of a validated, published mir30 based *Zeb1* shRNA (Singh et al., 2016) into the EGL of *ex vivo* cerebellar slices to silence Zeb1 function restored CGN displacement to the IGL in hypoxia (2% O₂), when Hif1 α HD was overexpressed or when VHL was deleted via Cre-mediated excision, suggesting that *Zeb1* acts downstream of *VHL* and *Hif1 α* and mediates the hypoxia-induced migration delay (Figure 6A). Finally, we co-electroporated Zeb1 and a Cre-encoding expression vector into cerebellar slices prepared from *Hif1 α ^{flx/flx}* cerebella. Zeb1 overexpression prevented precocious GZ exit and migration elicited by *Hif1 α* deletion, showing that elevated Zeb1 expression is sufficient to restore GZ occupancy to Hif1 α -deficient cells (Figure 6A). Not only do these results show that Zeb1 expression is activated by both hypoxia and elevated

Hif1 α activity, but our epistasis analysis reveals that Zeb1 is necessary for Hif1 α to promote GNP GZ occupancy.

Given that Hif1 α pathway activation simultaneously activated Zeb1 expression and suppressed Zeb1 target-gene expression (Figure 5B,G), we determined whether Zeb1 downstream targets (*Pard3*, *Pard6 α* , and *Chl1*) (Singh et al., 2016) were involved in Hif1 α pathway modulation of GZ occupancy or the hypoxia-induced delay of displacement to the IGL. Silencing the Pard-complex proteins *Pard3* or *Pard6 α* in Hif1 α -deficient CGNs inhibited the displacement to the IGL seen in *ex vivo* slices incubated in 2% O₂ in which *Hif1 α* had been genetically deleted (Figure 6B), showing that cell polarity gene function is required for GZ exit to proceed when CGNs are relieved of Hif1 α pathway-activity in hypoxia. We next tested whether *Pard3*, *Pard6 α* , or *Chl1* gain of function altered displacement to the IGL in cerebellar slices in which the Hif1 α pathway was activated by hypoxia, Hif1 α gain of function, or *VHL* deletion (Figure 6B). Whereas LacZ-expressing CGNs remained in the EGL GZ under all three experimental conditions, *Pard3*, *Pard6 α* , and *Chl1* rescued displacement to the IGL in all three modes of Hif1 α pathway activation (Figure 6B; see Supplemental Figure 7 for Hif1 α HD overexpression experiment plus compiled analysis of epistasis experiments and Supplemental Figure 3 for similar experiments in EGLN1- and EGLN3-deficient CGNs). Finally, we performed a structure function analysis on the *Par6 α* protein to determine whether the interaction with classical binding partners is required for enhanced polarity signaling to rescue a hypoxia phenotype. Singly introducing a panel *Pard6 α* cDNA mutants into *ex vivo* slices cultured at 2% O₂ revealed that the

Pard6 α PDZ domain, the aPKC- and Pard3-binding sites were essential for Pard6 α to rescue delayed GZ exit, suggesting Pard6 α acts in a concert with aPKC, Pard3 and ligands for its PDZ domain to support the initiation of CGN migration (Supplemental Figure 8). Surprisingly, a previously reported nuclear localization signal was also essential for Pard6 α to rescue delayed CGN migration, however the CRIB Cdc42 binding site was dispensable. The results of these epistasis and structure-function studies show that Hif1 α and hypoxia restraint of GNP GZ exit involves functional antagonism of neuronal polarization through a subset of classical Pard complex components like Pard6 α , Pard3 and aPKC. Pard-complex gain of function rescues the delay of GZ exit elicited by Hif1 α pathway activation, whereas Pard-complex loss of function restrains the early onset of migration elicited by *Hif1 α* loss of function. Taken together, these results suggest that early cerebellar hypoxia activates the Hif1 α pathway, which in turn stimulates Zeb1-mediated Pard-complex repression, thus gating the exit of GNPs from their GZ niche.

Antagonism Between Hif1 α -Zeb1 and the Pard Complex Controls GZ Occupancy via Integrin Extracellular Matrix Adhesion

Having found that Hif1 α and Zeb1 cooperate to negatively regulate Pard complex-dependent GZ exit, we sought to determine the downstream mechanisms by which oxygen homeostasis controlled GZ occupancy. Zeb1 is a key regulator of epithelial mesenchymal transition (EMT) in epithelia and developing GNPs. In many EMT paradigms, extracellular matrix (ECM) contacts driven by beta-1 integrin (Itg β 1)

receptors are favored over cell-cell adhesions such as tight or adherens junctions that pattern morphogenic movements of these cells (Baum et al., 2008; Shook and Keller, 2003). Spurred by classical electron microscopy studies that found that GNP maintain extensive contacts with the pial-derived ECM until they become postmitotic (Hausmann and Sievers, 1985) and control GNP mitogen responses (Blaess et al., 2004), we investigated whether integrin receptors were involved in GNP GZ exit. Although Zeb1 generally functions as a transcriptional repressor, we noted a 5.5 fold increase in *Itgβ1* mRNA expression in Zeb1-overexpressing CGNs (Figure 7A). We also surveyed the expression of *Itgβ1* in the cerebellum: at P7, *Itgβ1* expression was high in oEGL GNPs that co-expressed Zeb1 as well as focal adhesion kinase (FAK) phosphorylated on residue tyrosine 397 (phospho-FAK Y397), a marker that signals integrin activation and high mechanical tension when cells interact with ECM (Paszek et al., 2005) (Figure 7B). Given that Hif1α activates Zeb1 expression, we also tested whether hypoxia or Hif1α pathway activation affected integrin activity in GNPs or CGNs. Compared to control cells incubated under standard culture conditions (117.1 ± 21.1 cells/mm² cell density), purified CGNs incubated in 2% oxygen bound more strongly to a pure laminin substrate (179.0 cells/mm² cell density, t-test, $P < 0.0002$), an *Itgβ1* ECM ligand found at a high level in the basal lamina produced by pial fibroblasts (Figure 7C). Moreover, phospho-FAK Y397 was more abundant *in vivo* in the EGLs of mice in which *VHL* had been conditional deleted via *Atoh1-Cre* than in the EGLs of control mice, suggesting that integrin signaling is elevated when the Hif1α pathway is genetically activated (Figure 7D). The potential correlation between hypoxia or high Hif1α

pathway activity with elevated integrin adhesion led us to test whether *Itgβ1* was functionally involved in GZ exit. Cre-mediated deletion of floxed *Itgβ1* alleles rescued GNP GZ exit defects in *ex vivo* slices maintained in culture in 2% O₂ (Figure 7E, Cre^{active} \bar{x} = 40.5 ± 2.3 μm, Cre^{inactive} \bar{x} = 73.7 ± 4.4 μm, T-test, P<0.004). Moreover, *Itgβ1* gain of function via overexpression of a constitutively active V737N receptor–clustering mutant (Paszek et al., 2005) in *ex vivo* cerebellar slices was sufficient to restrain GNP GZ exit under culture conditions with the standard oxygen concentration (Figure 7F, Control \bar{x} distance = 64.4 ± 0.2 μm, whereas *Itgβ1* V737N OE \bar{x} distance = 35.4 ± 6.0 μm). Thus, not only does *Itgβ1* gain of function phenocopy *Hif1α* gain of function or hypoxia phenotypes, but *Itgβ1* loss is alone is also sufficient to restore GZ exit in hypoxic conditions.

We gained insights into *Itgβ1* regulation during GZ exit through our analysis of the changes in gene expression that accompany *Pard6α* rescue of *Zeb1*-overexpression phenotypes. Although our previous work showed that *Pard6α* rescues GNP differentiation and GZ exit defects linked to elevated *Zeb1* expression, *Pard6α* did not restore the expression of genes such as *Chl1* or *Pard3* that are actively repressed by *Zeb1* (Singh et al. 2016). Thus, the mechanism by which *Pard6α* rescues a *Zeb1* phenotype correlated with restored neuronal differentiation but could not be linked to a precise mechanism. Surprisingly, qRT-PCR showed that restored *Pard6α* expression in the context of *Zeb1* gain of function caused *Itgβ1* mRNA expression to decline to levels below those in unmanipulated CGNs (Figure 7A), suggesting that *Hif1α* pathway modulation of *Zeb1* simultaneously restrains neuronal polarity and promotes integrin

engagement. To address this question in GNPs, we FACS isolated pure progenitors from Atoh1-EGFP knock-in animals and incubated them at 2% O₂ in the presence or absence of echinomycin, a small molecule Hif1 α antagonist (Supplemental Figure 9A, B). Consistent with Hif1 α 's role in GNP neurogenesis (Figure 2), Hif1 α inhibition at 2% O₂ decreased the number of Atoh1-EGFP positive GNPs (Supplemental Figure 9C, D). Western blotting revealed that Hif1 α inhibition decreased Zeb1 and BNIP3 expression, increased α -internexin (a CGN differentiation marker) and Pard6 α expression and not only diminished Itg α 6 laminin receptor expression but also levels of the phospho-FAK Y397 marker for integrin engagement (Supplemental Figure 9E, F), supporting the Hif1 α pathway modulation of polarity and integrin engagement model.

Pard6 α inhibition of Zeb1 induced Itg β 1 expression suggested that Pard6 α functions to inhibit Itg β 1-mediated adhesion. To assess this possibility directly, we developed an assay to image GNP integrin-laminin focal contacts, using a LIM and SH3 protein 1 fusion protein (LASP1-Emerald). LASP1 is one of the few focal adhesion adaptor proteins specifically expressed in GNPs (according to the RIKEN brain transcriptome database (Sato et al., 2008) that also serves as a reporter for Itg β 1 focal adhesion to ECM substrates in non-neuronal cells (Lin et al., 2004). The resolution and signal-to-noise ratio of spinning-disk or confocal microscopy was insufficient to capture GNP focal adhesions or their dynamics (data not shown). Therefore, to perform our LASP1-Emerald phenotypic screen, we implemented the Structured Illumination (SIM) mode of Lattice Light-Sheet (LLS) microscopy, which uses ultrathin light sheets derived from optical lattices to rapidly

section cells grown in culture with minimal phototoxicity and provide near-isotropic imaging in the x, y, and z dimensions. Combinations of LASP1-Emerald, Hif1 α , Zeb1, and Pard6 α expression vectors were nucleofected into purified CGNs, which were maintained in culture on coverslips coated with laminin, and LLS-SIM time-lapse microscopy was used to assess the focal adhesion levels. After applying a Weka machine-learning approach (Arganda-Carreras et al., 2017) to quantitate the GNP focal adhesions, we found that both Hif1 α and Zeb1 gain of function alone led to a five- to six-fold increase in LASP1 focal adhesion density on a laminin substrate, when compared to control cells, confirming that both Hif1 α and Zeb1 gain of function act to enhance integrin adhesion (Figure 7G). Interestingly, Pard6 α expression in the context of Hif1 α or Zeb1 gain of function reversed LASP1 focal adhesion density to control levels. Finally, we assessed whether enhanced neuronal polarity modulated Itg β 1 mediated delay in GZ exit. Expression of Pard6 α rescued GZ exit in GNPs over-expressing Itg β 1 V737N receptor-clustering mutant (Paszek et al., 2005) in *ex vivo* cerebellar slices (Supplemental Figure 8C and see legend for detailed statistical analysis). Taken together, these results show not only that both Hif1 α and Zeb1 promote Itg β 1-based contacts that by themselves are sufficient to promote GNP GZ occupancy but also that Pard6 α facilitates GZ exit in part by inhibiting integrin adhesions. Thus, oxygen homeostasis in the developing cerebellum controls GZ exit gating via a mechanism involving Hif1 α negative regulation of the onset of neuronal polarization via Zeb1, which antagonizes Pard6 α inhibition of integrin contacts with pial-derived ECM components in the EGL niche.

DISCUSSION

Neuronal differentiation involves a complex interplay of extrinsic cues with intrinsic signaling pathways that support morphologic specialization, migration, and subsequent synaptic integration of post-mitotic neurons. Despite the intense focus on the function of genetically encoded morphogens, neurotrophic factors, or cell-surface cues on neuronal polarization and differentiation, the impact of simple environmental cues, such as oxygen tension, on these processes remains surprisingly unexplored at the cellular or molecular levels. We have found that a developmental switch in oxygen tension and the activity of the Hif1 α pathway balance germinal niche interaction and neuronal migration initiation by modulating neuronal polarization signaling molecules. Diminished Hif1 α pathway activity that accompanies postnatal vascularization helps release inhibition placed on polarity genes in neurons early in their development. Ultimately, GZ oxygen fluctuations control the affinity of immature neurons for niche extracellular matrix components versus the migration pathways that guide these maturing cells to their final laminar position.

Earlier studies have uncovered various configurations of developing neural cells and vascular elements. In many cases, the vasculature has been thought to provide positive trophic support for neural stem cells (Javaherian and Kriegstein, 2009; Palmer et al., 2000; Shen et al., 2004; Shen et al., 2008; Tavazoie et al., 2008), [but a lack of vasculature has recently been proposed to be critical to generating appropriate levels of cerebral cortical neural stem cell proliferation via the Hif1 \$\alpha\$ pathway controlling the metabolic status of the stem cell population](#)

(Lange et al., 2016). Moreover, the Hif1 α pathway controls oligodendrocyte maturation in manner that couples angiogenesis with optimal vascularization (Yuen et al., 2014). The profile of Hif1 α expression, hypoxypromoter labeling, and vascularization in the developing cerebellum indicates a complex switch in Hif1 α pathway activity, whereby an early epoch in GNP proliferation occurs mainly in a hypoxic environment, after which the period of CGN differentiation arises with a period of rapid vascularization. The EGL is unique in that this secondary germinal matrix, which is fated to vanish during development, is never fully vascularized by comparison with regions where mature neurons reside, such as the IGL or the mid- and hindbrains. This surprising finding introduces a new concept regarding the relation of developing neural cells to the vasculature: not only is poorly developed vasculature in specific lamina an arbiter of the overall maturation of neurons residing in that layer but, given that hypoxia potently inhibits GZ exit and migration, environmental conditions within the layer itself are a barrier to subsequent lamination that must be overcome as cells progress to their final position. Further studies are required to understand how cell types in the developing cerebellum communicate to regulate the onset of vascularization. Although it is clear that oligodendrocyte precursors are the source of signals that promote white-matter angiogenesis (Yuen et al., 2014), it is unknown what cell types contribute towards ML angiogenesis, as the ML is mostly free of oligodendrocytes, or how angiogenesis is coordinated with the developmental status of neuronal populations.

A number of studies have implicated hypoxia as a regulator of adult or embryonic neural stem cell self-renewal and quiescence (Lange et al., 2016; Mazumdar et al., 2010; Mohyeldin et al., 2010; Morrison et al., 2000; Panchision, 2009; Simon and Keith, 2008; Studer et al., 2000). To our knowledge, the role of the Hif1 α pathway or hypoxia in regulating neuronal differentiation and, especially, polarization is unexplored. We have now provided multiple levels of evidence based on Hif1 α pathway gain of function or loss of function to support the hypothesis of Hif1 α not only regulates neuronal differentiation but also key milestones of the post-mitotic state: First, the Hif1 α pathway is necessary and sufficient to maintain peak levels of actively cycling GNPs *in vivo*. Indeed, the loss of Hif1 α increased the fraction of GNPs exiting the cell cycle even when mitogens such as sonic hedgehog were present. Second, the Hif1 α pathway controls the timing of GZ exit and radial migration initiation, which occurs only when CGNs have entered the postmitotic phase of their differentiation. Third, hypoxia and Hif1 α elevate Zeb1 expression while simultaneously repressing differentiation markers such as Pard6 α , Pard3, and other genes required for neuronal maturation. Fourth, Hif1 α pathway activation maintains the affinity of CGNs for Itg β 1 substrates, which is a hallmark of GZ-resident CGNs. Whereas earlier studies implicated Hif1 α in indirect effects on non-neuronal cell differentiation through paracrine or autocrine modulation of BMP or Wnt signaling (Mazumdar et al., 2010), our findings have identified a well-defined cluster of Hif1 α -regulated genes that represent a cell-autonomous pathway controlling neuronal cell differentiation.

Our work highlights a significant conceptual shift in the understanding of cell polarity regulation. The field had previously focused on post-translational rheostat-like polarity signaling mechanisms based on polarity protein phosphorylation and asymmetric subcellular partitioning of signaling complexes that were classically influenced by how polarity is regulated in invertebrate model systems (McCaffrey and Macara, 2009; Namba et al., 2015). Recent studies in vertebrates have revealed diverse polarity regulatory mechanisms, including global switch-like mechanisms whereby polarity competency is modulated through the overall expression levels of polarity genes, as in polarity inhibition by microRNAs, ubiquitin ligases (Cheng et al., 2011; Famulski et al., 2010; Laumonnerie and Solecki, 2018), and now Hif1 α -Zeb1-mediated transcriptional repression. Unexpectedly, Hif1 α regulation of Pard-complex function via Zeb1 is the first known example of cellular polarity modulation by oxygen tension during development, whether in the nervous system or elsewhere. Our data suggest a model in which low oxygen tension in the cerebellum before P10 leads to elevated Hif1 α and Zeb1 activity that antagonizes Pard-complex gene expression in immature cells of the CGN lineage (Supplemental Figure 10). Subsequent elevation of oxygen tension, presumably through postnatal vascularization, leads to diminished repression of polarity genes by Hif1 α -Zeb1, ultimately leading to GZ exit and migration initiation. Mechanistically, our results also show that the Pard complex allows GNPs to release Itg β 1 focal adhesive contacts with pial-derived ECM substrates, a function that complements its role in promoting Jam-C-dependent CGN-CGN or CGN-Bergmann glial adhesion, which allows these cells to exit their germinal niche

(Famulski et al., 2010; Singh et al., 2016). Thus, the Pard complex not only regulates multiple adhesive substrate affinities during GZ exit and migration but is also the developmental switch in cerebellar oxygen tension and profoundly affects the polarity-mediated, stage-specific adhesion choices made during neuronal maturation. Interestingly, Hif1 α and Itg β 1 loss of function both reduce GNP sensitivity to mitogen signaling (Blaess et al., 2004; Nguyen et al., 2018), suggesting that further investigation of the oxygen tension–cell polarity–ECM interactions will yield insights into not only how these interactions maintain appropriate levels of neuronal differentiation but also provide more insights into how oxygen shapes neuronal circuit formation.

The finding that oxygen tension regulates the cell polarization status of developing neurons has implications beyond GZ occupancy and radial migration initiation; it suggests that crucial polarity-controlled events in neurons, such as spindle orientation during neural stem-cell division, axon-dendrite specification, or adhesive events that promote synaptogenesis, may also be regulated by oxygen tension (Singh and Solecki, 2015; Uzquiano et al., 2018). This paradigm is particularly relevant to neurodevelopmental abnormalities associated with pre-term birth, in which perinatal hypoxia leads to underdevelopment and damage to sensitive populations of immature neurons and glial cells (Salmaso et al., 2014). Indeed, recent neuroimaging studies have noted neuronal heterotopias in the brains of children with vascular defects. Interestingly, the classical function of polarity signaling cascades in non-neural tissues is to maintain the homeostasis of epithelial or vascular endothelial tight and adherens junctions; thus, hypoxic

inhibition of cell polarity may also be related to the vascular leakage and hemorrhage associated with hypoxic insult to the brain. Hypoxic inhibition of polarity signaling cascades not only may provide a molecular entry point through which to mechanistically dissect the pathogenesis associated with perinatal hypoxia but also suggests a treatment strategy based on promoting cell polarity that may be useful to support healthy brain development in preterm infants.

AUTHOR CONTRIBUTIONS

JK, NT and DH carried out *ex vivo* studies, epistasis analyses and prepared many figures. JK performed all *in vivo* studies. VN and DHR provided VHL deficient cerebella. DRS spearheaded LLS SIM microscopy implementation and developed Lavisision Ultramicroscope imaging protocols. NT carried out iDisco clearing, while JK carried out Clarity clearing studies. NT carried out all *ex vivo* slice imaging. JK, NT and DH used an algorithm developed by CL in Amira to analyze all fixed and live cell migration experiments. AS designed and implemented computational methods to analyze iDisco and LLS-SIM experiments. JK, NT, DH, DHR participated in conceptual study design. DJS conceived of the study, participated in its design and coordination and performed all LLS-SIM imaging studies. All authors drafted or edited the manuscript.

DECLARATION OF INTERESTS: None to declare.

ACKNOWLEDGEMENTS: The Lattice Light Sheet Microscope referenced in this research was used under license from Howard Hughes Medical Institute, Janelia Research Campus. We thank the Cell and Tissue Imaging Core of St. Jude

Children's Research Hospital for assistance implementing for additional imaging support and David Finkelstein for bioinformatics support. Keith A. Laycock, PhD, ELS edited the manuscript. Felizza Gunderson Ph.D., Maddy Craske Ph.D. and Paul Labhart Ph.D. from ActiveMotif provided invaluable support designing and carrying out CHIP-PCR and CHIP-Seq experiments plus analysis. JAK was supported by a post-doctoral fellowship from the Deutsche Forschungsgemeinschaft (KU 3253/1-1 and KU 3253/2-1). Solecki laboratory is funded by the American Lebanese Syrian Associated Charities (ALSAC) and by grants 1R01NS066936 and R01NS104029 from the National Institute of Neurological Disorders (NINDS). The Rowitch laboratory is funded by grant P01NS08351 from NINDS. The content is solely the responsibility of the authors and does not necessarily represent the official views of the NINDS or the NIH.

STAR METHODS

Animals

All mouse lines were maintained in standard conditions in accordance with guidelines established and approved by the Institutional Animal Care and Use Committee at St. Jude Children's Research Hospital (Protocol no. 483). Atoh1-cre/Esr1*14Fsh/J, EglN1^{tm1KaeI}/J, B6.129-Hif1a^{tm3Rsjo}/J, C;129S-Vhl^{tm1Jae}/J and B6.129S-Atoh1tm4.1Hzo/J mouse strains were obtained from The Jackson Laboratory.

Plasmid vectors

All cDNAs encoding proteins of interest were commercially synthesized and subcloned into pCIG2 by GenScript (Piscataway, NJ). Expression plasmids for Pard3, Pard6 α , Jam-C-Nectin3, and fluorescent fusion proteins such as pCIG2 H2B-mCherry, pCIG2 RFP-UTRCH, pCIG2 Centin2-Venus, and pCIG2 JAM-C-pHluorin were subcloned as previously described ([Solecki et al., 2009](#)).

Preparation and nucleofection of CGNs

CGNs were prepared as previously described ([Hatten, 1985](#)). Briefly, cerebella were dissected from the brains of P7 mice and the pial layer removed, then the tissue was treated with a Neural Tissue Dissociation Kit (Miltenyi Biotec) and triturated into a single-cell suspension by using fine-bore Pasteur pipettes. The suspension was layered onto a discontinuous Percoll gradient and separated by centrifugation. The small-cell fraction was then isolated. The resulting cultures routinely contained 95% CGNs and 5% glia. Expression vectors encoding fluorescently labeled nuclear proteins and pCIG2 expressing proteins of interest were introduced into granule neurons via Amaxa nucleofection, using an Amaxa Mouse Neuron Nucleofector Kit in accordance with the manufacturer's instructions and program A005. The concentration of pCIG2 expression vectors used was determined such that there would be at least a two-fold increase in protein expression. After cells had been allowed to recover from the nucleofection for 10 min, they were plated in 6-cm dishes coated with low concentrations of poly-L-

ornithine to facilitate the attachment of neurons to glial processes (according to methods established by Edmondson and Hatten, 1987)

Ex vivo cerebellar electroporation, organotypic slice culture, and imaging

P7 cerebella were dissected, soaked in endotoxin-free plasmid DNA suspended in Hank's balanced salt solution (1–3 µg/µL of each DNA was generally used, with pCIG2-mCherryH2B being electroporated as a nuclear marker for migrating CGNs), transferred to a CUY520-P5 platinum-block petri-dish electrode (Protech International), and electroporated with a CUY21EDIT square-wave electroporator (80 V, 5 pulses, 50-ms pulse, 500-ms interval) (Protech International). Electroporated cerebella were embedded in 4% low-melting-point agarose and 300-µm sagittal cerebellar slices were prepared using a VT1200 Vibratome (Leica Microsystems). Slices were transferred to Millicell tissue culture inserts (Millipore) and incubated in basal Eagle medium supplemented with 2 mM L-glutamine, 0.5% glucose, 50 U/mL penicillin-streptomycin, and 1× B27 and 1× N2 supplements (Invitrogen) at the air-medium interface for the times indicated in the figures.

Previous characterization of this method had shown that more than 97% of the electroporated cells were Pax6-positive CGNs in the outer EGL (Famulski et al., 2010). To measure the migration distance of CGNs, cerebellar slices were fixed with 4% paraformaldehyde and mounted on slides by using ProLong Gold (Invitrogen). The migration distance was measured as the distance between the cerebellar pial surface and the center of individual cell nuclei marked by mCherry-H2B. Measurements were made using a self-written program in the Amira software. Statistical analysis used Microsoft Excel, and graphs were prepared with

KaleidaGraph v4.03 (Synergy Software). For live-imaging analysis of the migration of H2B-mCherry–labeled CGNs, slice cultures were transferred at 18 h to the humidified chamber of the spinning-disk confocal microscope described above. Z-stacks (60–80 μm in width, approximately 20 sections per stack) were collected at multiple x, y stage positions every 15 min for 24–48 h.

Slice movie analysis

The nuclei of neurons were tracked manually over the course of the movie by using Slidebook 6 (Intelligent Imaging Innovations) and a Marianas Spinning Disk confocal microscope. The distance from the edge (DFE) of the slice was computed using Amira 6.2 (FEI, Thermo Fisher Scientific) and added as an intensity channel to the respective movie. Only movies in which the overall XY drift was limited to 5 μm were considered in the analysis. Nuclear coordinates (X, Y, DFE) tracked at each time-point were exported to Excel (Microsoft) in order to plot the distance distribution for each time-point and calculate the instant speed average and average distance variation. Angles were calculated from the distance variation and instant speed vectors at each time-point. Data were divided into layers based on extrapolated measurements from histologic sections at P7, i.e., oEGL: 0–30 μm ; iEGL: 30–50 μm ; ML: 50–100 μm ; and IGL: >100 μm , based on their DFE at a given time-point.

Lattice light-sheet structured illumination microscopy (LLS-SIM).

Images were acquired on a lattice light-sheet microscope in the Developmental Neurobiology Department's Neuroimaging Laboratory. The specialized optics of this instrument have been described by Chen and coworkers (Chen et al., 2014). The optics used for the experiments described herein included the following: 560- and 488-nm laser lines, with maximum power of 500 mW and 300 mW, respectively, and a quad-band emission filter to resolve spectrally the imaged channels.

The LLS was aligned each morning, allowing at least 4 h for thermal equilibration after the heating apparatus was activated. All the cell samples were imaged in Fluorobrite low-fluorescence medium supplemented with 10% heat-inactivated horse serum, to which the spherical aberration correction parameter of the objective was adjusted. Cells were seeded on 5-mm coverslips and mounted in custom-fabricated sample holders for imaging. Images were acquired with the Slidebook software package, using a custom-designed 15 μm -square light-sheet pattern in the 5-phase structured illumination z-galvo and objective scan mode, with both colors being captured at each z position. The acquired images were background subtracted, then high-resolution SIM images were generated using an open-source, GPU-accelerated SIM reconstruction software with freshly acquired optical transfer functions (OTFs) generated on each day of imaging (Chen et al., 2014; Rego and Shao, 2015). Weka-mediated machine learning in Fiji was then used to analyze the numbers of LASP1-Emerald focal adhesions in maximum-intensity projections of LLS-SIM 3D volumes to determine the effects of Zeb1 or Hif1 α overexpression on integrin-mediated adhesion.

Gene expression analyses: Flow cytometry, RNA isolation, RT-PCR, and Affymetrix arrays

To obtain a pure population of GNP_s expressing the protein of interest, GNP_s isolated from cerebella of postnatal day 7 (P7) mice were nucleofected with pCIG2 H2B-mCherry (to label cells red [control]) or mCherry with Hif1 α or Zeb1, maintained in culture for 24 h, triturated into a single-cell suspension, and stained with DAPI. Sorting of viable mCherry-positive cells was carried out in the Shared Resource flow cytometry facility at St. Jude, using a BD Aria III SORP sorter. A bandpass 610/20 filter was used to detect mCherry signals during excitation at 561 nm. The cells were directly collected in the lysis buffer, and RNA was extracted with an Ambion RNAqueous Kit (Austin, TX). In accordance with the manufacturer's instructions, each sample was isolated in 40 μ L of elution buffer and treated with DNase (Ambion) to eliminate any genomic contamination. The quantity and quality of the isolated RNA was checked using an Agilent 2100 Bioanalyzer with RNA 6000 Nano Chips (Agilent Technologies, Santa Clara, CA). Primer sets for each gene were designed with Primer Express Software (Applied Biosystems, Foster City, CA) and synthesized (IDT, Coralville, IA). RNA amplification and reverse transcription were performed with the WT-Ovation RNA Amplification System (NuGEN) in accordance with the manufacturer's instructions. Two-step real-time RT-PCR was performed with an ABI PRISM 7900 Sequence Detection System, using the SYBR Green PCR Master Mix (Applied Biosystems), as described previously ([Singh et al., 2010](#)). Data were normalized to the 18S ribosomal RNA and actin expression levels in each sample.

RNA quality and microarray analyses were performed by the microarray core facility at St Jude. RNA quality was analyzed with an Agilent 2100 Bioanalyzer, and all samples had an RIN of less than 8. A 100-ng sample of total RNA was processed using an Affymetrix 3' IVT Express Kit. Biotin-labeled cRNAs were hybridized to the Affymetrix GeneChip HT MG-430 PM array, then washed, stained, and scanned on a GeneTitan instrument (Affymetrix). Data were summarized using Affymetrix Expression Console software (v1.1) to apply the robust multi-array average (RMA) algorithm (ArrayExpress accession no. E-MTAB-3557). The arrays were RMA normalized and batch corrected with R/ComBat. Unsupervised hierarchical clustering analysis and principal component analysis was performed with Spotfire and GeneMaths. Differentially expressed genes were analyzed using a linear models algorithm (R/Limma). Differentially expressed genes in Hif1 α - and Zeb1-overexpressing cells were selected by using an FDR-corrected *P*-value (*q*-value) of 0.05 and a fold change of 1.5 as the cutoffs. GO analysis was performed with the DAVID Bioinformatics Resource for the common upregulated genes in Hif1 α - and Zeb1-overexpressing cells.

Cerebellar immunohistochemistry

Postnatal brains were fixed by immersion in 4% paraformaldehyde at 4°C overnight, followed by cryoprotection in PBS containing 30% sucrose. Histologic sagittal sections were cut on a cryostat and pre-blocked for 1 h in PBS with 0.1% Triton X-100 and 10% normal donkey serum. Sections were incubated overnight at 4°C with the primary antibodies. This was followed by incubation for 1 h with the appropriate Alexa Fluor–labeled secondary antibody (Invitrogen; diluted 1:1000)

before mounting. For cell proliferation assays, mice were injected intraperitoneally with 50 mg/kg EdU, and EdU incorporation was assayed with the Click-iT assay (Invitrogen) in accordance with the manufacturer's instructions. To detect organs and cells low in oxygen, mice were injected intraperitoneally with 60 mg/kg pimonidazole hydrochloride 2 h before they were euthanized, and binding of the compound was visualized with the Hypoxyprobe-1 Omni kit. GluT1 staining required tissue to be cleared with the CLARITY method and was essentially performed as described at <http://wiki.claritytechniques.org>.

iDisco clearing

EGFP-Atoh1-expressing p7 brains were stained to visualize their vasculature by using the iDisco protocol (<https://idisco.info/idisco-protocol/>). Briefly, the P7 brains were dissected and trimmed down to leave the hindbrain, cerebellum, and midbrain intact. The brains were fixed in PFA and then underwent pretreatment and bleaching with methanol/dichloromethane (DCM) and H₂O₂ in accordance with the protocol. Permeabilization and blocking steps were carried out for 3 days each at 37°C. Samples were then immunolabeled with chick anti-GFP antibody (EMD Millipore, diluted 1:1000) (to label EGFP-Atoh1) and rabbit anti-GLUT-1 (Aves, diluted 1:500) (to label blood vessels). Both primary and appropriate secondary antibodies (Alexa donkey anti-rabbit 555 [LifeTechnologies, diluted 1:500] and donkey anti-chick 647 [Jackson ImmunoResearch, diluted 1:500]) were incubated with the brains for 6 days at 37°C. Samples were then cleared using the methanol/DCM/dibenzyl ether (DBE) treatment outlined in the protocol. Imaging of staining was carried out on a LaVision Ultramicroscope II, using 3-µm step sizes

at 0.63× magnification. Images were processed and rendered in Arivis 4D (Arivis AG).

Atoh1-eGFP sorted cells analysis of polarity protein expression.

Pups homozygous for Atoh1-eGFP (B6.129S-Atoh1tm4.1Hzo/J, The Jackson Laboratory, JAX: 013593) were collected at P7, and cerebellar granule neurons were isolated following the dissociation methods described above. Progenitors were sorted based on their high GFP intensity with a cell sorter (FACSAria Fusion, BD Biosciences, 85µm nozzle 35PSI). Sample for CHiP PCR or CHiP-Seq were snap frozen. GNPs used for validation of Zeb1, Pard protein and integrin related protein expression profiles were cultured for 24h on Laminin (2µg.µm⁻², EMD Millipore, Chemicon, Cat# CC095) at 2% O₂ in presence of DMSO or Echinomycin (Fresh batch for each replicates, Tocris, Cat# 5520). Proteins were isolated from cell lysate and reduced in Laemmli buffer (Sigma-Aldrich, Cat# S3401) prepared to then loaded on gel for Western Blot analysis (antibody and concentration provided in the key resource table) using the quantitative Li-COR Biotechnology system. Band intensity was measured and analyzed with Image Studio (Li-COR Biotechnology) and each signal was normalized using total protein stain (Revert™ 700 Total Protein Stain Kits, Li-COR Biotechnology, Cat# P/N 926-11016).

Expression analysis for Hif1α protein or Hypoxyprobe levels

Nuclear and cytoplasmic protein fractions were extracted with NE-PER Nuclear and Cytoplasmic Extraction Reagent (Thermo Fisher Scientific). Protein lysates were denatured for 5 min with NuPAGE sample-reducing agent (LifeTech) and loading buffer heated to 75°C. Samples were subjected to electrophoresis on SDS-

PAGE 4–12% Bis-Tris gels (LifeTech). Proteins were electroblotted onto polyvinylidene fluoride membranes by using a Gel Transfer Device (Invitrogen). Membranes were dried, activated with methanol, blocked for 1 h at room temperature with Odyssey Blocking buffer diluted 1:2 in TBS, and incubated with the indicated antibodies at 4°C overnight. Odyssey secondary IR antibodies (diluted 1:10000) were used for detecting proteins with the Odyssey Infrared Imaging System.

Chromatin Immunoprecipitation

Atoh1-EGFP positive GNPs were fixed with 1% formaldehyde for 15 min and quenched with 0.125 M glycine. Chromatin was isolated by the addition of lysis buffer, followed by disruption with a Dounce homogenizer. Lysates were sonicated and the DNA sheared to an average length of 300-500 bp. Genomic DNA (Input) was prepared by treating aliquots of chromatin with RNase, proteinase K and heat for de-crosslinking, followed by ethanol precipitation. An aliquot of chromatin (10 ug) was precleared with protein A agarose beads (Invitrogen). Genomic DNA regions of interest were isolated using 5 µg of antibody against HIF1a (Abcam, ab2185, Lot GR3239692-1). Complexes were washed, eluted from the beads with SDS buffer, and subjected to RNase and proteinase K treatment. Crosslinks were reversed by incubation overnight at 65°C, and CHIP DNA was purified by phenol-chloroform extraction and ethanol precipitation. Quantitative PCR (QPCR) reactions were carried out in triplicate on specific genomic regions using SYBR Green Supermix (Bio-Rad). The resulting signals were normalized for primer efficiency by carrying out QPCR for each primer pair using Input DNA.

Illumina ChIP Sequencing

Illumina sequencing libraries were prepared from the ChIP and Input DNAs by the standard consecutive enzymatic steps of end-polishing, dA-addition, and adaptor ligation. Steps were performed on an automated system (Apollo 342, Wafergen Biosystems/Takara). After a final PCR amplification step, the resulting DNA libraries were quantified and sequenced on Illumina's NextSeq 500 (75 nt reads, single end). Reads were aligned to the mouse genome (mm10) using the BWA algorithm (default settings). Duplicate reads were removed and only uniquely mapped reads (mapping quality ≥ 25) were used for further analysis. Alignments were extended in silico at their 3'-ends to a length of 200 bp, which is the average genomic fragment length in the size-selected library, and assigned to 32-nt bins along the genome. The resulting histograms (genomic "signal maps") were stored in bigWig files. Peak locations were determined using the MACS algorithm (v2.1.0) with a cutoff of p-value = $1e-7$. Peaks that were on the ENCODE blacklist of known false ChIP-Seq peaks were removed. Signal maps and peak locations were used as input data to Active Motifs proprietary analysis program, which creates Excel tables containing detailed information on sample comparison, peak metrics, peak locations and gene annotations.

Statistical analysis

All data are expressed as the mean \pm SE. Student's *t*-test was used for comparing two groups, and the one-way analysis of variance and Holm-Sidak post-hoc test was used for multiple comparisons, with the level of statistical significance being set at $P < 0.01$ unless otherwise specified. In migration rescue assays, if the

rescuing conditions resulted in a χ^2 -test *P*-value greater than 0.8 when compared to controls and a *t*-test *P*-value of less than 0.01 when compared to Zeb1 overexpression alone, they were considered to have achieved rescue.

REFERENCES

Arganda-Carreras, I., Kaynig, V., Rueden, C., Eliceiri, K.W., Schindelin, J., Cardona, A., and Sebastian Seung, H. (2017). Trainable Weka Segmentation: a machine learning tool for microscopy pixel classification. *Bioinformatics* 33, 2424-2426.

Ayala, R., Shu, T., and Tsai, L.H. (2007). Trekking across the brain: the journey of neuronal migration. *Cell* 128, 29-43.

Barnes, A.P., and Polleux, F. (2009). Establishment of axon-dendrite polarity in developing neurons. *Annual review of neuroscience* 32, 347-381.

Baum, B., Settleman, J., and Quinlan, M.P. (2008). Transitions between epithelial and mesenchymal states in development and disease. *Seminars in cell & developmental biology* 19, 294-308.

Blaess, S., Graus-Porta, D., Belvindrah, R., Radakovits, R., Pons, S., Littlewood-Evans, A., Senften, M., Guo, H., Li, Y., Miner, J.H., *et al.* (2004). Beta1-integrins are critical for cerebellar granule cell precursor proliferation. *J Neurosci* 24, 3402-3412.

Bui, T., Sequeira, J., Wen, T.C., Sola, A., Higashi, Y., Kondoh, H., and Genetta, T. (2009). ZEB1 links p63 and p73 in a novel neuronal survival pathway rapidly induced in response to cortical ischemia. *PloS one* 4, e4373.

Chen, B.C., Legant, W.R., Wang, K., Shao, L., Milkie, D.E., Davidson, M.W., Janetopoulos, C., Wu, X.S., Hammer, J.A., 3rd, Liu, Z., *et al.* (2014). Lattice light-sheet microscopy: imaging molecules to embryos at high spatiotemporal resolution. *Science* 346, 1257998.

Cheng, P.L., Lu, H., Shelly, M., Gao, H., and Poo, M.M. (2011). Phosphorylation of E3 ligase Smurf1 switches its substrate preference in support of axon development. *Neuron* 69, 231-243.

Cooper, J.A. (2013). Cell biology in neuroscience: mechanisms of cell migration in the nervous system. *The Journal of cell biology* 202, 725-734.

Falk, S., Bugeon, S., Ninkovic, J., Pilz, G.A., Postiglione, M.P., Cremer, H., Knoblich, J.A., and Gotz, M. (2017). Time-Specific Effects of Spindle Positioning on Embryonic Progenitor Pool Composition and Adult Neural Stem Cell Seeding. *Neuron* 93, 777-791 e773.

Famulski, J.K., Trivedi, N., Howell, D., Yang, Y., Tong, Y., Gilbertson, R., and Solecki, D.J. (2010). Siah regulation of Pard3A controls neuronal cell adhesion during germinal zone exit. *Science* 330, 1834-1838.

Gossage, L., Eisen, T., and Maher, E.R. (2015). VHL, the story of a tumour suppressor gene. *Nature reviews Cancer* 15, 55-64.

Hatten, M.E. (2002). New directions in neuronal migration. *Science* 297, 1660-1663.

Hatten, M.E., and Roussel, M.F. (2011). Development and cancer of the cerebellum. *Trends Neurosci* 34, 134-142.

Hausmann, B., and Sievers, J. (1985). Cerebellar external granule cells are attached to the basal lamina from the onset of migration up to the end of their proliferative activity. *J Comp Neurol* 241, 50-62.

Ivan, M., and Kaelin, W.G., Jr. (2017). The EGLN-HIF O₂-Sensing System: Multiple Inputs and Feedbacks. *Molecular cell* 66, 772-779.

Javaherian, A., and Kriegstein, A. (2009). A stem cell niche for intermediate progenitor cells of the embryonic cortex. *Cereb Cortex* 19 Suppl 1, i70-77.

Kaelin, W.G., Jr. (2008). The von Hippel-Lindau tumour suppressor protein: O₂ sensing and cancer. *Nature reviews Cancer* 8, 865-873.

Kaelin, W.G., Jr., and Ratcliffe, P.J. (2008). Oxygen sensing by metazoans: the central role of the HIF hydroxylase pathway. *Molecular cell* 30, 393-402.

Knobloch, M., and Jessberger, S. (2017). Metabolism and neurogenesis. *Current opinion in neurobiology*.

Kohwi, M., and Doe, C.Q. (2013). Temporal fate specification and neural progenitor competence during development. *Nat Rev Neurosci* 14, 823-838.

Kreshuk, A., Straehle, C.N., Sommer, C., Koethe, U., Cantoni, M., Knott, G., and Hamprecht, F.A. (2011). Automated detection and segmentation of synaptic contacts in nearly isotropic serial electron microscopy images. *PloS one* 6, e24899.

Krishnamachary, B., Zagzag, D., Nagasawa, H., Rainey, K., Okuyama, H., Baek, J.H., and Semenza, G.L. (2006). Hypoxia-inducible factor-1-dependent repression of E-cadherin in von Hippel-Lindau tumor suppressor-null renal cell carcinoma mediated by TCF3, ZFH1A, and ZFH1B. *Cancer Res* 66, 2725-2731.

Lange, C., Turrero Garcia, M., Decimo, I., Bifari, F., Eelen, G., Quaegebeur, A., Boon, R., Zhao, H., Boeckx, B., Chang, J., *et al.* (2016). Relief of hypoxia by angiogenesis promotes neural stem cell differentiation by targeting glycolysis. *The EMBO journal* 35, 924-941.

Laumonnerie, C., and Solecki, D.J. (2018). Regulation of Polarity Protein Levels in the Developing Central Nervous System. *J Mol Biol.*

Lewis, T.L., Jr., Courchet, J., and Polleux, F. (2013). Cell biology in neuroscience: Cellular and molecular mechanisms underlying axon formation, growth, and branching. *The Journal of cell biology* 202, 837-848.

Lin, Y.H., Park, Z.Y., Lin, D., Brahmabhatt, A.A., Rio, M.C., Yates, J.R., 3rd, and Klemke, R.L. (2004). Regulation of cell migration and survival by focal adhesion targeting of Lasp-1. *The Journal of cell biology* 165, 421-432.

Mazumdar, J., Mazumdar, J., O'Brien, W.T., O'Brien, W.T., Johnson, R.S., Johnson, R.S., LaManna, J.C., LaManna, J.C., Chavez, J.C., Chavez, J.C., *et al.* (2010). O₂ regulates stem cells through Wnt/ β -catenin signalling. *Nature cell biology* 12, 1007-1013.

McCaffrey, L.M., and Macara, I.G. (2009). Widely conserved signaling pathways in the establishment of cell polarity. *Cold Spring Harb Perspect Biol* 1, a001370.

Metin, C., Vallee, R.B., Rakic, P., and Bhide, P.G. (2008). Modes and mishaps of neuronal migration in the mammalian brain. *The Journal of neuroscience : the official journal of the Society for Neuroscience* 28, 11746-11752.

Mohyeldin, A., Garzón-Muvdi, T., and Quiñones-Hinojosa, A. (2010). Oxygen in Stem Cell Biology: A Critical Component of the Stem Cell Niche. *Cell Stem Cell* 7, 150-161.

Morrison, S.J., Csete, M., Groves, A.K., Melega, W., Wold, B., and Anderson, D.J. (2000). Culture in Reduced Levels of Oxygen Promotes Clonogenic Sympathoadrenal Differentiation by Isolated Neural Crest Stem Cells. *Journal of Neuroscience* 20, 7370-7376.

Nakayama, K., Frew, I.J., Hagensen, M., Skals, M., Habelhah, H., Bhoumik, A., Kadoya, T., Erdjument-Bromage, H., Tempst, P., Frappell, P.B., *et al.* (2004). Siah2 regulates stability of prolyl-hydroxylases, controls HIF1 α abundance, and modulates physiological responses to hypoxia. *Cell* 117, 941-952.

Nakayama, K., and Ronai, Z. (2004). Siah: new players in the cellular response to hypoxia. *Cell Cycle* 3, 1345-1347.

Namba, T., Funahashi, Y., Nakamuta, S., Xu, C., Takano, T., and Kaibuchi, K. (2015). Extracellular and Intracellular Signaling for Neuronal Polarity. *Physiol Rev* 95, 995-1024.

Nguyen, V., Sabeur, K., Maltepe, E., Ameri, K., Bayraktar, O., and Rowitch, D.H. (2018). Sonic Hedgehog Agonist Protects Against Complex Neonatal Cerebellar Injury. *Cerebellum* 17, 213-227.

Palmer, T.D., Willhoite, A.R., and Gage, F.H. (2000). Vascular niche for adult hippocampal neurogenesis. *The Journal of comparative neurology* 425, 479-494.

Panchision, D.M. (2009). The role of oxygen in regulating neural stem cells in development and disease. *Journal of cellular physiology* 220, 562-568.

Paszek, M.J., Zahir, N., Johnson, K.R., Lakins, J.N., Rozenberg, G.I., Gefen, A., Reinhart-King, C.A., Margulies, S.S., Dembo, M., Boettiger, D., *et al.* (2005). Tensional homeostasis and the malignant phenotype. *Cancer cell* 8, 241-254.

Rasin, M.R., Gazula, V.R., Breunig, J.J., Kwan, K.Y., Johnson, M.B., Liu-Chen, S., Li, H.S., Jan, L.Y., Jan, Y.N., Rakic, P., *et al.* (2007). Numb and Numbl are required for maintenance of cadherin-based adhesion and polarity of neural progenitors. *Nature neuroscience* 10, 819-827.

Rego, E.H., and Shao, L. (2015). Practical structured illumination microscopy. *Methods Mol Biol* 1251, 175-192.

Rose, M.F., Ren, J., Ahmad, K.A., Chao, H.T., Klisch, T.J., Flora, A., Greer, J.J., and Zoghbi, H.Y. (2009). Math1 is essential for the development of hindbrain neurons critical for perinatal breathing. *Neuron* 64, 341-354.

Ruiz de Almodovar, C., Coulon, C., Salin, P.A., Knevels, E., Chounlamountri, N., Poesen, K., Hermans, K., Lambrechts, D., Van Geyte, K., Dhondt, J., *et al.* (2010). Matrix-binding vascular endothelial growth factor (VEGF) isoforms guide granule cell migration in the cerebellum via VEGF receptor Flk1. *J Neurosci* 30, 15052-15066.

Salmaso, N., Jablonska, B., Scafidi, J., Vaccarino, F.M., and Gallo, V. (2014). Neurobiology of premature brain injury. *Nature neuroscience* 17, 341-346.

Sato, A., Sekine, Y., Saruta, C., Nishibe, H., Morita, N., Sato, Y., Sadakata, T., Shinoda, Y., Kojima, T., and Furuichi, T. (2008). Cerebellar development transcriptome database (CDT-DB): profiling of spatio-temporal gene expression during the postnatal development of mouse cerebellum. *Neural Netw* 21, 1056-1069.

Semenza, G.L., Shimoda, L.A., and Prabhakar, N.R. (2006). Regulation of gene expression by HIF-1. *Novartis Found Symp* 272, 2-8; discussion 8-14, 33-16.

Shen, Q., Goderie, S.K., Jin, L., Karanth, N., Sun, Y., Abramova, N., Vincent, P., Pumiglia, K., and Temple, S. (2004). Endothelial cells stimulate self-renewal and expand neurogenesis of neural stem cells. *Science* 304, 1338-1340.

Shen, Q., Wang, Y., Kokovay, E., Lin, G., Chuang, S.-M., Goderie, S.K., Roysam, B., and Temple, S. (2008). Adult SVZ stem cells lie in a vascular niche: a quantitative analysis of niche cell-cell interactions. *Cell Stem Cell* 3, 289-300.

Shook, D., and Keller, R. (2003). Mechanisms, mechanics and function of epithelial-mesenchymal transitions in early development. *Mechanisms of development* 120, 1351-1383.

Simon, M.C., and Keith, B. (2008). The role of oxygen availability in embryonic development and stem cell function. *Nature reviews Molecular cell biology* 9, 285-296.

Singh, S., Howell, D., Trivedi, N., Kessler, K., Ong, T., Rosmaninho, P., Raposo, A.A., Robinson, G., Roussel, M.F., Castro, D.S., *et al.* (2016). Zeb1 controls neuron differentiation and germinal zone exit by a mesenchymal-epithelial-like transition. *Elife* 5.

Singh, S., and Solecki, D.J. (2015). Polarity transitions during neurogenesis and germinal zone exit in the developing central nervous system. *Front Cell Neurosci* 9, 62.

Solecki, D.J. (2012). Sticky situations: recent advances in control of cell adhesion during neuronal migration. *Curr Opin Neurobiol* 22, 791-798.

Studer, L., Csete, M., Lee, S.-H., Kabbani, N., Walikonis, J., Wold, B., and McKay, R. (2000). Enhanced Proliferation, Survival, and Dopaminergic Differentiation of CNS Precursors in Lowered Oxygen. *Journal of Neuroscience* 20, 7377-7383.

Syed, M.H., Mark, B., and Doe, C.Q. (2017). Playing Well with Others: Extrinsic Cues Regulate Neural Progenitor Temporal Identity to Generate Neuronal Diversity. *Trends Genet* 33, 933-942.

Tavazoie, M., Van der Veken, L., Silva-Vargas, V., Louissaint, M., Colonna, L., Zaidi, B., Garcia-Verdugo, J.M., and Doetsch, F. (2008). A specialized vascular niche for adult neural stem cells. *Cell Stem Cell* 3, 279-288.

Taverna, E., Gotz, M., and Huttner, W.B. (2014). The cell biology of neurogenesis: toward an understanding of the development and evolution of the neocortex. *Annu Rev Cell Dev Biol* 30, 465-502.

Uzquiano, A., Gladwyn-Ng, I., Nguyen, L., Reiner, O., Gotz, M., Matsuzaki, F., and Francis, F. (2018). Cortical progenitor biology: key features mediating proliferation versus differentiation. *J Neurochem*.

Yuen, T.J., Silbereis, J.C., Silbereis, J.C., Griveau, A., Griveau, A., Chang, S.M., Chang, S.M., Daneman, R., Daneman, R., *et al.* (2014). Oligodendrocyte-Encoded HIF Function Couples Postnatal Myelination and White Matter Angiogenesis. *Cell* 158, 383-396.

FIGURE LEGENDS

Figure 1. Cerebellar Hypoxia Accompanies GNP Proliferation and Abates with Development

(A) Immunohistochemical staining of P5 and P9 cerebella reveals strong pimonidazole (red) binding in all layers that abates by P15. (B) Complementary vascularization (GluT1, red) is sparse at P5 and P9 but covers wider areas at P15. Bar charts show quantification of the relative vascularization of the cerebellar layers at the investigated time-points. The percentage vascularization of the tissue, represented by **GluT1** staining increased significantly in the EGL, ML and IGL over time, when compared to P5 levels in the respective region (T-test, $P < 0.05$ in all timepoints tested against P5 levels). (C) Analysis of vascularization of the P7 cerebellum, hindbrain, and midbrain, using iDisco-cleared tissue. The left panel is a full 3D rendering of a representative cerebellum, hindbrain, and midbrain from an Atoh1-EGFP animal included in the quantitative analyses. The middle three panels are single-plane representative examples of the Atoh1-EGFP signal used to segment the EGL/ML throughout the 3D analyzed iDisco-cleared volumes (left), an example of a single-plane mask of segmented EGL/ML that was applied to iDisco-cleared volumes, and an example of a single-plane mask of segmented GluT1-labeled vasculature that was detected through the iDisco-cleared volumes. The right panel is a violin plot comparing the full 3D vascular volume fraction of the EGL/ML, hindbrain, and midbrain for three iDisco-cleared Atoh1-EGFP mice. The average vascular volume fraction of the EGL/ML region is roughly half that of the

IGL, hindbrain, and midbrain regions that contain differentiated neurons. (D) Immunohistochemical staining of P7 and P15 cerebella showing that Hif1 α (red) expression coincides with Ki67 expression (green) but is complementary to p27^{Kip1} expression (green). The Hif1 α signal abates by P15. The scale bar equals 25 μ m. (E) Western blots of cerebellar lysates reveal high Hif1 α and pimonidazole adduct levels between P2 and P9 that abate after P9, significantly, when compared to P7 levels (T-test, $P < 0.001$). Actin (green) was used for normalization. The bar diagrams at lower right depict the relative Hif1 α levels normalized to P7 and actin and the pimonidazole levels normalized to actin. Pimonidazole signal significantly reduced from P7 levels after P12 (T-test, $P < 0.05$). [T-test P value significance denoted by: * (< 0.05), ** (< 0.01), *** (< 0.001), **** (< 0.0001)].

Figure 2. Altering the Hif1 α Oxygen-Sensing Pathway *in Vivo* Tunes GNP Proliferation

(A) Western blots of *Atoh1-Cre:Hif1 $\alpha^{flx/flx}$* CGNs grown in culture in 2% O₂ show $75.6 \pm 5.8\%$ (mean \pm sem) reduction in Hif1 α signal (red [T-test, $P < 0.01$]) compared to *Hif1 $\alpha^{flx/flx}$* CGNs. Actin (green) served as a loading control. (B) Bar diagrams show cerebella of *Atoh1-Cre:Hif1 $\alpha^{flx/flx}$* mice to be smaller than those of controls throughout development (P7 *Hif1 $\alpha^{flx/flx}$* : 4.8 ± 0.2 mm², *Atoh1-Cre:Hif1 $\alpha^{flx/flx}$* : 4.1 ± 0.2 mm², T-test, $P < 0.01$; P10 *Hif1 $\alpha^{flx/flx}$* : 5.1 ± 0.1 mm², *Atoh1-Cre:Hif1 $\alpha^{flx/flx}$* : 4.6 ± 0.2 mm², T-test, $P < 0.05$; P15 *Hif1 $\alpha^{flx/flx}$* : 8.0 ± 0.1 mm², *Atoh1-Cre:Hif1 $\alpha^{flx/flx}$* : 7.3 ± 0.3 mm², T-test, $P < 0.07$). (C) Immunohistochemical examination using pH3 (cyan), EdU (green), and Ki67 (red) of GNP proliferation in P7 cerebella in *Atoh1-*

Cre:Hif1^{flx/flx} and *Atoh1-Cre:VHL^{flx/flx}* mice and the respective controls. (D) The number of pH3-positive (pH3⁺) GNPs is 23 ± 6% reduction in *Atoh1-Cre:Hif1^{flx/flx}* mice and a 39 ± 13% increase in *Atoh1-Cre:VHL^{flx/flx}* mice, as compared to the respective controls ($P < 0.05$ for both cases). The ratio of EdU⁺/Ki67⁻ cells is increased in *Atoh1-Cre:Hif1^{flx/flx}* mice (53 ± 15%) and reduced in *Atoh1-Cre:VHL^{flx/flx}* mice (30 ± 5%), as compared to the respective controls (T-test, $P < 0.02$ for *Atoh1-Cre:VHL^{flx/flx}*; and $P < 0.05$ for *Atoh1-Cre:VHL^{flx/flx}*). [T-Test P value significance denoted by: * (<0.05), ** (<0.01), *** (<0.001), **** (<0.0001)].

Figure 3. Oxygen Tension Tunes CGN GZ Exit and Migration ex Vivo

(A) P7 EGLs were electroporated with H2B-mCherry and maintained in culture at various O₂ concentrations. After 24 or 48 h in *ex vivo* culture, the distance of labeled CGNs from the pial surface (to the left in every image) was analyzed. The histograms above each representative image show the binned distance distribution for each condition (n > 1,300 [24 h] or > 2,000 [48 h] cells analyzed for each condition; a χ^2 test showed that at 24 h and 48 h, a 2% or 5% O₂ concentration significantly decreased migration ($P < 0.04$ compared to that observed in 20% O₂), and the box plot (far right) shows the average distances, which also demonstrated that, all hypoxic conditions (including 10 and 15% O₂ concentration shown in supplemental figure 2) Lowering O₂ levels significantly decreased migration compared to that observed in 20% O₂ ($P < 0.03$ for all conditions by T-test). Whereas, hypoxic conditions (2% or 5% O₂) decreased neuronal migration at 24

and 48 h timepoints, hyperoxic conditions (40% O₂) increased neuronal migration at the 48 h timepoint, by comparison with that observed in 20% O₂. (B) Analysis of *ex vivo* live-cell imaging of slices maintained in culture in 20% or 2% O₂. The left graph shows the percentage layer occupancy plot of slice cultures maintained in 20% or 2% O₂. The blue trace is the outer EGL, the orange trace is the inner EGL, the grey trace is the ML, and the yellow trace is the IGL. The middle plots are migration efficiency plots (i.e., showing the frequency of migration speeds for inward or tangential migration) for each layer, with the darker bars representing the inward migration efficiency in each layer and the lighter bars representing the tangential migration percentage in each layer. (C) CGN migration is independent of energy production from glycolysis or oxidative phosphorylation. Neither inhibiting glycolysis (galactose) nor inhibiting the TCA cycle and oxidative phosphorylation (malonate) decreases CGN migration (glucose: \bar{x} distance = $64.7 \pm 1.7 \mu\text{m}$; galactose: \bar{x} distance = $60.5 \pm 2.4 \mu\text{m}$, $P > 0.05$; malonate: \bar{x} distance = $61.6 \pm 4.0 \mu\text{m}$, $P > 0.05$). [T-test and χ^2 test; P value significance denoted by: * (<0.05), ** (<0.01), *** (<0.001), **** (<0.0001)].

Figure 4. Deletion of *Hif1 α* Restores Hypoxia-Induced GZ Exit Deficiency

(A) Electroporation of the EGL with a hydroxylation-deficient *Hif1 α* (*Hif1* HD) impairs CGN migration after 48 h in *ex vivo* culture ($41.7 \pm 3.6 \mu\text{m}$ [mean distance migrated \pm sem] as opposed to $58.2 \pm 4.0 \mu\text{m}$ in the LacZ controls [χ^2 test, $P < 0.0001$, T-test $P < 0.02$]). Deleting *Hif1 α* by expressing Cre recombinase in *Hif1 α ^{flx/flx}* cerebella led to precocious migration in 20% O₂ (Cre^{inactive}: \bar{x} distance =

$33.9 \pm 0.5 \mu\text{m}$, $\text{Cre}^{\text{active}}$: \bar{x} distance = $48.1 \pm 2.57 \mu\text{m}$, $P < 0.001$) and rescued the hypoxia-induced migration deficiency ($\text{Cre}^{\text{inactive}}$: \bar{x} distance = $25.3 \pm 1.3 \mu\text{m}$, $\text{Cre}^{\text{active}}$: \bar{x} distance = $43.5 \pm 3.7 \mu\text{m}$, χ^2 and T-test analysis both $P < 0.0002$). (B) Longitudinal time-lapse analysis of migration kinetics in $\text{Hif1}\alpha^{\text{flx/flx}}$ ($\text{Cre}^{\text{inactive}}$ transfected) or $\text{Hif1}\alpha^{\text{flx/flx}}$ ($\text{Cre}^{\text{active}}$ transfected) CGNs in *ex vivo* cerebellar slices. The leftmost graph shows the percentage layer occupancy plots for $\text{Hif1}\alpha^{\text{flx/flx}}$ CGNs and $\text{Hif1}\alpha^{-/-}$ CGNs. The blue trace is the outer EGL, the orange trace is the inner EGL, the grey trace is the ML, and the yellow trace is the IGL. The middle plots are migration efficiency plots (i.e., showing the frequency of migration speeds for inward or tangential migration) for each layer, with the darker bars representing the inward migration efficiency in each layer and the lighter bars representing the tangential migration percentage in each layer. (C) Deleting VHL by expressing Cre recombinase in $\text{VHL}^{\text{flx/flx}}$ cerebella reduced CGN migration by comparison to that seen with a catalytically inactive Cre recombinase ($\text{Cre}^{\text{inactive}}$) ($\text{Cre}^{\text{inactive}}$: \bar{x} distance = $117.6 \pm 0.4 \mu\text{m}$, $\text{Cre}^{\text{active}}$: \bar{x} distance = $80.5 \pm 3.8 \mu\text{m}$, $P < 0.0001$ [χ^2 test] or $P < 0.001$ [T-test]). Migration could be restored by co-electroporation of VHL ($\text{Cre}^{\text{active}}$ + VHL \bar{x} distance = $105.7 \pm 4.7 \mu\text{m}$; $P < 0.0001$ [χ^2 test] or $P < 0.004$ [T-test] vs $\text{Cre}^{\text{active}}$). (D) Longitudinal time-lapse analysis of migration kinetics in $\text{VHL}^{\text{flx/flx}}$ ($\text{Cre}^{\text{inactive}}$ transfected) or $\text{VHL}^{\text{flx/flx}}$ ($\text{Cre}^{\text{active}}$ transfected) CGNs in *ex vivo* cerebellar slices. The leftmost graph shows the percentage layer occupancy plots for VHL^{wt} CGNs and $\text{VHL}^{-/-}$ CGNs. The blue trace is the outer EGL, the orange trace is the inner EGL, the grey trace is the ML, and the yellow trace is the IGL. The middle plots are migration efficiency plots (i.e., showing the frequency of

migration speeds for inward or tangential migration) for each layer, with the darker bars representing the inward migration efficiency in each layer and the lighter bars representing the tangential migration percentage in each layer. [T-test and X^2 test; P value significance denoted by: * (<0.05), ** (<0.01), *** (<0.001), **** (<0.0001)].

Figure 5. Zeb1 is Activated by Hif1 α

(A) Immunohistochemical staining of *ex vivo* cerebellar slices maintained in culture in 2% O₂ for 48 h shows increased Zeb1 staining (green) in the EGL. (B) Quantitative real-time PCR of granule cells overexpressing Hif1 α HD shows upregulation of Hif1 α and established Hif1 α downstream targets. Whereas Zeb1 is robustly upregulated by Hif1 α gain of function, known Zeb1 downstream targets, such as the polarity-complex proteins Pard3 and Pard6 α and the cell adhesion molecule Chl1, are repressed. (C) Visual representation of Hif1 α ChIP-seq enrichment in the vicinity of the Zeb1 locus. Peak finding was run on 35.1 million input tags pooled from three Atoh1-EGFP sorted biological replicates and each peak has a MACS2 p-value < 1×10^{-12} . Exons are represented as blue rectangles and the direction of transcription of a locus is represented by hatched arrows along intronic sequence. Hif1 α peaks at -212 and +847 relative to the Zeb1 TSS harbor conserved HRE binding sites. (D) ChIP PCR validation of Hif1 α binding to -212 and +847. The graph shows relative binding measured in binding events per 1000 cells to a control locus, two previously validated Hif1 α binding sites (Pgk and Ldha), and Zeb1 -212 and +847. (E) Heat map of microarrays of CGNs electroporated with LacZ (control), Zeb1, or Hif1 α . Marked with a red box are a

small subset of transcripts that are repressed by Zeb1 and Hif1 α (magnified at right). Differentially expressed genes were selected using FDR corrected p-value (q value) of 0.05 and fold change of 1.5 as the cutoff. (F) Cluster analysis using gene ontology terms and DAVID algorithms showing the highest fold enrichment for nine proteins already known to be involved in neuronal migration. (G) Model for the genetic interactions between Hif1 α , Zeb1 and the Pard proteins in hypoxia or normoxia

Figure 6. Zeb1 Loss of Function or Pard Complex Gain of Function Rescues Hypoxia and Hif1 α -Pathway Inhibition of GZ Exit.

(A) Silencing Zeb1 with *Zeb1* shRNA rescues the hypoxia-mediated migration deficiency (shControl at 20% O₂: \bar{x} distance = 84.4 \pm 2.2 μ m; shControl at 2% O₂: \bar{x} distance = 32.1 \pm 2.8 μ m; shZeb1 at 2% O₂: \bar{x} distance = 49.1 \pm 1.7 μ m; T-test and X² analysis: $P < 0.001$), Hif1 α HD over-expression (LacZ + Mir30 Luc688 sh (Control sh): \bar{x} distance = 70.3 \pm 3.8 μ m; Hif1 α HD OE + Mir30 Luc688 sh: \bar{x} distance = 42.2 \pm 4.0 μ m; Hif1 α HD OE + shZeb1: \bar{x} distance = 70.0 \pm 4.6 μ m; T-test and X² analysis: $P < 0.01$) or VHL deletion (*VHL*^{flx/flx} Cre^{inactive} + Mir30 Luc688 sh: \bar{x} distance = 96.4 \pm 9.0 μ m; *VHL*^{flx/flx} Cre^{active} + Mir30 Luc688 sh: \bar{x} distance = 62.3 \pm 6.4 μ m; *VHL*^{flx/flx} Cre^{active} + shZeb1: \bar{x} distance = 79.3 \pm 2.7 μ m; X² analysis: $P < 0.02$). Electroporation of the EGL with Zeb1 inhibits precocious migration mediated by *Hif1 α* deletion (*Hif1 α* ^{flx/flx} Cre^{inactive} + LacZ: \bar{x} distance = 54.5 \pm 3.0 μ m; *Hif1 α* ^{flx/flx} Cre^{inactive} + Zeb1: \bar{x} distance = 44.9 \pm 2.3 μ m (T-test; $P < 0.03$); *Hif1 α* ^{flx/flx} Cre^{active} + LacZ: \bar{x} distance = 59.3 \pm 2.9 μ m; *Hif1 α* ^{flx/flx} Cre^{active} + Zeb1: \bar{x} distance =

41.2 ± 1.4 μm; T-Test: $P < 0.001$, X^2 analysis; $P < 0.03$). (B) Silencing *Pard3* or *Pard6α* in 2% O₂ completely abolished the rescue of the hypoxia-mediated migration deficiency through the deletion of *Hif1α* (*Hif1α^{flx/flx} Cre^{inactive}* + shControl: \bar{x} distance = 31.8 ± 2.5 μm; *Hif1α^{flx/flx} Cre^{active}* + shControl: \bar{x} distance = 50.4 ± 2.8 μm; *Hif1α^{flx/flx} Cre^{active}* + sh*Pard3*: \bar{x} distance = 30.5 ± 1.6 μm, T-test and X^2 analysis: $P < 0.001$; *Hif1α^{flx/flx} Cre^{active}* + sh*Pard6α*: \bar{x} distance = 36.2 ± 3.2 μm, T-test and X^2 analysis: $P < 0.01$). *Pard3*, *Pard6α*, or *Chl1* gain of function rescued the hypoxia-mediated migration deficiency (*LacZ*: \bar{x} distance = 42.6 ± 1.8 μm; *Pard3*: \bar{x} distance = 54.1 ± 3.0 μm, T-test and X^2 analysis $P < 0.05$; *Pard6α*: \bar{x} distance = 54.7 ± 3.7 μm, T-test and X^2 analysis $P < 0.01$; *Chl1*: \bar{x} distance = 54.9 ± 4.4 μm, T-test and X^2 analysis $P < 0.05$) *Pard6α* and *Pard3* overexpression rescued the phenotype observed by deletion of the *VHL* pathway (*VHL^{flx/flx} Cre^{inactive}* + *LacZ*: \bar{x} distance = 96.4 ± 8.7 μm; *VHL^{flx/flx} Cre^{active}* + *LacZ*: \bar{x} distance = 59.4 ± 1.8 μm; T-test and X^2 analysis: $P < 0.01$; *VHL^{flx/flx} Cre^{active}* + *Pard3*: \bar{x} distance = 108.5 ± 4.3 μm; T-test and X^2 analysis: $P > 0.3$; *VHL^{flx/flx} Cre^{active}* + *Pard6α*: \bar{x} distance = 95.7 ± 6.3 μm; T-test and X^2 analysis: $P > 0.9$)

Figure 7. The Antagonistic Relation Between *Hif1α*-Zeb1 and *Pard6α* Regulates *Itgβ1*-Mediated GZ Occupancy. (A) CGNs in culture were nucleofected with a plasmid encoding H2B mCherry alone or in combination with plasmids encoding Myc-Zeb1 plus single plasmids encoding *Pard6α*. After 24 h in culture, nucleofected cells were FACS sorted to isolate mRNA (n = 3 sort experiments). qRT-PCR analyses show that Zeb1 gain-of-function induces *Itgβ1*

mRNA expression (5.5 ± 2.4 fold increase vs controls [$\bar{x} \pm sd$]) and that restored *Pard6a* expression reduces *Itg β 1* expression 6.8 ± 1.1 fold decrease vs controls (T-test, $P < 0.02$). (B) Immunohistochemical staining of P7 cerebella shows that activated *Itg β 1* expression (red) in GNPs of the outer EGL is coincident with both *Zeb1* (left panel, green) and phospho-FAK Y397 (middle panel, green). Developmental qRT-PCR analysis of purified GNP RNA shows that mRNA expression is high in the early postnatal period but subsequently declines below P0 expression levels, when *Itg β 1* CGN commences. (C) Low O₂ tension increases CGN adherence to laminin, a pial-derived ECM component. CGNs were purified from P7 cerebella, plated on laminin-coated glass coverslips, incubated at the indicated oxygen tensions, agitated to dislodge nonadherent cells, stained with DAPI, and then microscopically analyzed to determine the levels of adherent cells ($n = 3$ for graphed data). Cultures incubated at 2% O₂ levels were significantly more dense than their 20% O₂ counterparts (117.1 ± 21.1 cells/mm² [average \pm sem] at 20% O₂ and 179.0 ± 27.2 cells/mm² at 2% O₂, T-test, $P < 0.0005$) (D) P7 cerebellar immunohistochemistry in shows that activated *Itg β 1* engagement visualized with FAK-P-Y397 staining (red) is enhanced in GNPs from *Atoh1-Cre:VHL^{flx/flx}* cerebella. (E) *Itg β 1* deletion rescues hypoxia-mediated migration deficiency (*Cre^{inactive}*: \bar{x} distance = 40.5 ± 2.3 μ m, *Cre^{active}*: \bar{x} distance = 73.7 ± 4.4 μ m, $P < 0.005$ and 0.0001 [by *t*-test and χ^2 test respectively]). (F) EGL electroporation of an *Itg β 1* G737V expression vector impairs CGN migration after 48 h in *ex vivo* culture (*LacZ*: \bar{x} distance = 64.4 ± 0.2 μ m, *Itg β 1*: \bar{x} distance = 35.4 ± 6.0 μ m, $P < 0.01$ [by *t*-test and χ^2 test]). (G) LLS-SIM reveals that *Hif1 α* and *Zeb1* stimulate

CGN integrin adhesion to a laminin substrate, whereas Pard6 α rescue restores integrin adhesion to baseline levels. CGNs were purified from P7 cerebella, electroporated with a LASP1-Emerald expression vector plus the indicated expression constructs, plated on laminin-coated glass coverslips, and then examined microscopically via LLS-SIM to determine the levels of integrin-based focal adhesions (e.g., LASP1 punta seen in the Zeb1 GOF image). The violin plot compares focal adhesions detected by Weka machine learning (n > 20 cells per condition).

Supplemental Figure 1: Immunohistochemical staining of P7 cerebella of *Atoh1-Cre:VHL^{flx/wt}* (control) and *Atoh1-Cre:VHL^{flx/flx}* mice with an antibody against a cleaved caspase 3 epitope (red) and DAPI staining (blue) shows that there is a marginal increase in cleaved caspase 3 staining in *Atoh1-Cre:VHL^{flx/flx}* samples compared to controls.

Supplemental Figure 2: Distribution graphs of slices incubated at 10% and 15% O₂ not included in Figure 3 (n>2000 in all conditions shown). Compared to 20% O₂ both 10% and 15% O₂ demonstrated reduced migration of CGNs at both 24 and 48 hour time points. Unlike average distance plots in Figure 3A hypoxic conditions show in Figure 3 only 15% O₂ incubation for 24 hours was significant different via X² test, P<0.001.

Supplemental Figure 3. The role of EGLN1 and 3 in hypoxia

(A) and (B) Electroporation of the EGL with the prolyl hydroxylase (PHD) enzyme Egl nine homolog 1 or 3 (EGLN1 or EGLN3) spurred CGN migration after 48 h *ex vivo* culture in hypoxic conditions (2% O₂) or normoxic conditions (20% O₂). Electroporating cerebella from wild-type mice with EGLN1 resulted in a slight increase in the migration of CGNs in 2% O₂, which was not evident when cells were electroporated with a hydroxyl-deficient mutant in EGLN1 (EGLN1HD control: \bar{x} distance = 87.6 ± 3.7 μm, EGLN1: \bar{x} distance = 129.5 ± 4.3 μm [*P* < 0.6 (χ² test) and *P* < 0.02 (*t*-test) for EGLN1 vs control], EGLN1HD: \bar{x} distance = 69.4 ± 8.9 μm [*P* < 0.6 (χ² test) and *P* < 0.5 (*t*-test) for EGLN1HD vs control]). The

effects of EGLN1 were more evident in 20% O₂, with EGLN1 spurring migration after 48 h (control: \bar{x} distance = 116.3 ± 13.6 μm, EGLN1: \bar{x} distance = 181.2 ± 16.8 μm [$P < 0.002$ (χ^2 test) and $P < 0.02$ (t -test) for EGLN1 vs control], EGLN1HD: \bar{x} distance = 124.3 ± 16.9 μm [$P < 1.0$ (χ^2 test) and $P < 0.3$ (t -test) for EGLN1HD vs control]). Similar results were obtained with EGLN3 and EGLN3HD after 48 h *ex vivo* culture in 2% O₂ (control: \bar{x} distance = 77.1 ± 6.4 μm, EGLN3: \bar{x} distance = 125.7 ± 9.2 μm [$P < 0.01$ (χ^2 test) and $P < 0.005$ (t -test) for EGLN3 vs control], EGLN3HD: \bar{x} distance = 72.3 ± 4.4 μm [$P < 1.0$ (χ^2 test) and $P < 0.3$ (t -test) for EGLN3HD vs Control) or 20% O₂ (control: \bar{x} distance = 95.4 ± 5.0 μm, EGLN3: \bar{x} distance = 153.6 ± 14.0 μm [$P < 0.002$ (χ^2 test) and $P < 0.02$ (t -test) for EGLN3 vs control], EGLN3HD: \bar{x} distance = 84.5 ± 3.9 μm [$P < 1.0$ (χ^2 test) and $P < 0.1$ (t -test) for EGLN3HD vs control]). (C) Deleting EGLN1 by expressing Cre recombinase in *EGLN1^{flx/flx}* cerebella led to reduced migration in 20% O₂, mimicking hypoxic conditions (Cre^{inactive}: \bar{x} distance = 94.5 ± 4.0 μm, Cre^{active}: \bar{x} distance = 68.5 ± 3.0 μm, [$P < 0.002$ (χ^2 test) and $P < 0.002$ (t -test) for Cre^{active} vs Cre^{inactive}]) the EGLN1 loss of function–induced migration deficiency was rescued in epistasis experiments by Pard3 overexpression (Cre^{active} + Pard3: \bar{x} distance = 93.0 ± 3.8 μm [$P = 1.0$ (χ^2 test) and $P < 0.8$ by (t -test) for Cre^{active} + Pard3 vs Cre^{inactive}]), Pard6α overexpression (Cre^{active} + Par 6: \bar{x} distance = 92.7 ± 5.8 μm, [$P = 1.0$ (χ^2 test) and $P < 0.8$ (t -test) for Cre^{active} + Pard6α vs Cre^{inactive}]), Chl1 overexpression (Cre^{active} + Chl: \bar{x} distance = 100.5 ± 3.4 μm, [$P = 1.0$ (χ^2 test) and $P < 0.3$ (t -test) for Cre^{active} + Chl vs Cre^{inactive}]), and by overexpressing EGLN1 itself (Cre^{active} + EGLN1: \bar{x} distance = 95.8 ± 2.4 μm, [$P < 1.0$ (χ^2 test) and $P < 0.5$ (t -test) for Cre^{active} + EGLN1

vs Cre^{inactive}). The reduction in CGN migration due to the overexpression of Cre^{active} in these mice was also rescued by overexpression of shRNA to Zeb1 (Cre^{active} + Zeb 1 shRNA: \bar{x} distance = $72.6 \pm 3.2 \mu\text{m}$), as compared to scrambled shRNA overexpression (Cre^{active} + scramble shRNA: \bar{x} distance = $54.0 \pm 5.0 \mu\text{m}$ [$P < 1.0$ (χ^2 test) and $P < 0.05$ by (t -test) for Cre^{active} + Zeb1 shRNA vs Cre^{active} + scrambled shRNA]).

Supplemental Figure 4: (A) VHL and Hif1 α have an antagonistic relationship. Removal of VHL expression by the expression of Cre^{active} in *VHL*^{flx/flx} mice reduced average distances from the pial surface (\pm sem) from 76.8 ± 2.3 (Cre^{inactive}) to 56.7 ± 0.1 (*Vhl*^{flx/flx} + Cre^{active}). T-test ($P < 0.05$) and X^2 analysis ($P < 0.0005$) both showed that this was a significant change. However in double floxed mice (*Vhl*^{flx/flx}; *Hif1 α* ^{flx/flx}) the expression of Cre^{active} resulted in an average cell migration of $90.9 \pm 5.5 \mu\text{m}$. (B) Reduction of the Ptch pathway did not affect the VHL deletion phenotype. Control slices demonstrated an average migration of $79.1 \pm 3.4 \mu\text{m}$ after 48 hours at 20% O₂ (*Vhl*^{flx/flx} + Cre^{inactive}). Deletion of VHL (*VHL*^{flx/flx} + Cre^{active}) reduced the average migration significantly to $55.9 \pm 1.8 \mu\text{m}$ (T-test: $P < 0.01$, X^2 analysis: $P < 0.0001$). Deletion of both VHL and Ptch *VHL*^{flx/flx}; *Ptch*^{flx/flx} + Cre^{active}) resulted in an average migration of $56.8 \pm 1.2 \mu\text{m}$, which was not significantly different to *Vhl*^{flx/flx} + Cre^{active} (T-test, $P < 0.37$). (C) Use of the Gli agonist, GANT61 did not restore GZ exit. Control slices incubated at 20% O₂ for 48 hours had an average distance from pial surface of $105.2 \pm 4.3 \mu\text{m}$, whereas slices incubated at 2% O₂ only migrated on average $63.0 \pm 3.7 \mu\text{m}$ (T-test; $P < 0.02$, X^2 analysis:

P<0.0001) Addition of GANT61 further reduced average migration to $42.3 \pm 5.0 \mu\text{m}$ (T-test: P<0.01, X² analysis: P<0.0001).

Supplemental Figure 5. Heat map of the transcriptomes of CGNs freshly purified from P0 and P15 cerebella compared to those of CGNs maintained in culture for 48 h in 2% or 20% O₂. Culture in 2% O₂ restrains the expression of genes that are heavily expressed in mature CGNs purified from P15 cerebella or in CGNs allowed to fully differentiate after 48 h in culture in 20% O₂. Differentially expressed genes were selected using FDR corrected p-value (q value) of 0.05 and fold change of 1.5 as the cutoff.

Supplemental Figure 6. Immunohistochemical staining of P7 and P15 cerebella of VHL^{+/-} (control) and VHL^{-/-} (conditional deletion via *Atoh1-Cre*) mice shows that there are more NeuN-negative or Zeb1-positive GNPs in the P7 EGL of mutant animals. Moreover, Pard3 and Pard6 α expression is diminished in P7 cerebella when the Hif1 α pathway is activated in the CGN lineage via *Atoh1-Cre*. Finally, Zeb1 expression persists in the P15 cerebella in VHL-deficient CGNs, both in the GNPs in the remnants of the EGL and in subpopulations of CGNs in the IGL.

Supplemental Figure 7: Additional statistical analysis and average distance data from Figure 6. Average migration graphs for Zeb1 epistasis shown in Figure 6. (A) Average distance from pial surface of slices electroporated with Zeb1 shRNA (shZeb1) and incubated at 2% O₂ for 48hrs ($49.1 \pm 2.2 \mu\text{m}$ [\bar{x} distance \pm sem]) was

able to significantly increase migration compared to control shRNA (shCon) in similar conditions ($32.1 \pm 2.8 \mu\text{m}$, T-test, $P < 0.0001$). (B) Mimicking hypoxia by overexpressing Hif1 α was also significantly rescued by shZeb1. Control slices expressing LacZ and shCon demonstrated an average distance from pial surface of $70.3 \pm 3.8 \mu\text{m}$ after 48 hrs incubation at 20% O₂, Hif1 α HD OE with shCon reduced CGN migration significantly (T-test $P < 0.01$) to $42.2 \pm 4.1 \mu\text{m}$. However, when Hif1 α was co-expressed with shZeb1 the distance from pial surface increased ($70.3 \pm 4.6 \mu\text{m}$). (C) Conversely, reduction of Zeb1 expression in slices from *Vhl^{flx/flx}* mice was shown to partially rescue the phenotype of shown in these mice when Cre^{active} was co-expressed (*VHL^{flx/flx}* + Cre^{inactive} + shCon = $96.4 \pm 8.7 \mu\text{m}$, *VHL^{flx/flx}* + Cre^{active} + shCon \bar{x} distance = $62.3 \pm 6.4 \mu\text{m}$ [T-test, $P < 0.02$], *VHL^{flx/flx}* + Cre^{active} + shZeb1 \bar{x} distance = $79.2 \pm 2.7 \mu\text{m}$, T-test vs Cre^{inactive} + shCon $P < 0.22$). (D) Slices in which the Hif1 α pathway had been genetically deleted or not by Cre^{active} or Cre^{inactive} respectively, both demonstrated enhanced GZ occupancy when Zeb1 was overexpressed. Following 48 hrs incubation at 20% O₂ control slices (Cre^{inactive} + LacZ), CGNs were located $54.5 \pm 3.0 \mu\text{m}$ from the pial surface, but addition of Zeb1 reduced this to $44.9 \pm 2.3 \mu\text{m}$ (T-test $P < 0.05$). Similarly when co expressing Cre^{active}, control slices (LacZ) \bar{x} distance was $59.3 \pm 2.9 \mu\text{m}$, with Zeb1 it was $41.2 \pm 1.4 \mu\text{m}$ (T-test $P < 0.0001$). E and F) *Ex vivo* control slices from wild type C57Bl6 mice were electroporated to overexpress Hif1 α and LacZ (Hif1 α HD) had an \bar{x} distance from pial surface of $50.5 \pm 2.2 \mu\text{m}$ after 48hrs in 20% O₂. The effect of Hif1 α overexpression was overcome by co expressing either Pard3 (av, migration = $65.8 \pm 3.8 \mu\text{m}$, T-test, $p < 0.02$), Pard6 α (av, migration =

68.6 ± 1.2 μm, T-test, p< 0.00001) and Chl1 (av, migration = 67.3 ± 2.8 μm, T-test, p< 0.002, .n>3500 in each condition). (G) The effect of genetically deleting the Hif1α pathway were rescued by reducing Pard3 and Pard6α with shRNA constructs. Control slices treated with Cre^{inactive} and shCon and incubated for 24hrs at 2% O₂ resulted in \bar{x} distance from the pial surface of 31.8 ± 2.5 μm. Slices treated with Cre^{active} and shCon RNA migrated further on average, 50.4 ± 2.8 μm (T-test P<0.0005). Reducing Pard3 expression (with shPard3) in these slices rescued the phenotype (30.5 ± 1.6 μm, T-test P=1.0) as did Pard6α reduction (with shPard6α, 36.2 ± 3.2 μm, T-test >0.25). (H) The effects of hypoxia were also rescued by Pard3, Pard6α and also Chl1 too. Slices incubated at 2%O₂ for 24 hours had an \bar{x} distance from the pial surface of 42.6 ± 1.8 μm, addition of Pard3 (54.1 ± 3.0, T-test P<0.01), Pard6α (54.7 ± 3.7 μm, P<0.01) and Chl1 (54.9 ± 4.4, P<0.02) all increased migration distances significantly. (I) Pard3 and Pard6α also rescued the phenotype exhibited by the *VHL*^{flx/flx} slices. After 48hr incubation at 20% with expression of Cre^{inactive} we observed 96.4 ± 8.8 μm \bar{x} distance from the pial surface. This was reduced to 59.4 ± 1.8 μm (T-test, P<0.02). Expression with Pard3 (108.5 ± 4.3 μm, P>0.39) or Pard6α (95.7 ± 6.3 μm, P>0.96) both rescued this phenotype caused by loss of VHL.

Supplemental Figure 8: (A) Diagram to show the structure of mouse Pard6α protein and its interaction partners at different domains (above). Several mutant constructs were produced (below) to do a structure function assay to determine which domains were necessary or sufficient for its ability to modulate CGN

migration in cerebellar slices at 2% O₂ after 48 hrs incubation. (B) Structure function analysis showed that deletion of three regions resulted in an inability for Pard6α to rescue the effects of the hypoxic conditions. CGNs in control slices migrated 35.4 ± 1.9 μm from the pial surface (\bar{x} distance ± sem), whereas wild type Pard6α caused precocious migration in comparison (63.8 ± 2.4 μm, T-test P<0.00001; X² analysis P<0.00001). The mutant constructs T7A,S11A, and ΔCRIB gave very similar results to wild type Pard6α (63.9 ± 1.7 and 62.9 ± 3.2 μm respectively). Although the \bar{x} distance from the pia for the K19A mutant was significantly different from controls (45.6 ± 1.1 μm, T-test P<0.002), the distribution of cells was not significantly different to controls as judged by X² analysis at the 5% level (P<0.08). The distribution of CGNs with the M235W mutant was significantly different (X² analysis P<0.01), but \bar{x} distance of cells from the pial surface was similar to controls (36.9 ± 2.2 μm, T-test P<0.32). The ΔNLS and ΔFLS failed to rescue the Pard6α phenotype (38.5 ± 2.3 and 37.3 ± 2.2 μm respectively).

(C) Overexpression of a clustering mutant of Itgβ1 (V737N) resulted in a reduction of GZ exit after 48 hour incubation at 20% O₂. Controls migrated 89.2 ± 2.8 μm, whereas addition of ITGβ1 V737N resulted in the \bar{x} to drop to 62.7 ± 3.3 μm (T-test P<0.01, X² analysis P<0.001). However addition of wild type Pard6α rescued the control phenotype (if not caused an increase in migration instead), with CGNs migrating an \bar{x} distance of 100.8 ± 3.4 μm from the pial surface (T-test P<0.005 [although with increased migration, hence, red asterisk], X² analysis P<0.36).

Supplemental Figure 9. Molecular characterization of hypoxic response in GNP cultured in presence of Hif1 α inhibitor echinomycin related to Figure 7

(A) Sagittal section through the cerebellum of a P7 Atoh1-EGFP mouse, showing the expression of EGFP restricted to the outer External Granule Layer (oEGL). (iEGL internal Granule Layer, ML molecular layer, IGL Internal Granule Layer, Scale bar 50 μ m). (B) FACS plot of dissociated cells from P7 Atoh1-EGFP mice showing cell density according to their GFP intensity and the forward scatter area (FSC-A). Two main populations, High and Low, were sorted based on their fluorescent intensity and put back in culture (inserts). (Scale bar 10 μ m). (C) Atoh1-EGFP High cells were plated and cultured for 24h at 2% O₂, with or without echinomycin at 11.6pM. In presence of the Hif1 α inhibitor a reduction of GFP positive cells is observed. Loss of Atoh1 is an indicator of differentiation from GNPs to CGNs. (D) Quantification of the percentage of GFP positive cells after 24h of culture at 2% O₂ with increasing concentration of Echinomycin showing a dose dependent effect of the treatment. Data represented as mean \pm SEM. (n=2) (E) Western Blot analysis of protein extract from Atoh1-EGFP positive cells cultured 24h at 2% O₂ with DMSO or 1nM of Echinomycin. Gels represent Bnip3, Zeb1, GFP, Ina, Pard6 α , Itg α 6, Fak, phospho-FAK Y397, Hsc70 and total protein staining. Molecular weight in kDa is given for each protein as reference. (F) Quantification of WB protein level. The level are normalized to total protein staining and express relative to DMSO in replicate. Data represented as mean \pm SEM and p values below 0.05 are display on the graph (* p<0.05, ** p<0.001, *** p<0.005) (n \geq 3; two-tailed Student's unpaired *t* test against DMSO).

Supplemental Figure 10. Model of VHL-Hif1 α -Zeb1 regulation of Pard6 α control of GZ occupancy.

Supplemental Movies

Supplemental Movie 1

3D render and animated tour of an iDisco cleared P7 cerebellum from an *Atoh1*^{EGFP/EGFP} knockin animal stained with antibodies against EGFP (magenta) and Glut1 (cyan). Note: cyan label micro-blood vessels are generally located in progenitor free zones of the developing cerebellum. Rendering and animation were generated as a volume view in arivisAG Vision4D software.

Supplemental Movie 2

Representative time-lapse sequence of CGNs labeled with H2B-mCherry (nucleus, red) and GPI-pHluorin (external face of plasma membrane, green, green) migrating in an ex vivo cerebellar slice preparation incubated at 20% O₂. Time lapse encompasses roughly twelve hours of imaging time.

Supplemental Movie 3

Representative time-lapse sequence of CGNs labeled with H2B-mCherry (nucleus, red) and GPI-pHluorin (external face of plasma membrane, green,

green) migrating in an *ex vivo* cerebellar slice preparation incubated at 2% O₂. Low oxygen tension blocks the transition of CGNs to the ML and IGL. Time lapse encompasses roughly twelve hours of imaging time.

Supplemental Movie 4

Representative time-lapse sequence of Hif1 α ^{flx/flx} CGNs expressing Cre^{inactive} labeled with H2B-mCherry (nucleus, red) and GPI-pHluorin (external face of plasma membrane, green) migrating in an *ex vivo* cerebellar slice preparation incubated at 20% O₂. Time lapse encompasses roughly twelve hours of imaging time.

Supplemental Movie 5

Representative time-lapse sequence of Hif1 α ^{flx/flx} CGNs expressing Cre^{active} labeled with H2B-mCherry (nucleus, red) and GPI-pHluorin (external face of plasma membrane, green) migrating in an *ex vivo* cerebellar slice preparation incubated at 20% O₂. Hif1 α deletion leads to early population of the ML and IGL of the cerebellar slice compared to Cre^{inactive} expressing cells. Time lapse encompasses roughly twelve hours of imaging time.

Supplemental Movie 6

Representative time-lapse sequence of *VHL*^{flx/flx} CGNs expressing Cre^{inactive} labeled with H2B-mCherry (nucleus, red) and GPI-pHluorin (external face of

plasma membrane, green) migrating in an *ex vivo* cerebellar slice preparation incubated at 20% O₂. Time lapse encompasses roughly twelve hours of imaging time.

Supplemental Movie 7

Representative time-lapse sequence of *VHL^{fix/fix}* CGNs expressing Cre^{active} labeled with H2B-mCherry (nucleus, red) and GPI-pHluorin (external face of plasma membrane, green) migrating in an *ex vivo* cerebellar slice preparation incubated at 20% O₂. VHL deletion leads to retention of GNP or CGNs in the outer layer of the cerebellar slice compared to Cre^{inactive} expressing cells. Time lapse encompasses roughly twelve hours of imaging time.

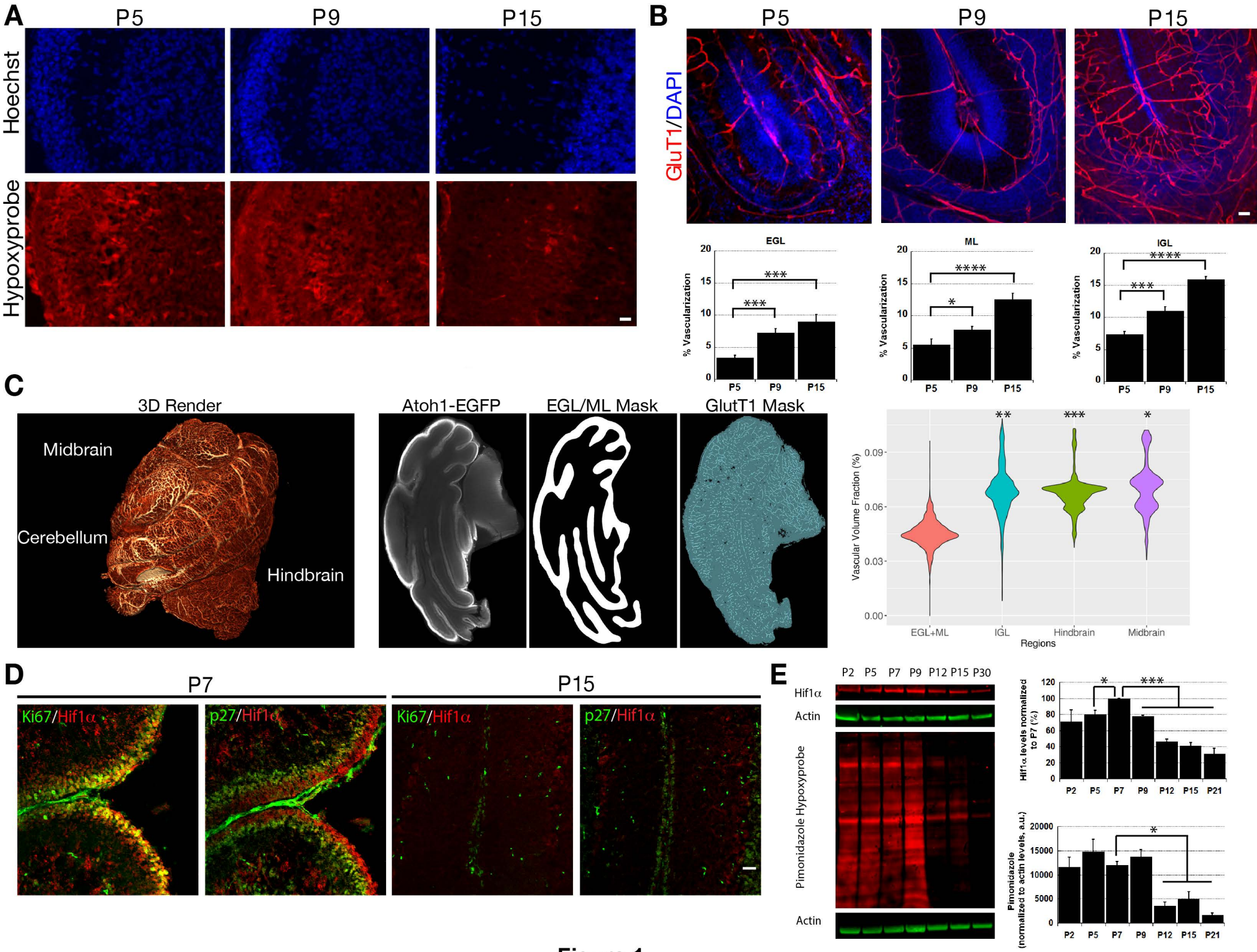


Figure 1

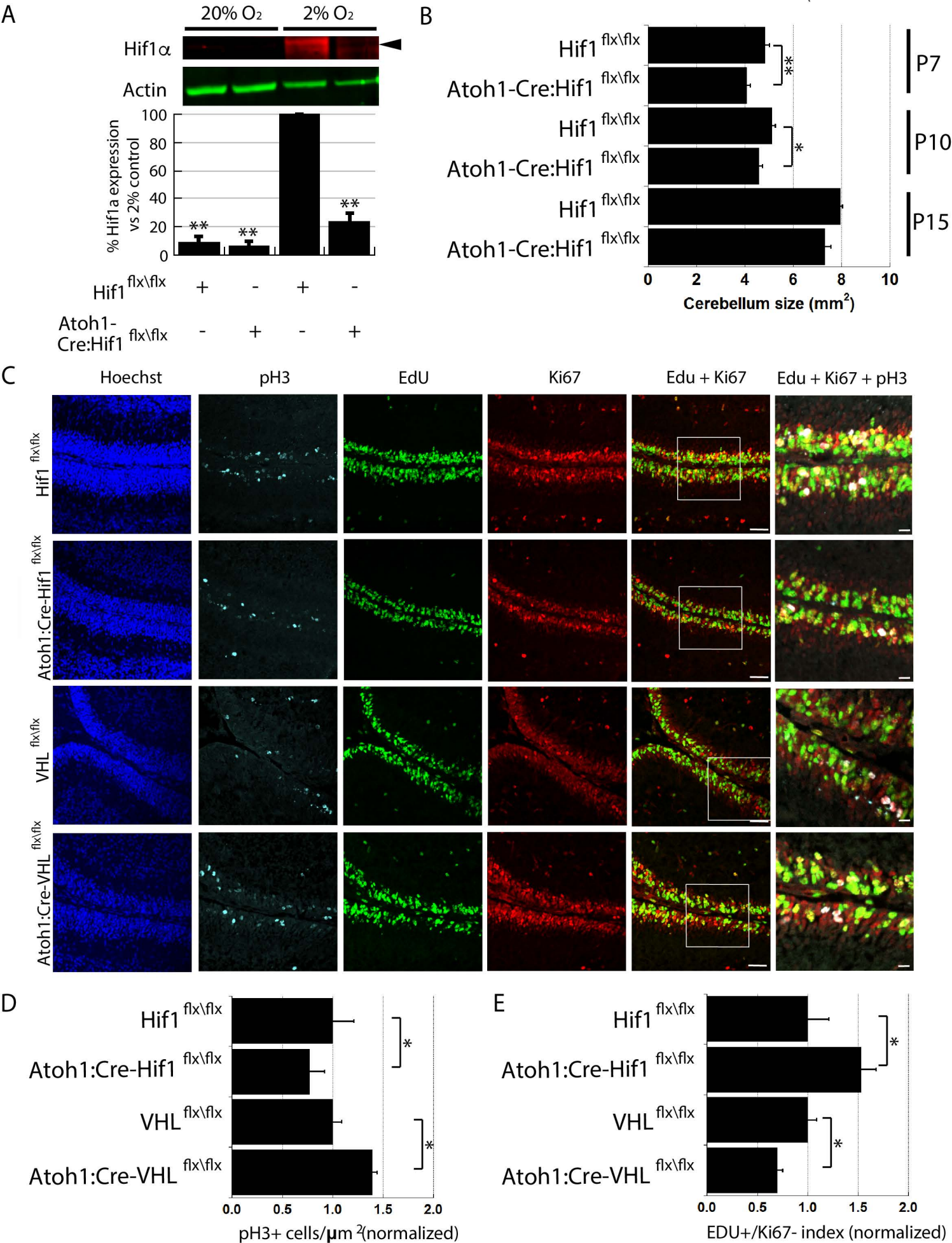


Figure 2

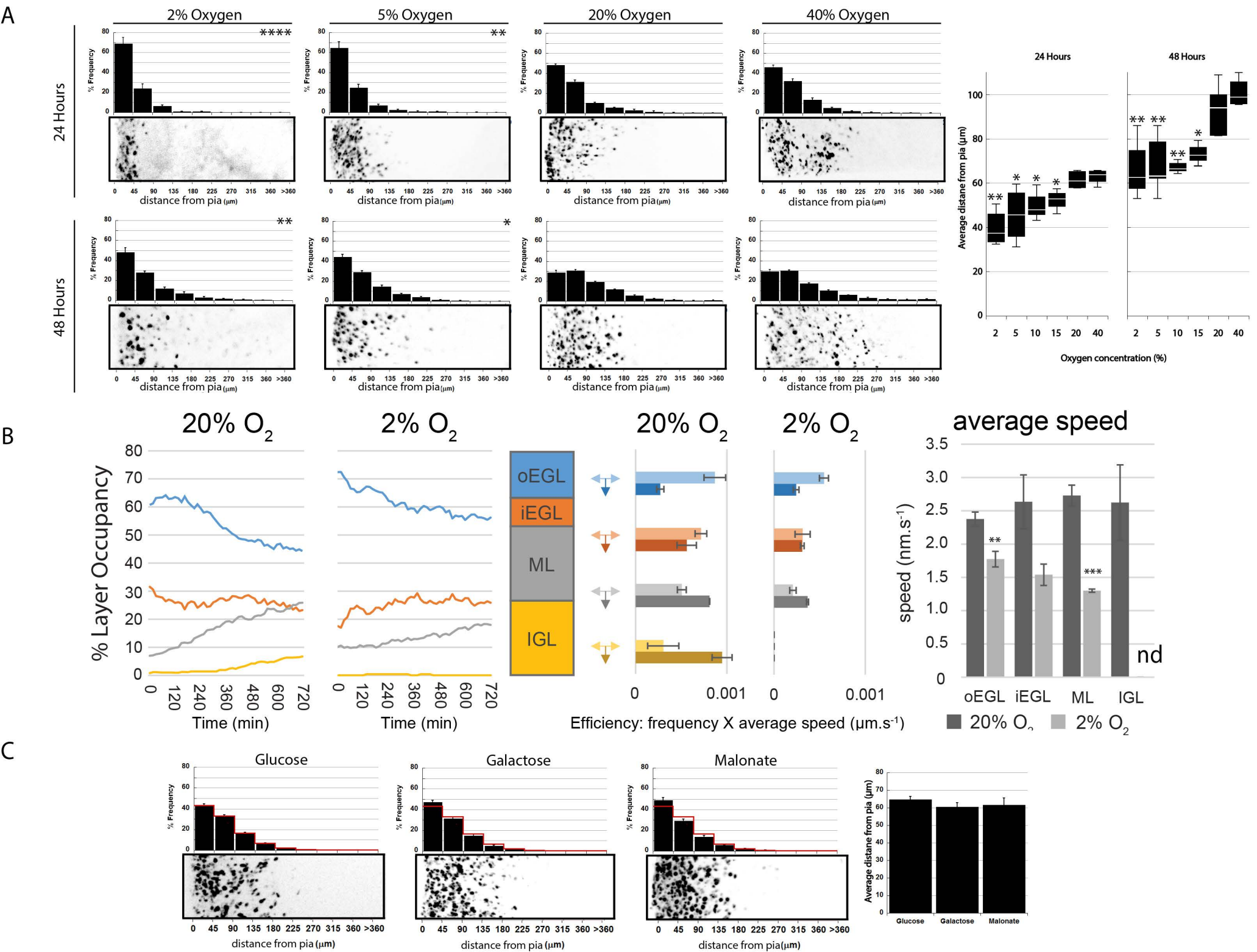


Figure 3

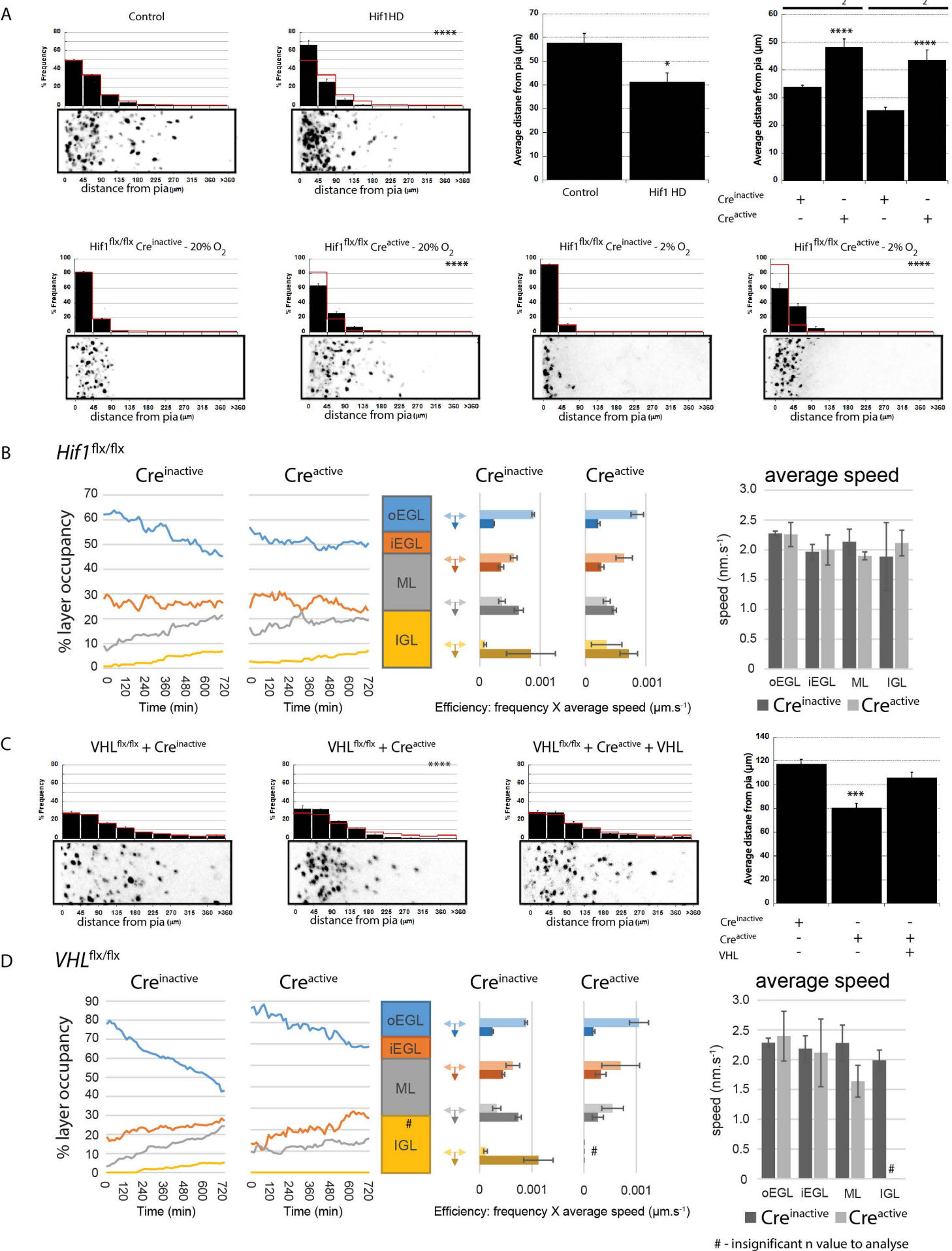
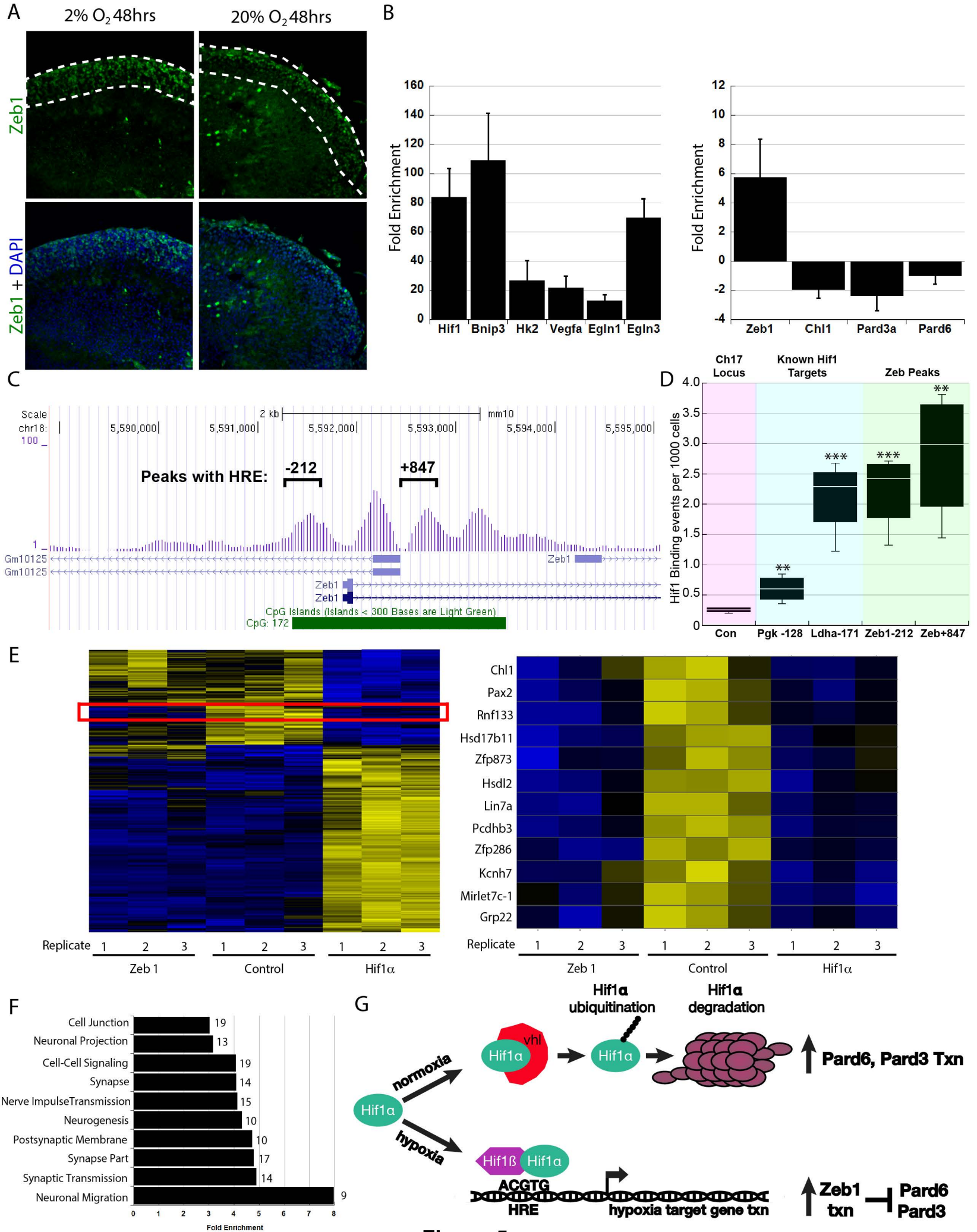
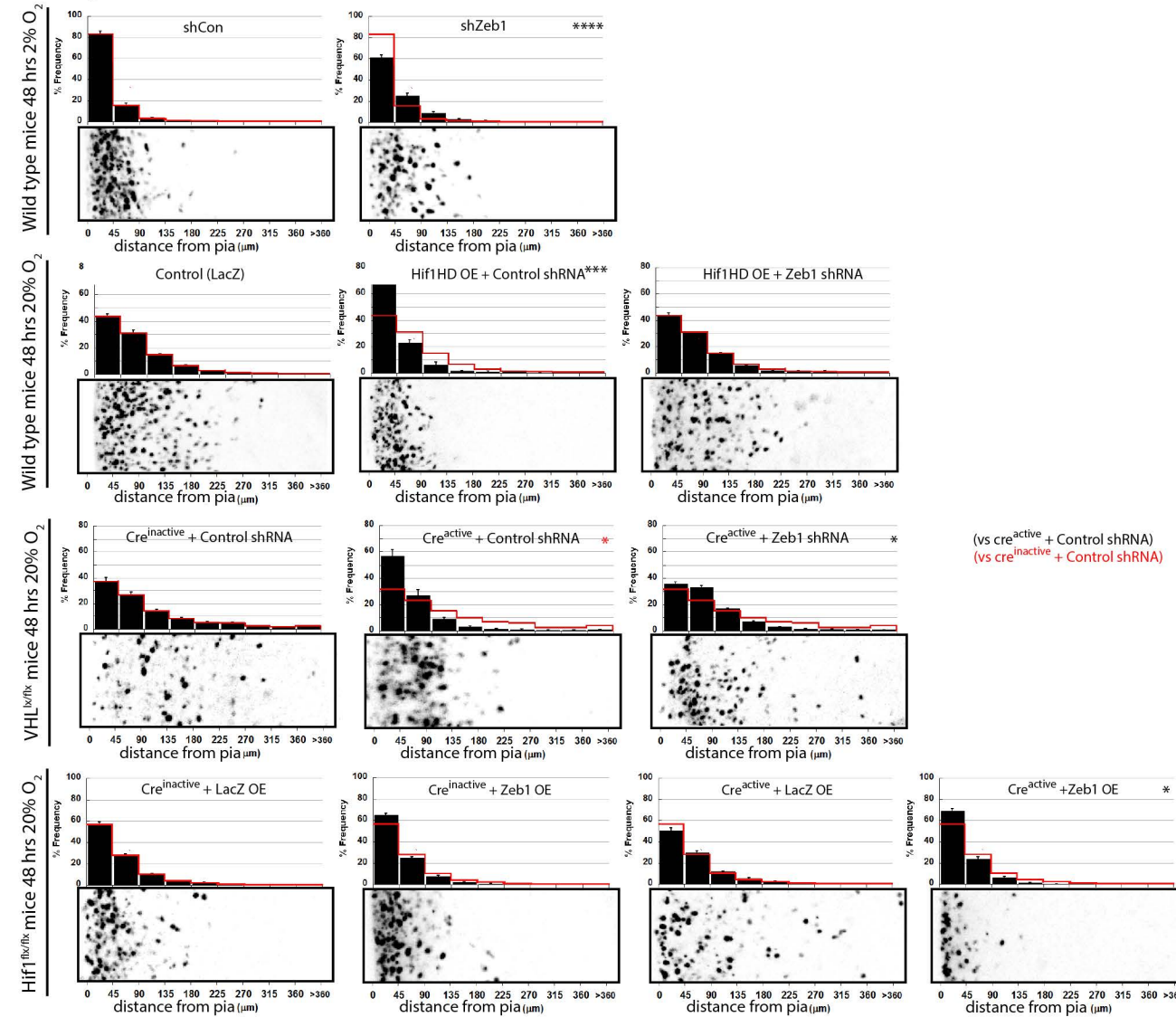


Figure 4



A Zeb1 Epistasis



B Pard Complex Epistasis

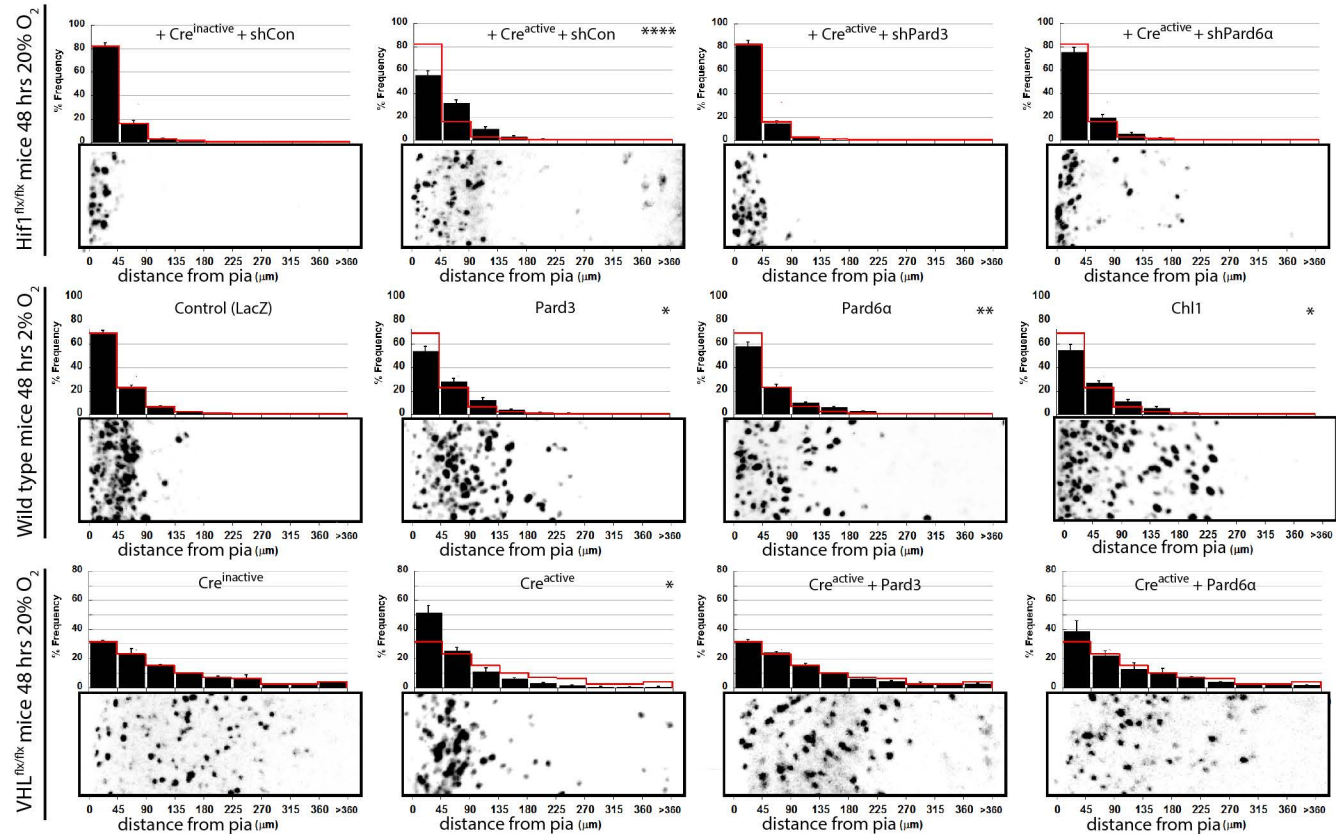


Figure 6

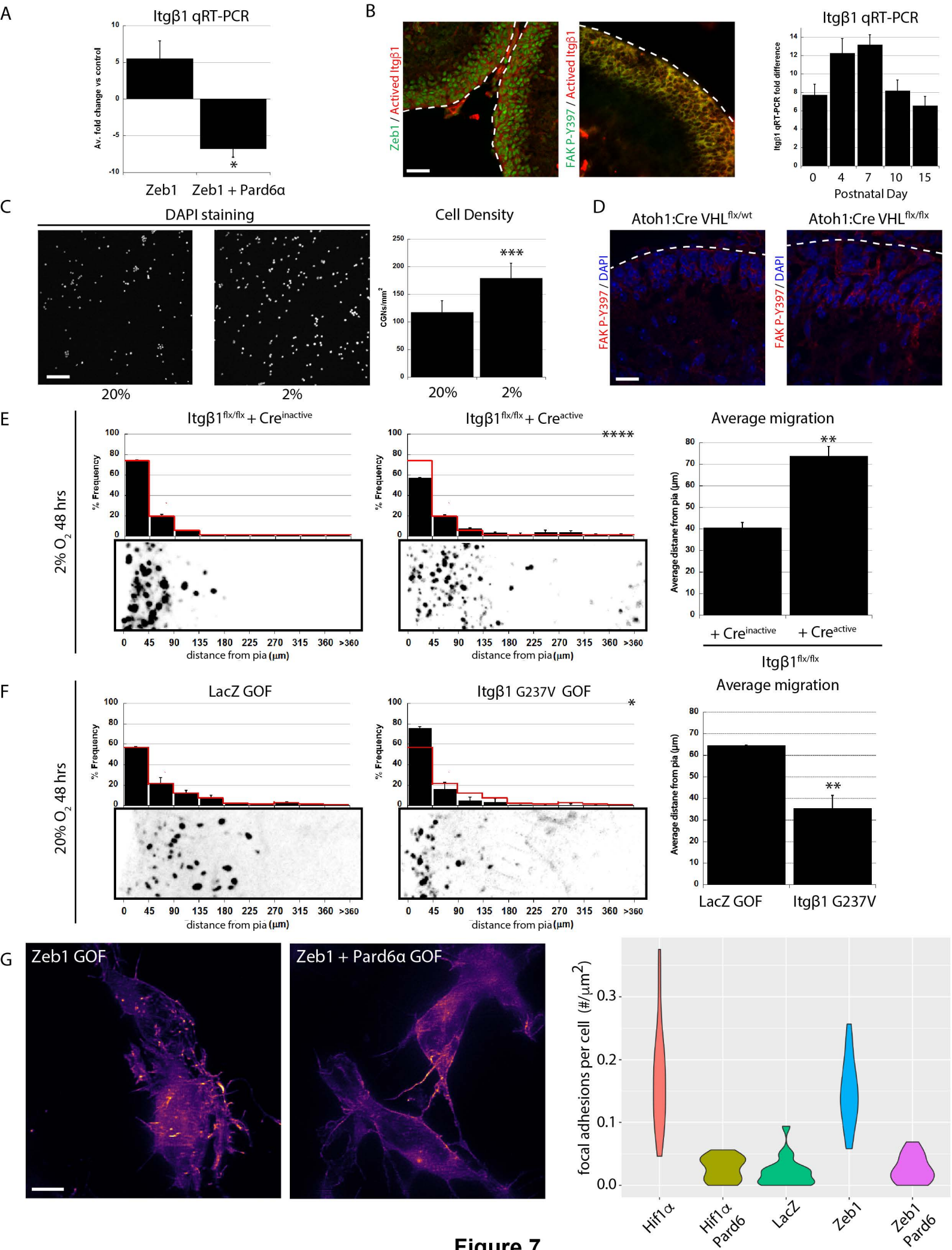
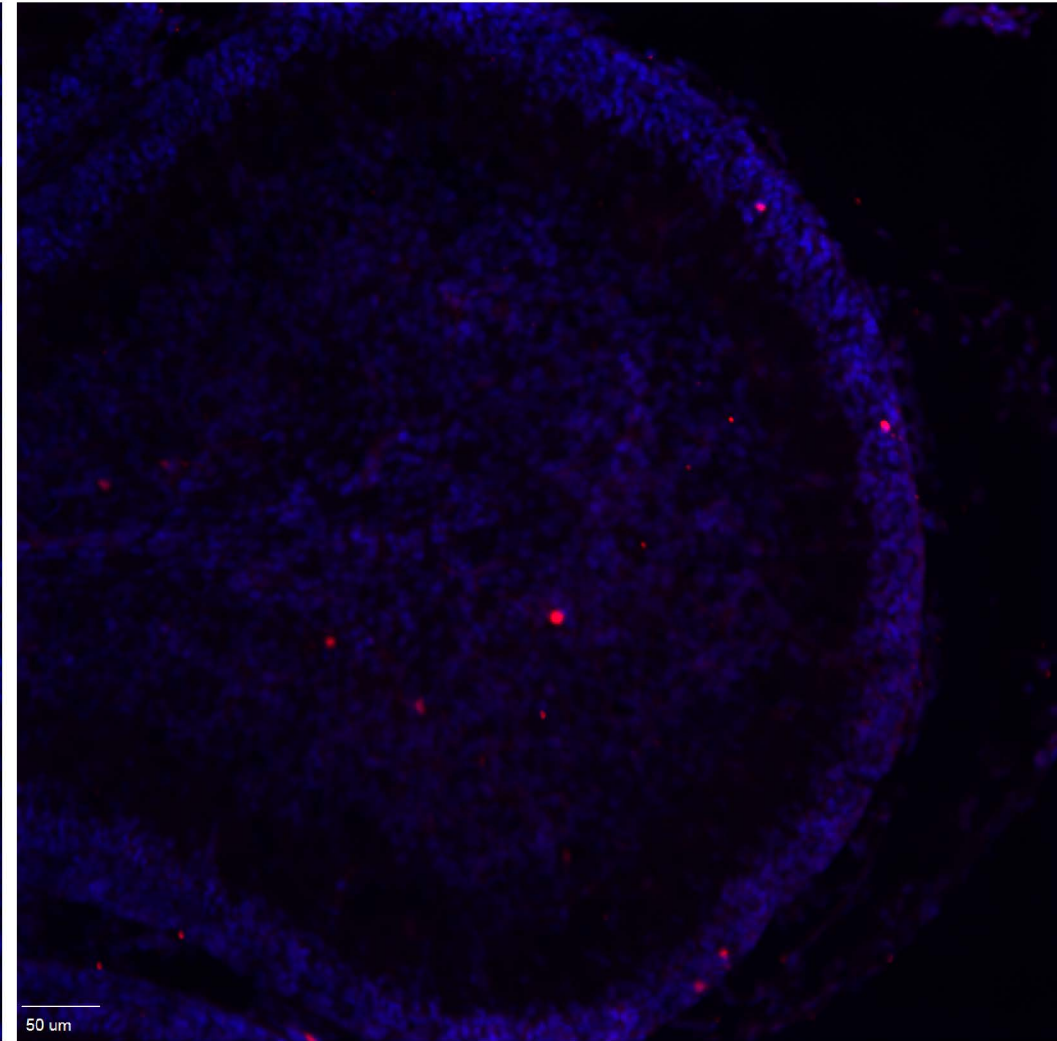
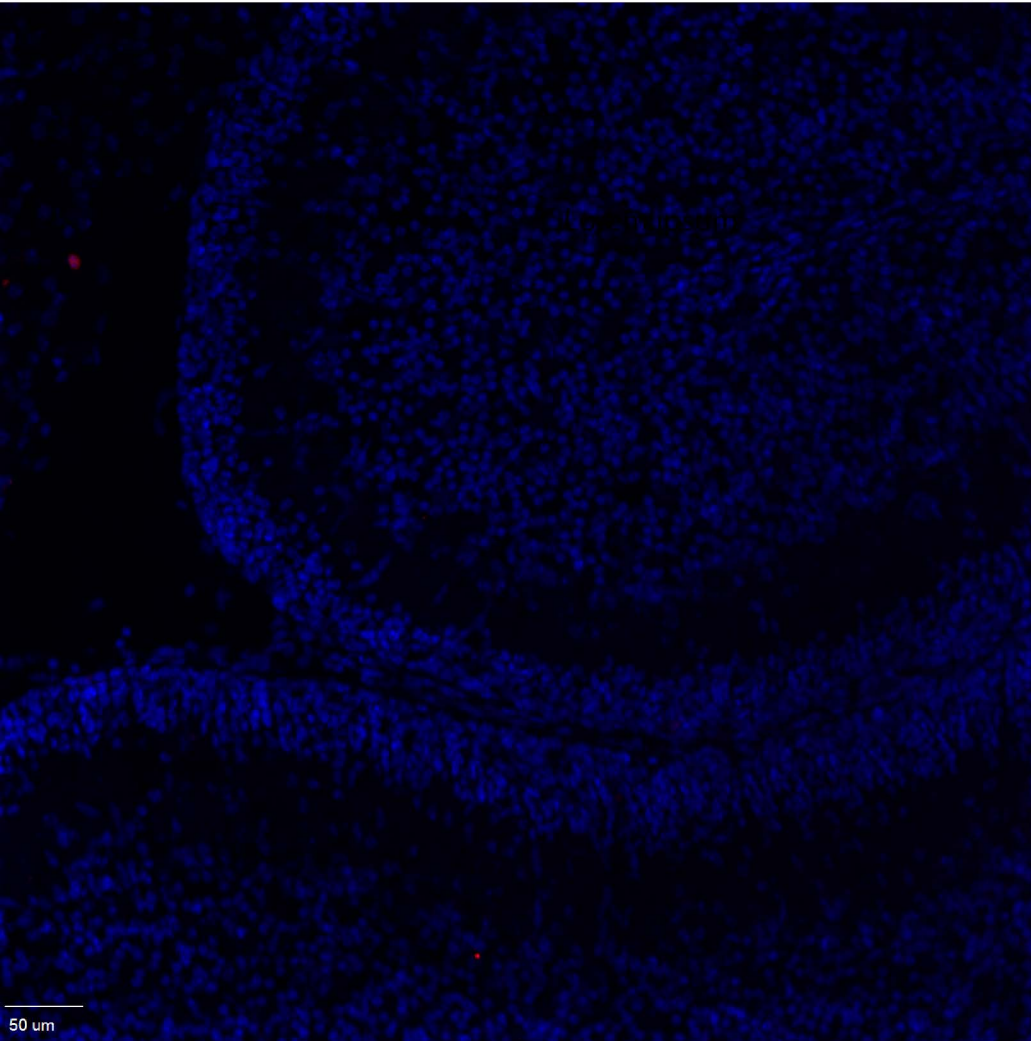


Figure 7

Atoh1-Cre:VHL^{flx/wt}

Atoh1-Cre:VHL^{flx/flx}

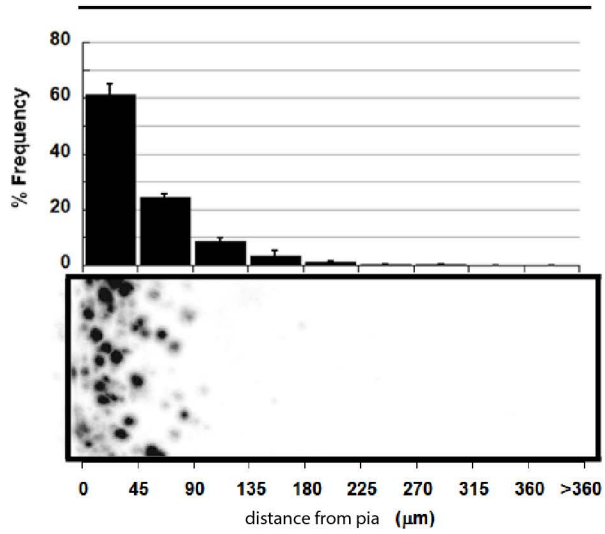


Cleaved Caspase3 Dapi

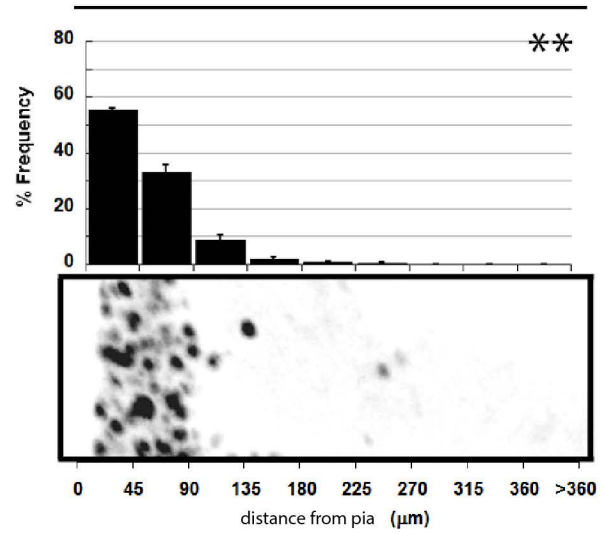
Supplemental Figure 1

24 Hours

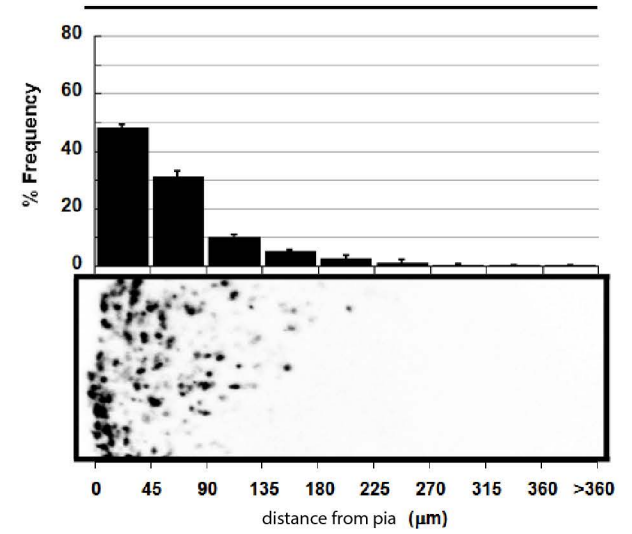
10% Oxygen



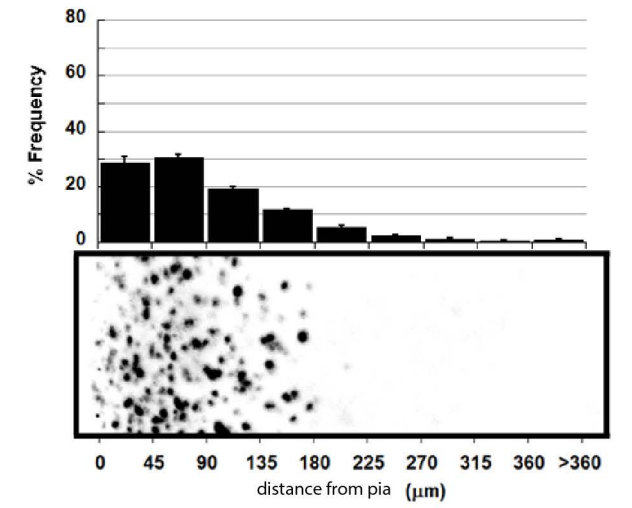
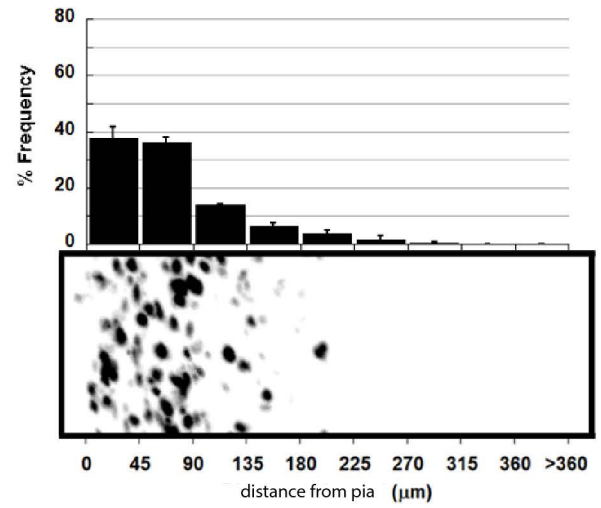
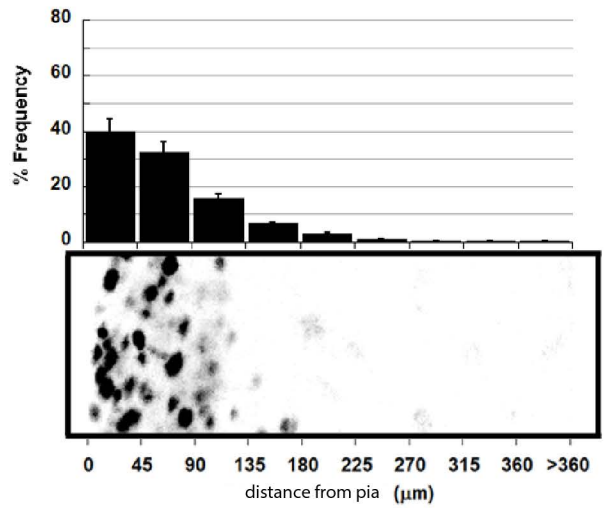
15% Oxygen



20% Oxygen

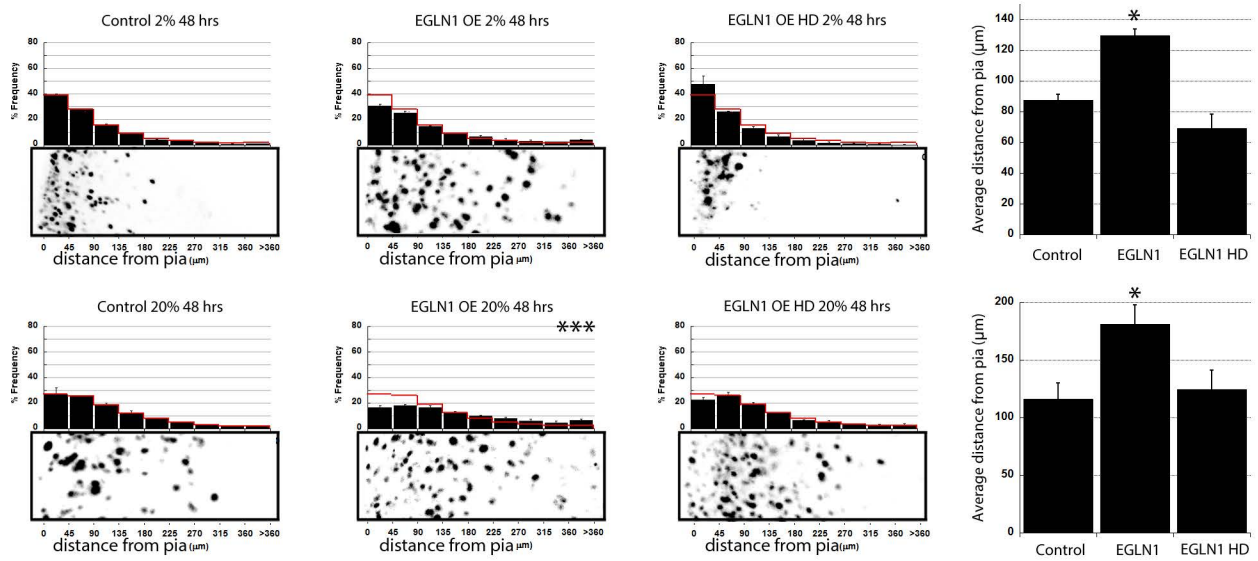


48 Hours

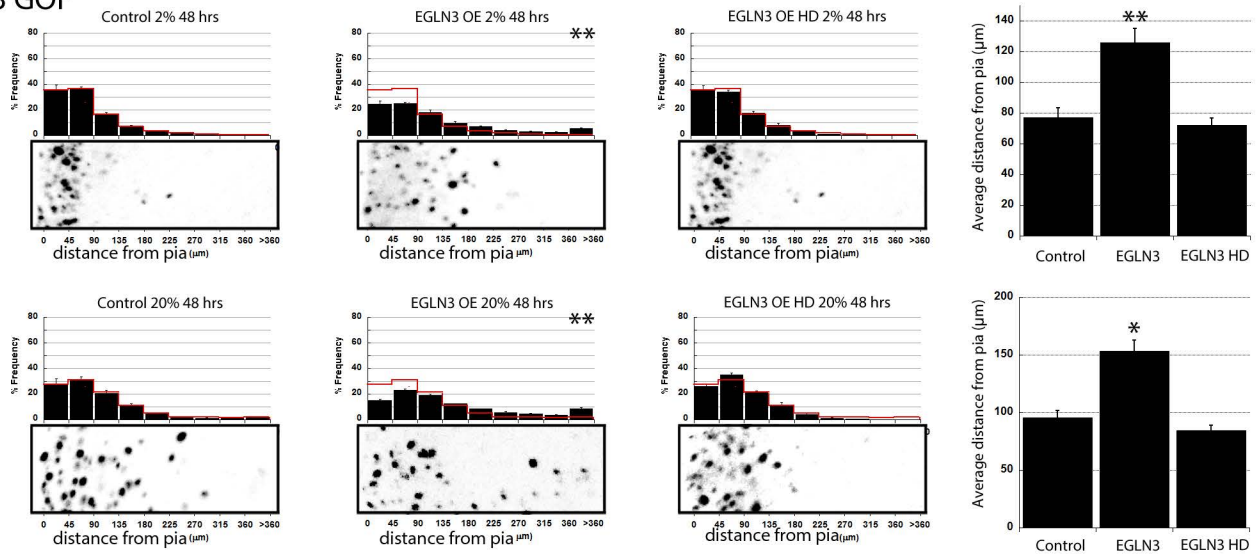


Supplemental Figure 2

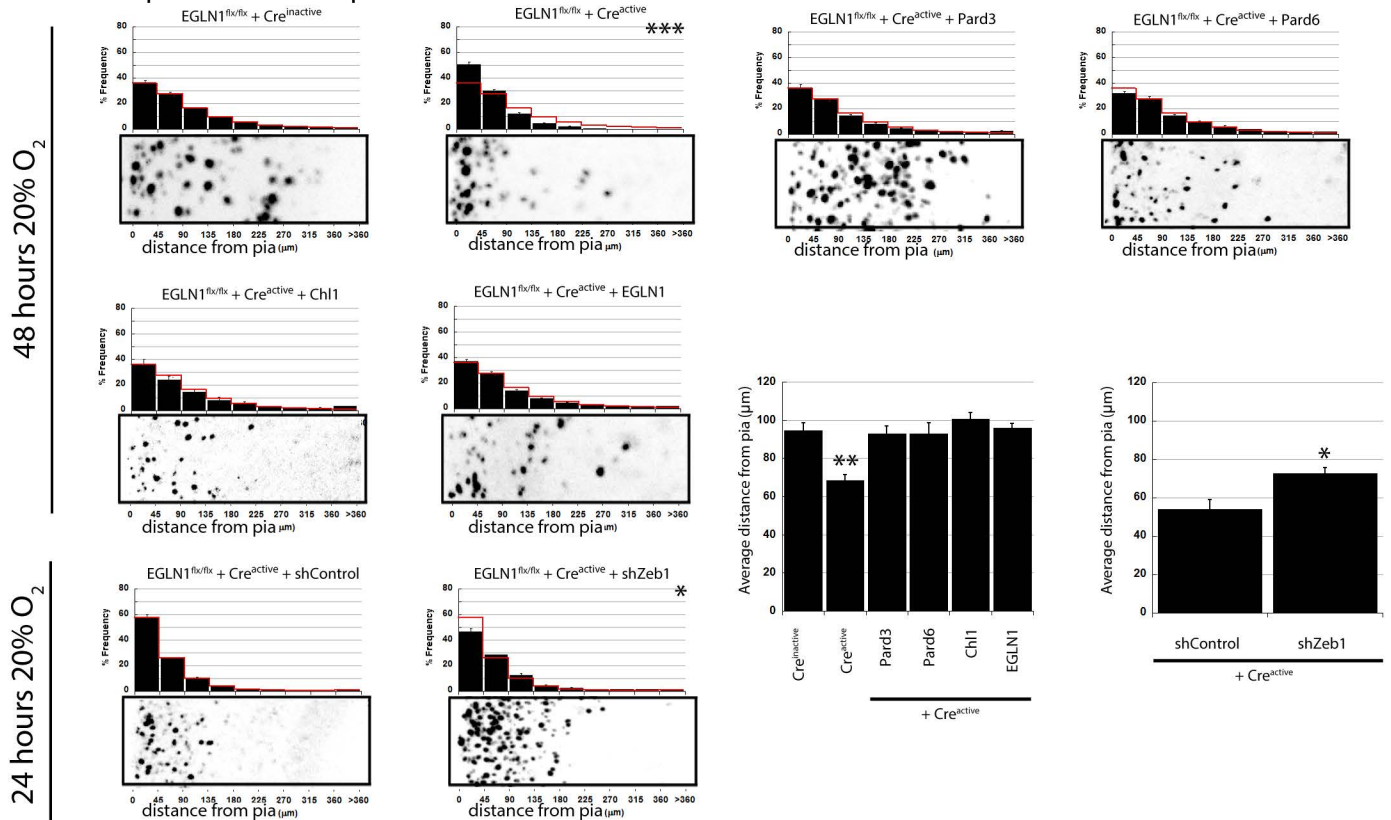
A EGLN1 GOF



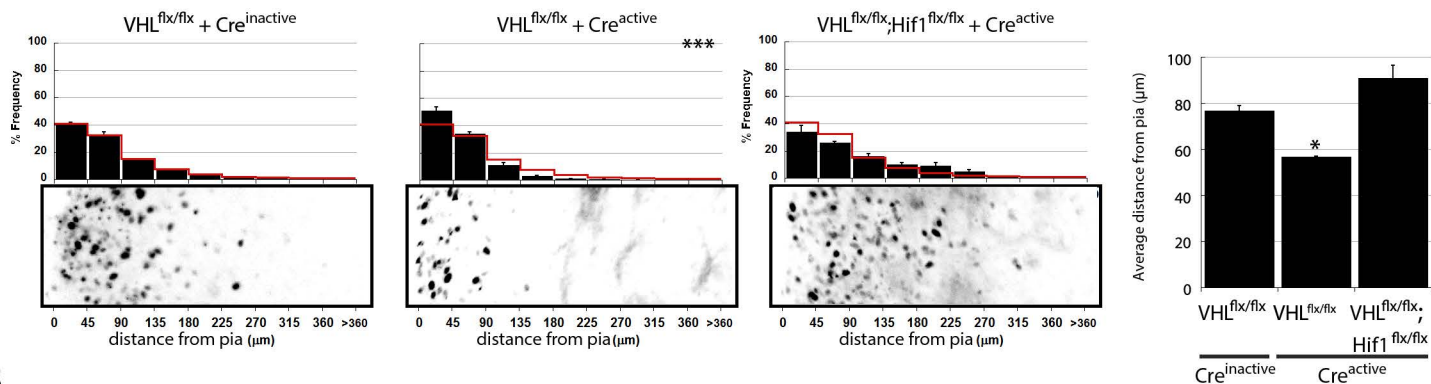
B EGLN3 GOF



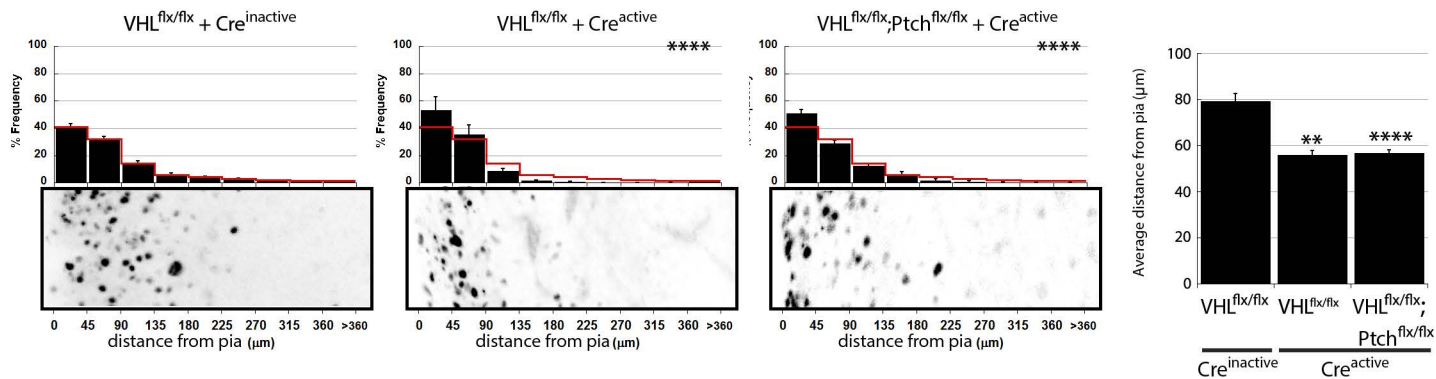
C EGLN1 LOF plus Pard-Zeb1 epistasis



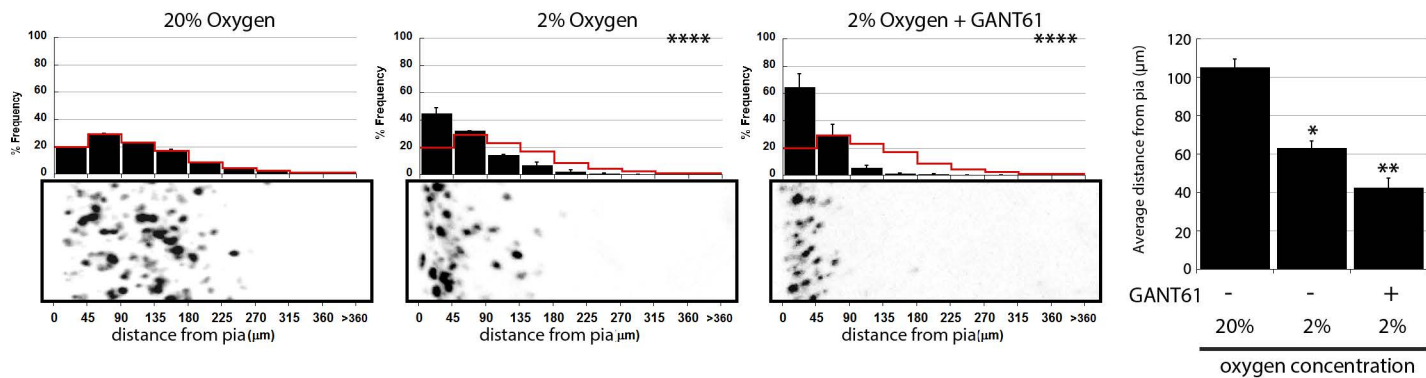
A



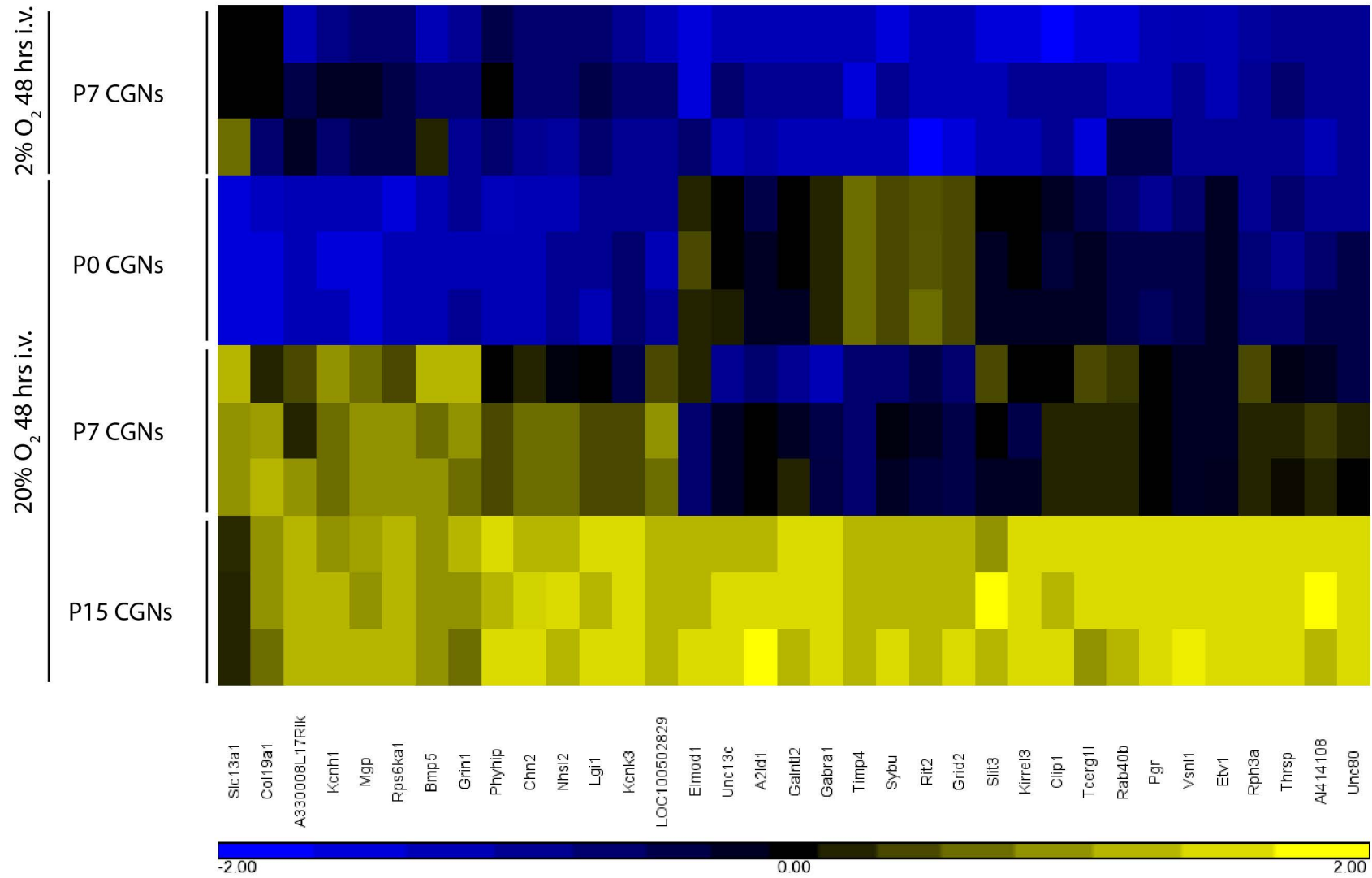
B



C

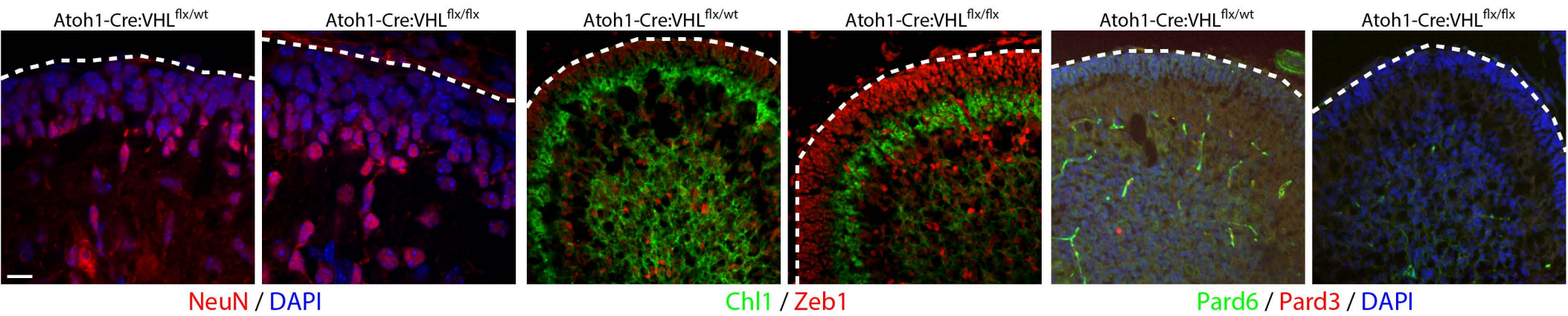


Supplemental Figure 4

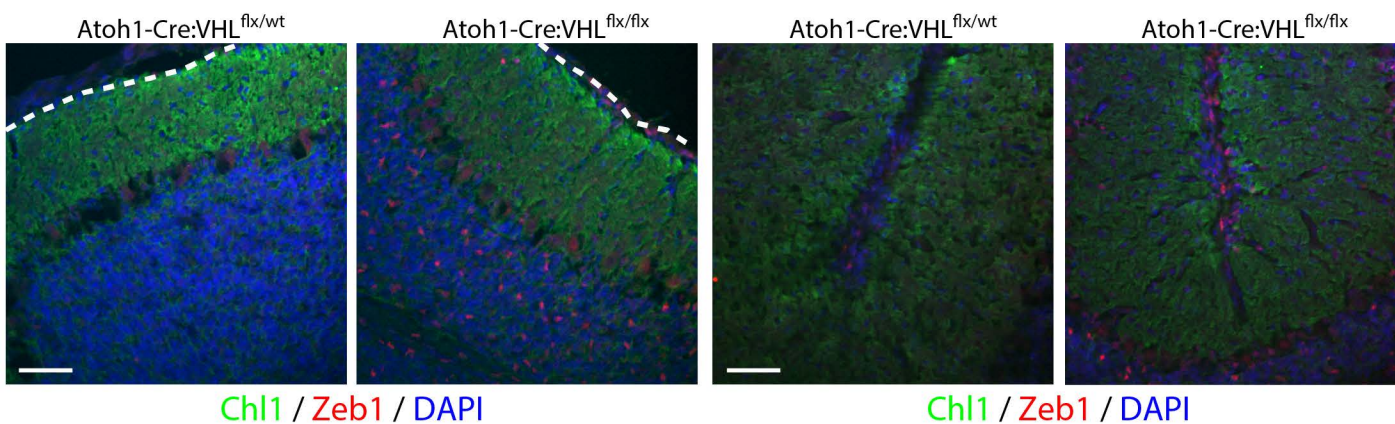


Supplemental Figure 5

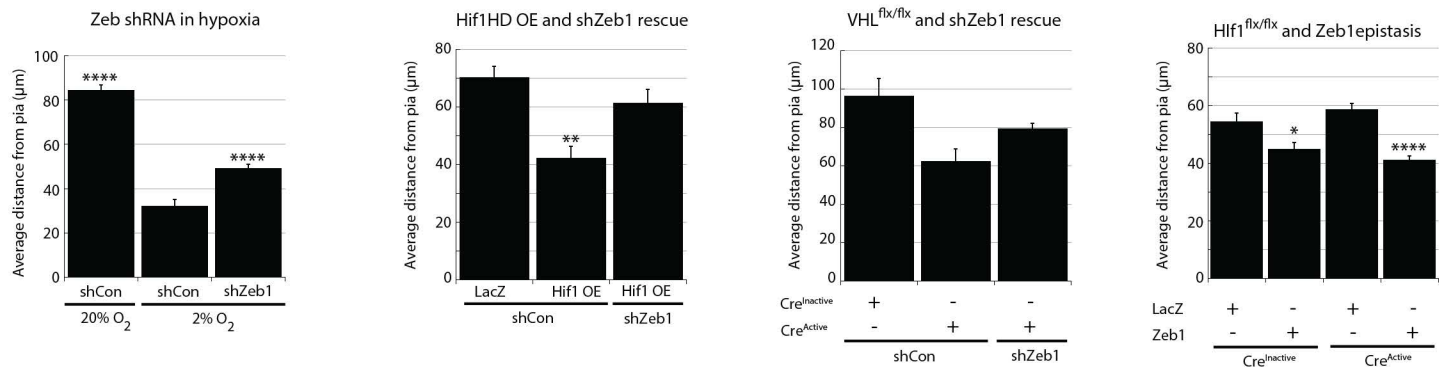
A Staining at P7



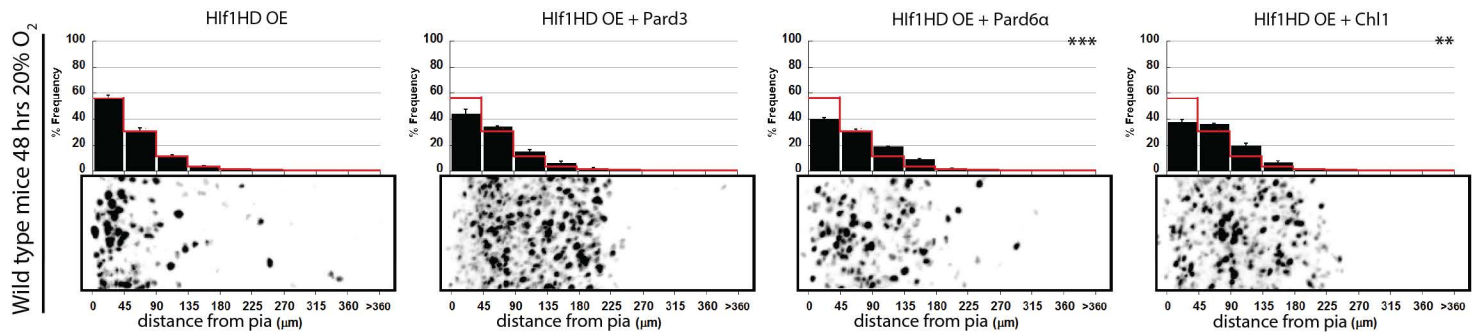
B Staining at P15



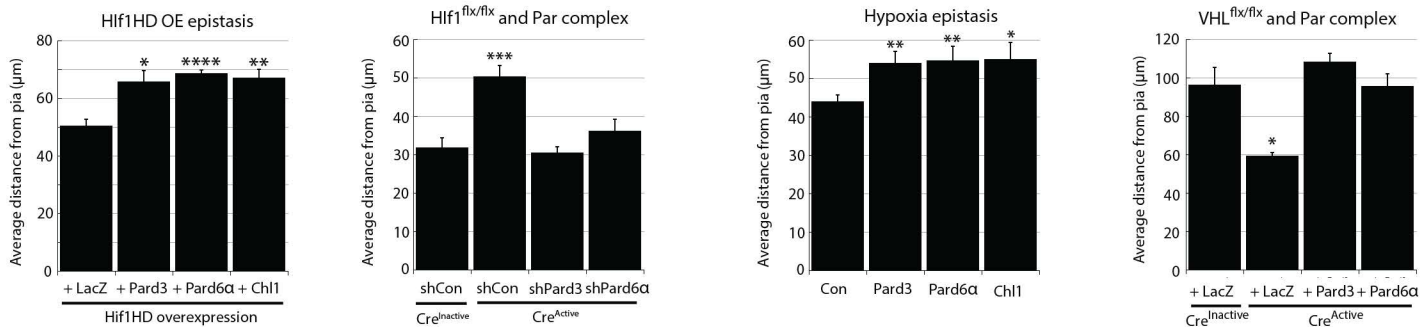
A



B



C



A Pard6 α domains

Interaction partner:

aPKC ζ or λ

? cdc42

Crb, PALS1

Pard3



Disrupting mutant:

K19A

del

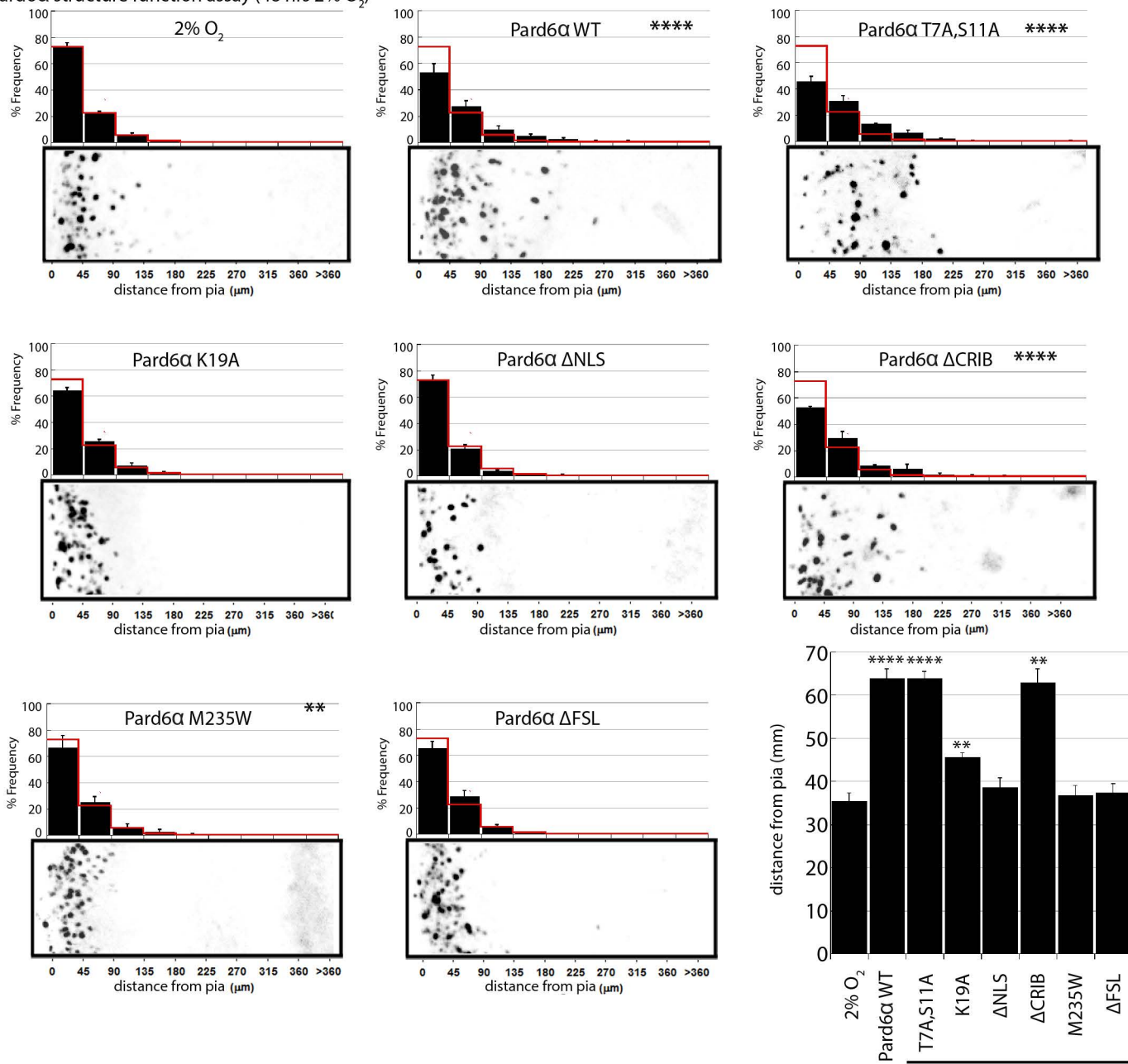
del

M235W

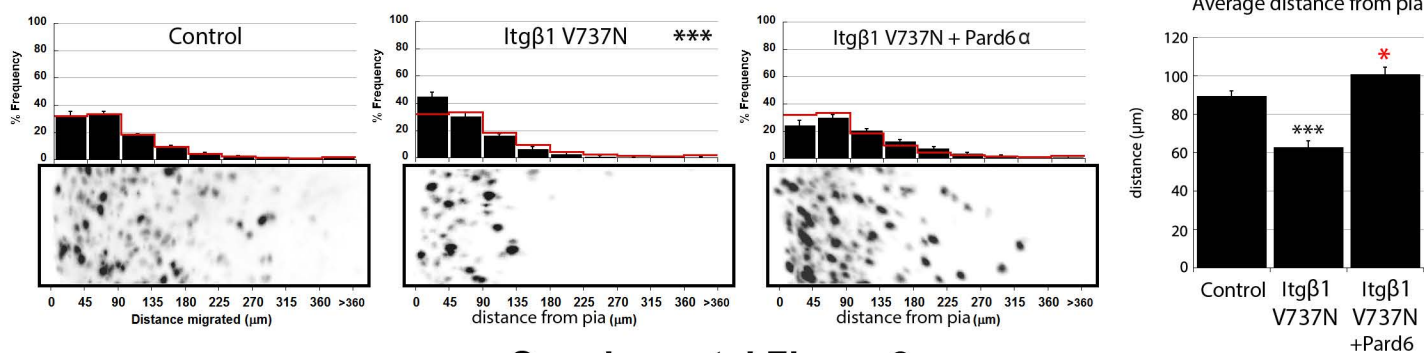
del

S7A,T11A putative phospho-degron alteration used as control mutant

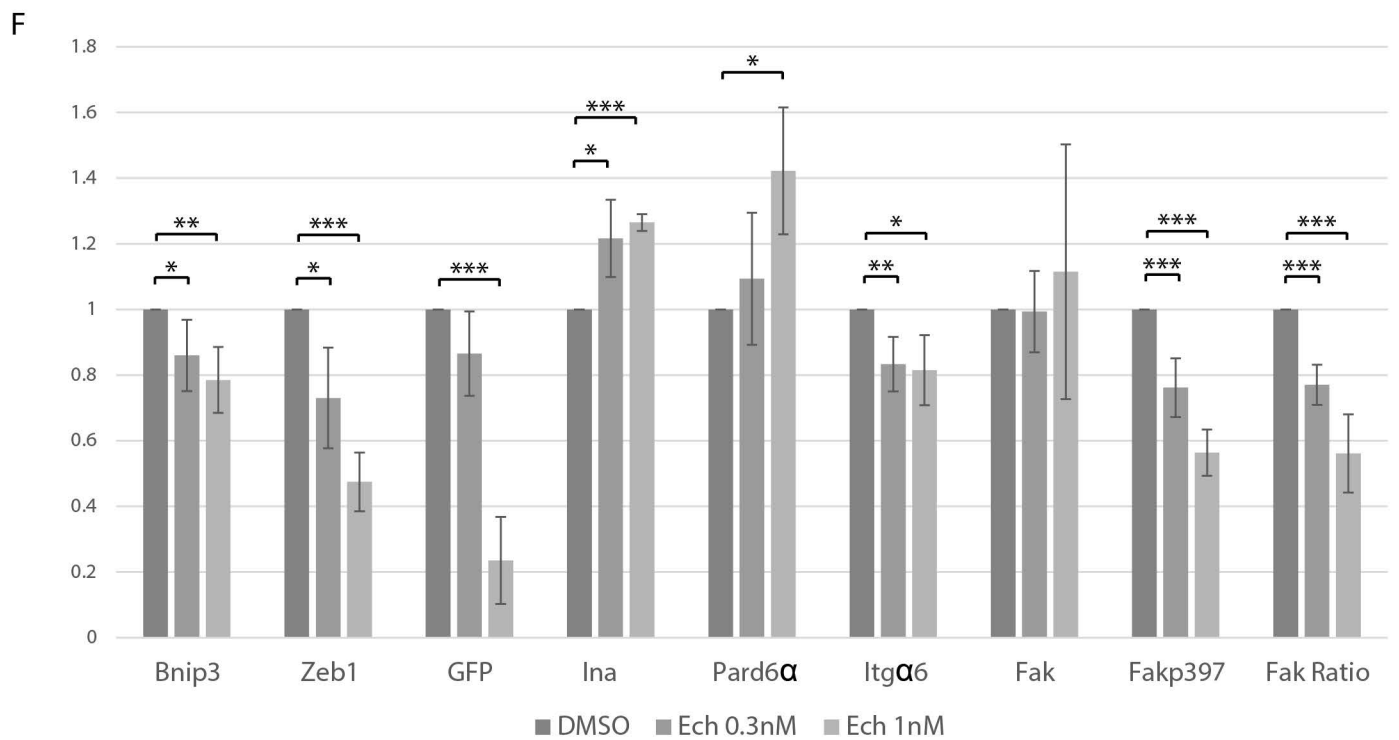
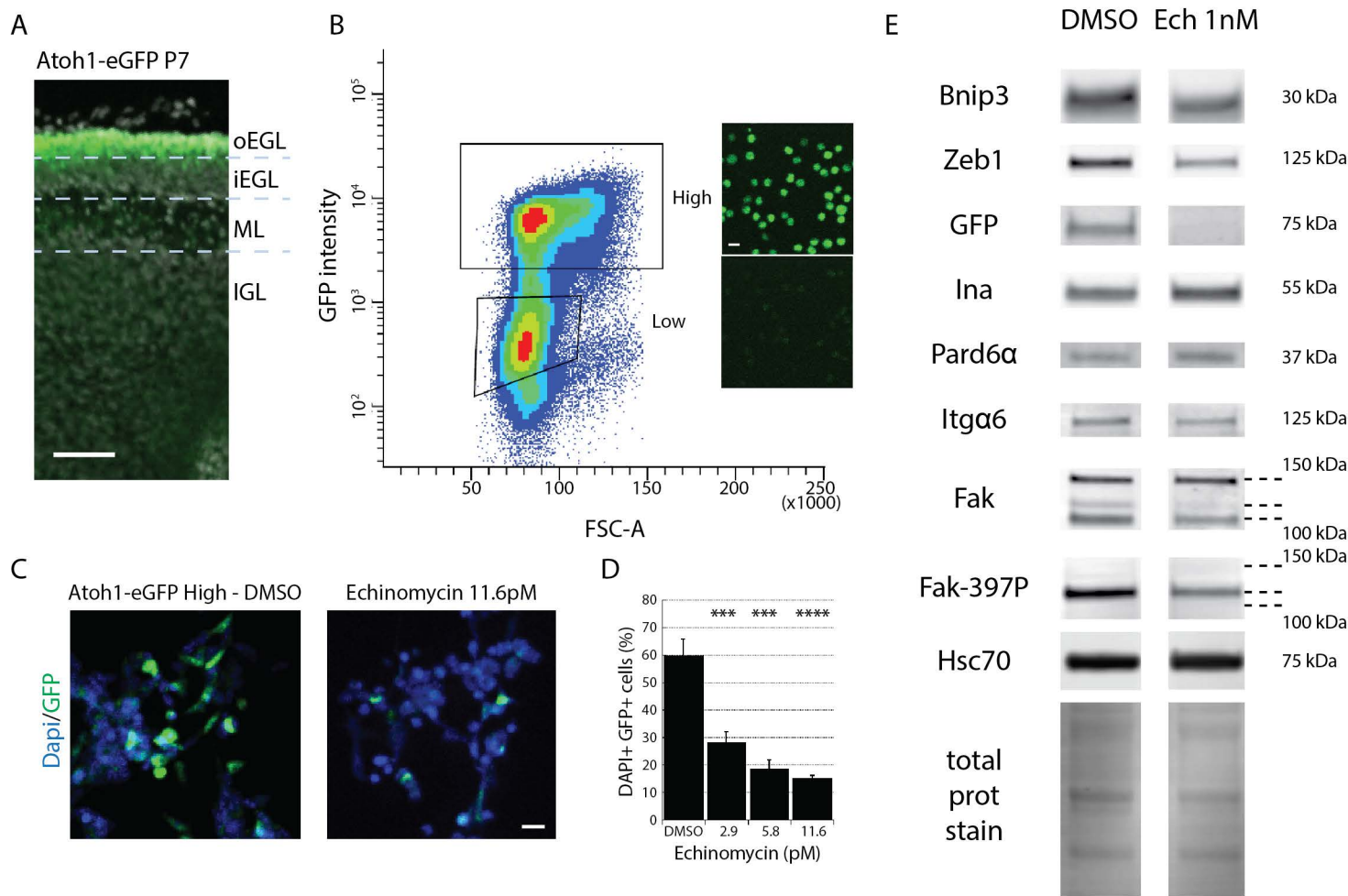
B Pard6 α structure function assay (48 hrs 2% O₂)



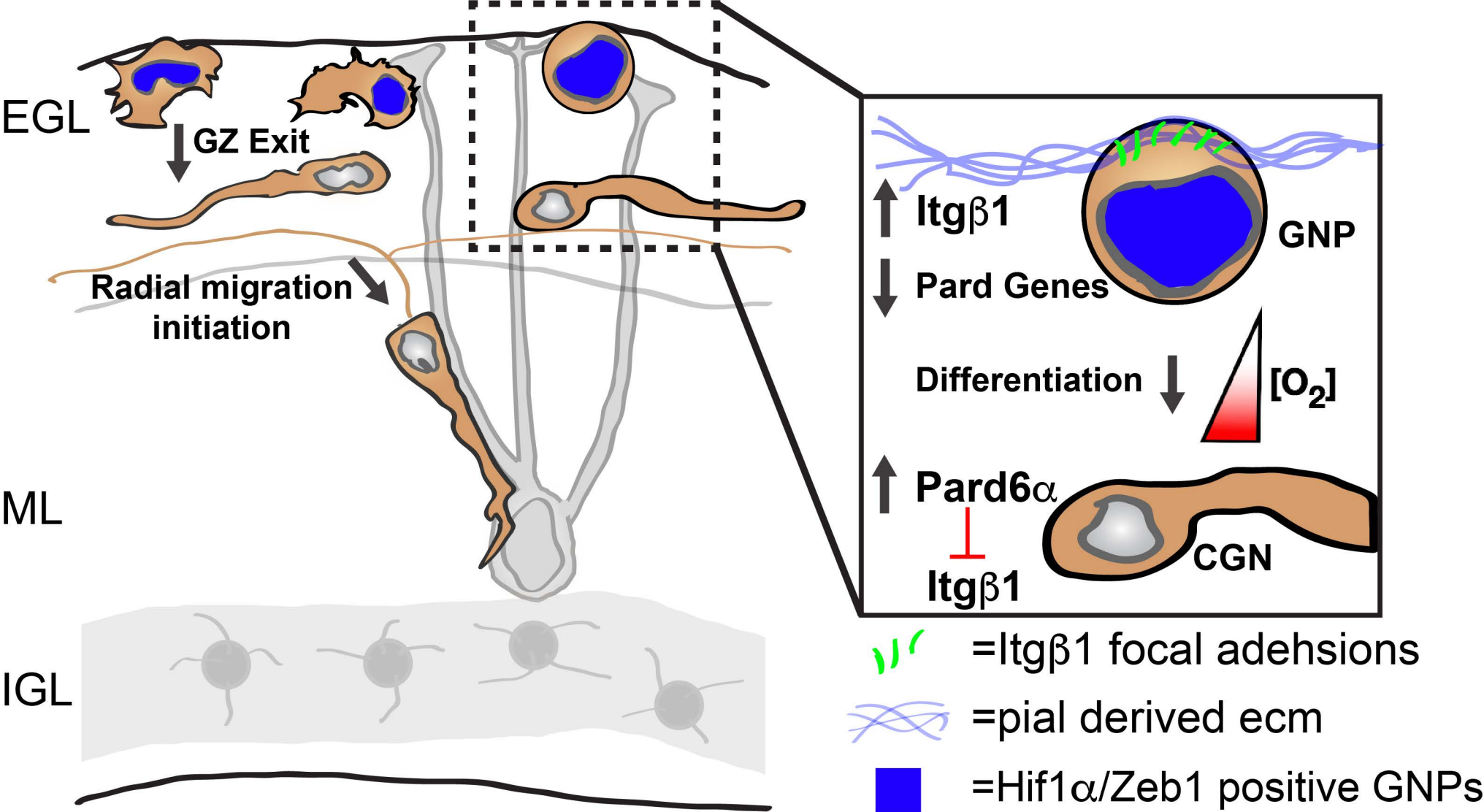
C Pard6 α rescue of intergrin β 1 G237V (48 hrs 20% O₂)



Supplemental Figure 8



Supplemental Figure 9



Supplemental Figure 10

TABLE FOR AUTHOR TO COMPLETE

Please upload the completed table as a separate document. **Please do not add subheadings to the Key Resources Table.** If you wish to make an entry that does not fall into one of the subheadings below, please contact your handling editor. (NOTE: For authors publishing in Current Biology, please note that references within the KRT should be in numbered style, rather than Harvard.)

KEY RESOURCES TABLE

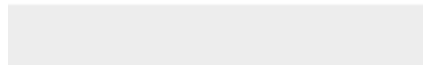
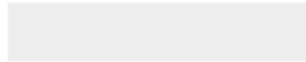
REAGENT or RESOURCE	SOURCE	IDENTIFIER
Antibodies		
Mouse monoclonal anti-Pard6a (clone C-3) (1:100)	Santa Cruz Biotechnology	Cat# sc-365323, RRID:AB_10846183
Rabbit monoclonal anti-Integrin alpha 6 (clone EPR18124) (1:200)	Abcam	Cat# ab181551
Rabbit polyclonal anti-Fak (1:200)	Abcam	Cat# ab131435, RRID:AB_11154758
Rabbit monoclonal anti-Phospho-FAK (Tyr397) (clone 31H5L17) (1:200)	Thermo Fisher Scientific	Cat# 700255, RRID:AB_2532307
Rabbit polyclonal anti-Zeb1 (1:1000)	Sigma-Aldrich	Cat# HPA027524, RRID:AB_1844977
Rabbit monoclonal anti-Bnip3/Nix (clone D4R4B) (1:500)	Cell Signaling Technology	Cat# 12396, RRID:AB_2688036
Rabbit polyclonal anti-alpha internexin (1:1000)	Abcam	Cat# ab7259, RRID:AB_305807
Goat polyclonal anti-GFP (1:500)	Abcam	Cat# ab6673, RRID:AB_305643
Mouse monoclonal anti-activated beta1 integrin HUTS4	Millipore	Catalog #: MAB2079Z
Bacterial and Virus Strains		
Biological Samples		
Chemicals, Peptides, and Recombinant Proteins		
Echinomycin	Tocris	Cat# 5520
Mouse Laminin	EMD Millipore, Chemicon	Cat# CC095
Critical Commercial Assays		
Deposited Data		

Experimental Models: Cell Lines		
Experimental Models: Organisms/Strains		
Mouse: Atoh1-eGFP: B6.129S-Atoh1tm4.1Hzo/J	The Jackson Laboratory	IMSR Cat# JAX:013593, RRID:IMSR_JAX:01 3593
Oligonucleotides		
Recombinant DNA		
Software and Algorithms		
Image Studio 5.2	Li-COR Biotechnology	https://www.licor.com/bio/image-studio/ , RRID:SCR_015795
Other		



[Click here to access/download](#)

Supplemental Videos and Spreadsheets
Supplemental Movie 1.mov

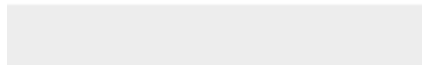


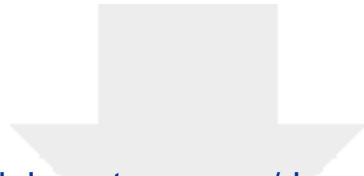


[Click here to access/download](#)

Supplemental Videos and Spreadsheets

Supplemental Movie 2 20% O2.mov





[Click here to access/download](#)

Supplemental Videos and Spreadsheets

Supplemental Movie 3 2% O2.mov

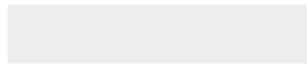


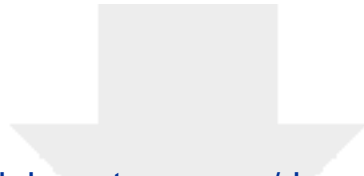


[Click here to access/download](#)

Supplemental Videos and Spreadsheets

Supplemental Movie 4 Hif1 fl_fl Cre Inactive.mov

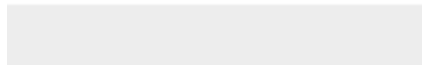




[Click here to access/download](#)

Supplemental Videos and Spreadsheets

Supplemental Movie 5 Hif1 fl_fl Cre Active.mov

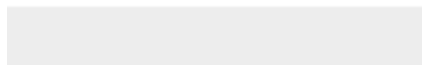




[Click here to access/download](#)

Supplemental Videos and Spreadsheets

Supplemental Movie 6 VHL fl_fl Cre Inactive.mov





[Click here to access/download](#)

Supplemental Videos and Spreadsheets

Supplemental Movie 7 VHL fl_fl Cre Active.mov

